Dissertations, Master's Theses and Master's Reports - Open

Dissertations, Master's Theses and Master's Reports

2005

RF-sputter fabrication of magnetic garnet thin films and simulation modeling for 1-D magnetic photonic crystal waveguide devices

Haichun Yang
Michigan Technological University

RF-Sputter Fabrication of Magnetic Garnet Thin Films

and Simulation Modeling For

1-D Magnetic Photonic Crystal Waveguide Devices

By

Haichun Yang

A DISSERTATION

Submitted in partial fulfillment of the requirement
For the degree of

DOCTOR OF PHILOSOPHY

Material Science and Engineering

MICHIGAN TECHNOLOGICAL UNIVERSITY
November 10, 2005

This dissertation, "**RF-Sputter Fabrication of Magnetic Garnet Thin Films and Simulation Modeling For 1-D Magnetic Photonic Crystal Waveguide Devices**" is hereby approved in partial fulfillment of the requirements for the degree of DOCTOR OF PHILOSOPHY in the field of Material Science and Engineering.

DEPARTMENT or PROGRAM:

Material Science and Engineering

Signatures:

Dissertation Advisor

Typewritten Name Dr. Miguel Levy

Committee members

Typewritten Name Dr.   Yoke Khin Yap

Typewritten Name Dr. Stephen A. Hackney

Typewritten Name Dr. Paul L. Bergstrom

Department Chair

Typewritten Name Dr. Mark R. Plichta

Date   November 10, 2005

RF-sputter Fabrication of Magnetic Garnet Thin Films and

Simulation Modeling for

1-D Magnetic Photonic Crystal Waveguide Devices

By Haichun Yang
Submitted to the department of Material science on Nov. 10, 2005
In partial fulfillment of requirements for the degree of
Doctor of Philosophy

Abstract

One dimensional magnetic photonic crystals (1D-MPC) are promising structures for integrated optical isolator applications. Rare earth substituted garnet thin films with proper Faraday rotation are required to fabricate planar 1D-MPCs. In this thesis, flat-top response 1D-MPC was proposed and spectral responses and Faraday rotation were modeled. Bismuth substituted iron garnet films were fabricated by RF magnetron sputtering and structures, compositions, birefringence and magnetooptical properties were studied. Double layer structures for single mode propagation were also fabricated by sputtering for the first time.

Multilayer stacks with multiple defects (phase shift) composed of Ce-YIG and GGG quarter-wave plates were simulated by the transfer matrix method. The transmission and Faraday rotation characteristics were theoretically studied. It is found that flat-top response, with 100% transmission and near 45° rotation is achievable by adjusting the inter-defect spacing, for film structures as thin as 30 to 35 μm. This is better than 3-fold reduction in length compared to the best Ce-YIG films for comparable rotations, thus allows a considerable reduction in size in manufactured optical isolators. Transmission bands as wide as 7nm were predicted, which is considerable improvement over 2 defects structure. Effect of repetition number and ratio factor on transmission and Faraday rotation ripple factors for the case of 3 and 4 defects structure has been discussed. Diffraction across the structure corresponds to a longer optical path length. Thus the use of guided optics is required to minimize the insertion losses in integrated devices. This part is discussed in chapter 2 in this thesis.

Bismuth substituted iron garnet thin films were prepared by RF magnetron sputtering. We investigated or measured the deposition parameters optimization, crystallinity, surface morphologies, composition, magnetic and magnetooptical properties. A very high crystalline quality garnet film with smooth surface has been heteroepitaxially grown on (111) GGG substrate for films less than 1μm. Dual layer structures with two distinct XRD peaks (within a single sputtered film) start to develop when films exceed this

thickness. The development of dual layer structure was explained by compositional gradient across film thickness, rather than strain gradient proposed by other authors. Lower DC self bias or higher substrate temperature is found to help to delay the appearance of the 2nd layer. The deposited films show in-plane magnetization, which is advantageous for waveguide devices application. Propagation losses of fabricated waveguides can be decreased by annealing in an oxygen atmosphere from 25dB/cm to 10dB/cm. The Faraday rotation at $\lambda=1.55\mu m$ were also measured for the waveguides. FR is small (10° for a 3mm long waveguide), due to the presence of linear birefringence. This part is covered in chapter 4.

We also investigated the elimination of linear birefringence by thickness tuning method for our sputtered films. We examined the compressively and tensilely strained films and analyze the photoelastic response of the sputter deposited garnet films. It has been found that the net birefringence can be eliminated under planar compressive strain conditions by sputtering. Bi-layer GGG on garnet thin film yields a reduced birefringence. Temperature control during the sputter deposition of GGG cover layer is critical and strongly influences the magnetization and birefringence level in the waveguide. High temperature deposition lowers the magnetization and increases the linear birefringence in the garnet films. Double layer single mode structures fabricated by sputtering were also studied. The double layer, which shows an in-plane magnetization, has an increased RMS roughness upon upper layer deposition. The single mode characteristic was confirmed by prism coupler measurement. This part is discussed in chapter 5.

Acknowledgements

First of all, I would like to express my gratitude to my advisor Prof. Miguel Levy. Thank you for giving me the precious opportunity to work with you and for guiding me, inspiring me and caring me throughout these years. You will always be a great advisor, teacher, researcher and human being.

It is a great pleasure to work together with Raghav Rao Vanga, Philip Huang, Rong Li and Ziyou Zhou in Prof. Levy's integrated photonics group. Thanks for their stimulant vision and personality and of course their friendship. Also I should mention Dr. Young-Hwan Kim for teaching me to operate the sputtering system during my initial steps and for sharing me with his insight and vision in garnet thin films.

I am grateful to faculty, staff and fellow graduate students in department of material science. Ed Laitila and Owen Mills are especially thanked for their help on characterization equipments. I would also like to thank Prof. Peter Moran for his kindness to let me use the high resolution X-ray diffractometer and helpful discussions and suggestions.

At last but not the least, I am forever indebted to my parent and my wife Rong Li for their understanding, encouragement and endless patience when it was most required. I would also like to thank my son Doudou for the joy and pleasure he brought me.

Abbreviations:

AFM   Atomic Force Microscopy
BIG   Bismuth Iron Garnet ($Bi_3Fe_5O_{12}$)
Bi-YbIG   Bismuth substituted Ytterbium Iron Garnet
Bi-YIG   Bismuth substituted Yttrium Iron Garnet
Ce-YIG   Cerium substituted Yttrium Iron Garnet
CMT   Coupled Mode Theory
EPMA   Electron Probe Microanalysis
FR   Faraday Rotation
GGG   Gadolinium Gallium Garnet ($Gd_3Ga_5O_{12}$)
HRXRD   High resolution X-Ray Diffraction
LCP   Left Circularly Polarized light
LPE   Liquid Phase Epitaxy
MO   Magnetooptical
MOCVD   Metalorganic Chemical Vapor Deposition
MPC   Magnetic Photonic Crystal
PLD   Pulsed Laser Deposition
RBS   Rutherford Backscattering Spectrometry
RCP   Right Circularly Polarized light
RF   Radio Frequency
SAE   Selective Area Epitaxy
TMM   Transfer Matrix Method
VSM   Vibrating Sample Magnetrometer
XPS   X-ray Photon Spectrometry
XRD   X-Ray Diffraction
YIG   Yttrium Iron Garnet ($Y_3Fe_5O_{12}$)

Contents

Chapter 1

Background Introduction and Motivation of this Research

1.1 Overview

In the last few decades, optical fiber communication has grown very rapidly due to its high capacity and high speed for data transport. Semiconductor laser sources are the most important parts in modern optical communications. As a result, it is essential to protect the lasers from the back scattered light. Otherwise, the laser sources are unstable and the life time of lasers is deteriorated. For this purpose, optical isolators are needed.

An optical isolator is a device that allows the laser beam to propagate only in one direction and blocks the back-scattered beam. Fig.1.1 shows the operation principle of an isolator. A beam passes through a polarizer and becomes vertically polarized. The polarization plane rotates 45° after passing through the Faraday rotator. The analyzer is oriented with its polarization axis at 45° from the input polarization so that there is no
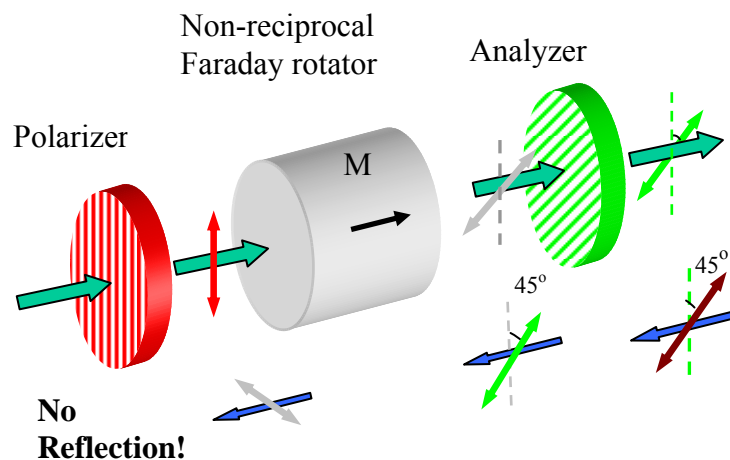
Figure 1.1 *Operation principle of an isolator*

obstruction for the incident light. Any back-scattered light becomes 45° polarized by the analyzer. The polarization plane turns another 45° in the same direction after passing through the Faraday rotator (nonreciprocal effect) and becomes perpendicular to the polarizer. Hence the beam is totally blocked.

The key component in an isolator is the Faraday rotator, which relies on the Faraday rotation effect (Fig.1.2). Faraday rotation is defined as half of the phase difference between right circularly polarized (RCP) and left circularly polarized (LCP) light. A linearly polarized light beam is split into RCP and LCP. RCP and LCP have different indices n_+ and n_- in a magnetooptical (MO) material and consequently propagate with different velocities $\dfrac{c}{n_+}$ and $\dfrac{c}{n_-}$. Therefore, the polarization of linearly polarized light rotates an angle of θ_F after length d by:

$$\theta_F = \frac{\pi d}{\lambda}(n_+ - n_-) \tag{1-1}$$
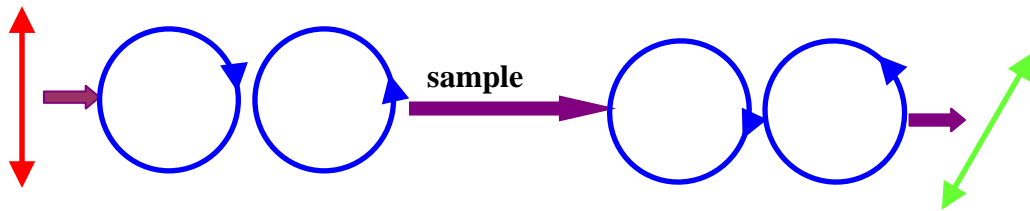
Figure 1.2 *Illustration of Faraday rotation*

Faraday rotation is a nonreciprocal effect. When light is reflected and passes through the sample in the opposite direction, the FR rotates in the same direction as in the forward propagation instead of rotating back. Magnetooptical materials are the basic elements for non-reciprocal isolators. Of all the MO materials, magnetic garnet crystals are the only materials suitable for realization of nonreciprocal devices at near infrared wavelength

(optical communication wavelength at 1.55μm) since they have the largest figure of merit (ratio between Faraday rotation and optical absorption coefficient). $Y_3F_5O_{12}$ (YIG), a garnet material, has been an important focus of research since it was first discovered in 1957 at Bell Labs due to its transparency and a measurable Faraday rotation in the near infrared region. Hundreds of papers have been published on theoretical studies [1-11], thin film preparation [12-50] and nonreciprocal device fabrication [51-62]. Enhancement of Faraday rotation to reduce size and cost of MO devices has also been of great interest among researchers [63-76]. Rare earth elements, such as bismuth [1-3,6-11,14-21,23] and cerium [28-34] had been found to enhance the FR (Fig. 1.3a), without significantly increase in absorption. Other elements, such as Pb and Co can also greatly enhance the FR. However, Pb and Co are 2+ charged and Fe^{4+} should be created to compensate the charge difference. The charge transfer between Fe^{2+} to Fe^{3+} or Fe^{3+} to Fe^{4+} leads to strong optical absorption increase – the coefficient of absorption can be easily increased by a factor of 100 [77].

(a)   (b)
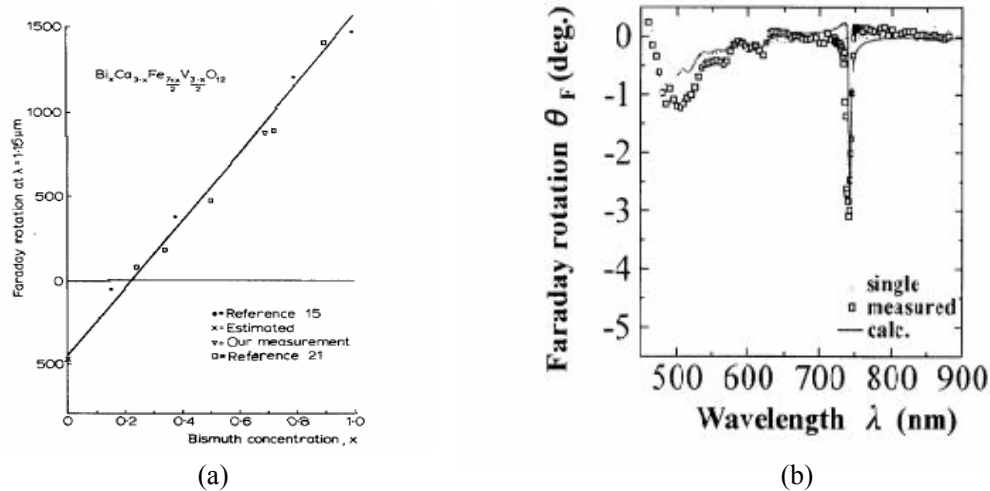
Figure 1.3 *Enhancement of FR by (a) bismuth substitution and (b) structure engineering.*

Recently, a new type of structure called magnetic photonic crystal (also called magnetophotonic crystal) was proposed by Inoue [63] and one dimensional magnetic photonic crystal with single defect was also fabricated by several authors [70-73, 76]. The Faraday rotation was increased by up to 2 orders of magnitude higher than that of Bi-YIG films of the same length (Fig. 1.3b). This structure can greatly reduce the total length required for 45° and is promising for device integration.

1.2 Structure of YIG [1]

The unit cell of YIG is cubic with space group of O_h^{10} (Ia3d). It contains eight formula units of $Y_3Fe_5O_{12}$ with a total of 160 ions. One formula unit of YIG contains three dodecahedral, two octahedral and three tetrahedral sites. Normally, garnets are represented by the following form:

$$\{C^{3+}\}_3[A^{3+}]_2(D^{3+})_3O_{12}$$
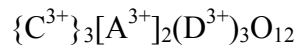
where C , A, D stands for ions that occupy different sites. Of the 160 ions, 24 Fe^{3+} occupy the tetragonal (D) sites. 16 Fe^{3+} occupy the octahedral [A] sites and 24 Y^{3+} occupy the dodecahedral {C} sites. 96 oxygen ions surround the 3 sites with coordination number of 4, 6 and 8, respectively. Fig.1.4 shows the arrangement of cations in a YIG formula unit. The lattice parameter of YIG is 12.38Å, which is very large compared to other materials. The magnitude of the saturation magnetization of the ferrimagnetic iron garnet is determined by those of the tetrahedral (Md), octahedral (Ma) and dodecahedral (Mc) sublattices as:

$$Ms = |Ma + Mc - Md| \qquad (1\text{-}2)$$

In YIG or rare earth substituted YIG there are only two sites, Ma and Md, that contribute to the magnetization since the Y^{3+} ion is non-magnetic. Fe^{3+} ions in the octahedral sites

and tetrahedral sites have opposite magnetization directions and hence the net

Figure 1.4 *Arrangement of cations in a YIG formula unit*

magnetization is in the tetrahedral direction. Each Fe^{3+} has a 0K magnetic moment of 5

Bohr magnetrons. Thus each formula unit has a $5\mu_B$ of 0K magnetic moment.

The large and open structure of YIG allows different elemental substitutions. The

substituting elements have their preferred sites depending on the atomic diameter of the

substituting ions, as shown in Fig.1.5. Substitutions result in different structural, magnetic,

optical and MO properties. Bismuth and cerium are the two most successful substitutions

that enhance the figure of merit. The FR of YIG is about 214°/cm at 1310 nm wavelength.

While the reported highest FR of bismuth substituted YIG (Bi-YIG) and cerium

substituted YIG (Ce-YIG) is 4300°/cm [23] and 4800°/cm [55] at 1550 nm, respectively.

Figure 1.5 *Elements that can be substituted into garnet and their preferred sites*

1.3 Physics of Magnetooptical effect [1-11]

1.3.1 Dielectric tensor

The propagation of electromagnetic waves in a material can be characterized by its

electric and magnetic permeability tensors $\hat{\varepsilon}$ and $\hat{\mu}$. At optical frequencies $\hat{\mu}$ can be

assumed to equal unity. The dielectric tensor is the bridge between theory and experiment

since it relates with the observable quantities, such as refractive index, absorption and FR,

etc. For materials with uniaxial anisotropy (z is the uniaxics) and magnetic field is

applied along the direction of light wave propagation (z axis), the dielectric tensor can be

written as:

$$\hat{\varepsilon} = \begin{pmatrix} \varepsilon_{xx} & i\varepsilon_{xy} & 0 \\ -i\varepsilon_{xy} & \varepsilon_{xx} & 0 \\ 0 & 0 & \varepsilon_{zz} \end{pmatrix}$$

(1-3)

Each element is a complex number and expressed as:

$$\varepsilon_{xx} = \varepsilon_{xx}{}' + i\varepsilon_{xx}{}''$$
$$\varepsilon_{xy} = \varepsilon_{xy}{}' + i\varepsilon_{xy}{}''$$

(1-4)

The imaginary part describes the absorption and the real part describes the propagation as indicated below. Gyrotropic effects, such as magnetic circular birefringence (Faraday effect), polar Kerr effect and magnetic circular dichroism are described by the off-diagonal element ε_{xy}, which is the only element that depends lineally on magnetization. The diagonal elements are related to the normal refractive index n and the normal extinction coefficient k by:

$$n^2 - k^2 = \varepsilon_{xx}{}'$$
$$2nk = \varepsilon_{xx}{}''$$

(1-5)

The off-diagonal elements are related to the refractive indices $n_\pm$ and the extinction coefficients $k_\pm$ of right (+) and left (-) circularly polarized light by:

$$(n_+ - n_-) + i(k_+ - k_-) = \frac{\varepsilon_{xy}}{\varepsilon_{xx}^{1/2}}$$

(1-6)

Here we use the definition for RCP light if, on looking against the direction of propagation, the electric field rotates counterclockwise.

The Faraday rotation, θ_F, which is half of the phase difference between RCP and LCP waves, is defined as:

$$\theta_F = \frac{\pi(n_+ - n_-)}{\lambda} = \text{Re}(\frac{\pi\varepsilon_{xy}}{\lambda\varepsilon_{xx}^{1/2}})$$

(1-7)

The Faraday ellipticity η_F is related with the difference in absorption of the RCP and LCP by:

$$\eta_F = \frac{\pi}{\lambda}(k_+ - k_-) = \text{Im}(\frac{\pi\varepsilon_{xy}}{\lambda\varepsilon_{xx}^{1/2}}) \qquad (1\text{-}8)$$

As shown above, the FR is proportional to the real part of the off-diagonal element of the dielectric tensor. The dielectric tensor at optical frequency can be measured from the optical observables such as reflection, Kerr rotation, Faraday rotation, etc.

1.3.2 Microscopic origins of the Faraday effect

Understanding of the microscopic origins of the Faraday effect is based on the materials' electronic structure and electron wave functions. The selection rules for light-induced quantum transitions show that LCP and RCP induce different electronic transition, hence different refractive indices when magnetic field is applied. In non-magnetic materials at H=0, LCP and RCP obey equal transition process and consequently no FR occur.

FR spectra must be interpreted in term of electric-dipole transitions. The contribution of allowed magnetic dipole transitions are orders of magnitude smaller to account for the observed spectra. The RCP and LCP excite electron transitions, which, in accordance with the law of angular momentum conservation, change the appropriate projection of the system's angular momentum by $\Delta m=\pm 1$. The Faraday effect is then defined as the difference between the right and left transitions (with $\Delta m=1$ and $\Delta m=-1$, respectively). The selection rule for electric dipole transitions determines the left and right polarized photon will induce a transition of the ion to the state with $\Delta M=1$ and $\Delta M=-1$, respectively (M is z projection of angular momentum operator of the ion).

Two transitions that satisfy the above condition will be discussed below. Historically they have been termed as paramagnetic and diamagnetic transitions.

1). Diamagnetic transition (double transition)

The excited states are split by spin-orbit coupling, exchange splitting or Zeeman effect and produce levels characterized by M_J=-1, 0, +1. The transitions from the spin and orbital singlet ground state to the M_J=+1, -1 levels occurs via RCP and LCP, respectively. The calculated off-diagonal element takes the following form:

$$\varepsilon_{xy} = \frac{\omega_p^2 f \Delta L}{2\omega_0} \frac{(\omega_0 - \omega)^2 - \Gamma_0^2 + 2i\Gamma_0(\omega_0 - \omega)}{\left[(\omega_0 - \omega)^2 + \Gamma_0^2\right]^2} \tag{1-9}$$

Δ is the separation between the levels because of the spin orbit coupling, ω_0 and Γ_0 are the center frequency and halfwidth at half height of the transition, and it is assumed that $\Delta \ll \Gamma_0$. $\omega_p = \frac{4\pi N e^2}{m}$, where e and m are the electronic charge and mass and N is the number of octahedral Fe^{3+} ions/cm^3. f is the oscillator strength. L is the Lorentz-Lorentz local field correction and equals $\left(\frac{n^2 + 2}{3}\right)^2$.

The line shape of this kind of transition is shown in Fig.1.6.
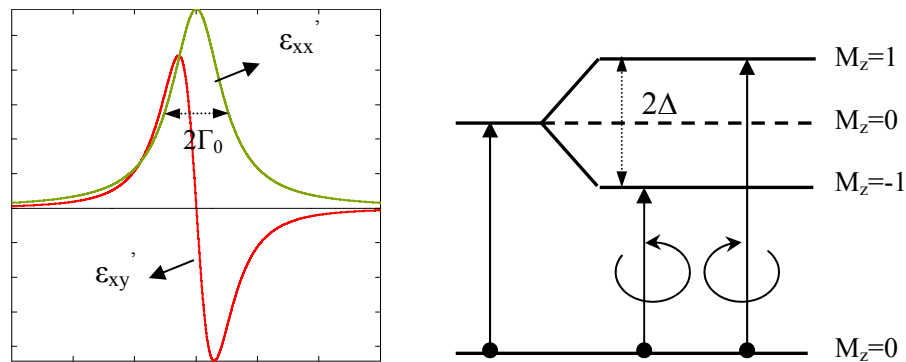
Figure 1.6 *Schematic of diamagnetic transition line shape*

2). Paramagnetic transition (single transition)

An applied magnetic field removes the degeneracy of the ground state and produces a set

of ground states, whose electronic populations are temperature dependent. As the temperature is lowered and/or field is increased, all the electrons condense in the lowest ground state. Consequently, the ground states have different transition frequencies and different populations. So the transition probabilities and hence the oscillator strengths are different for RCP and LCP for different ground states.   These kinds of line shapes are called paramagnetic transition. The off-diagonal element has the following form:

$$\varepsilon_{xy} = \frac{\omega_p^2 f df L \omega}{2} \frac{\left(\omega_0^2 - \omega^2 - \Gamma_0^2\right)^2 + i\Gamma_0\left(\omega_0^2 + \omega^2 + \Gamma_0^2\right)}{\omega_0\left[\left(\omega_0^2 + \omega^2 + \Gamma_0^2\right)^2 + 4\omega^2\Gamma_0^2\right]}$$ (1-10)

where the fractional dichroism df is defined as

$$df = \frac{f_- - f_+}{f_- + f_+} = \frac{f_- - f_+}{2f}$$ (1-11)

f_+ and f_- are oscillator strength for RCP and LCP, respectively.

The line shape of this kind of transition is shown in Fig.1.7

Figure 1.7 *Schematic of paramagnetic transition line shape*

The distinction between paramagnetic and diamagnetic transitions lies in the origin of different polarizabilities for LCP and RCP. For diamagnetic transition, it comes mainly

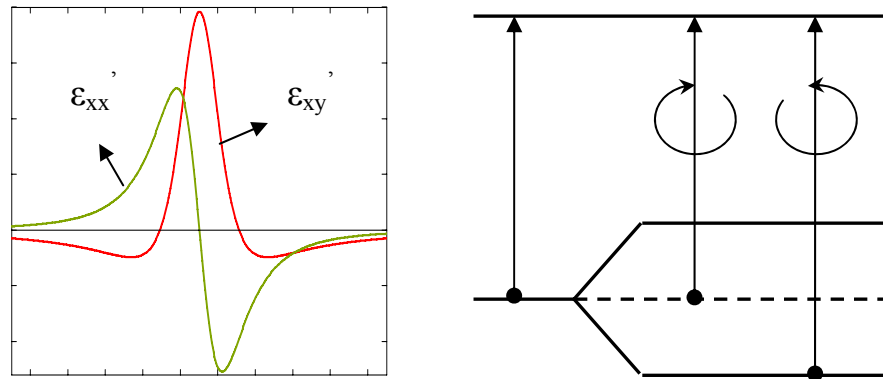from excited states splitting 2Δ. For paramagnetic transitions, it mainly comes from the different occupation numbers in the ground state and hence the different oscillator strengths f_+ and f_-.

If $\Delta \ll \Gamma_0$ is not satisfied, as argued by G. Allen and G. Dionne [9], the above theory must be modified. The off-diagonal element of diamagnetic type transition is given as:

$$\varepsilon_{xy} = \omega_p^2 \sum(\pm) \frac{f_\pm}{w\omega_{0\pm}} \times \frac{\omega(\omega_{0\pm}^2 - \omega^2 - \Gamma^2) + i\Gamma(\omega_{0\pm}^2 + \omega^2 + \Gamma^2)}{\omega(\omega_{0\pm}^2 - \omega^2 + \Gamma^2) + 4\omega^2\Gamma^2} \qquad (1\text{-}12)$$

Since ε_{xy} can be measured experimentally, theoretical curving fitting is based on these two transitions.

1.3.3　Bismuth doping and its microscopic origins

Direct evidence of the role of bismuth is observed based on (1) FR enhancement of Bi-YIG compared with pure YIG and (2) the linear dependence of FR enhancement with atomic percentage of Bi doping.

To study the microscopic origin of bismuth doping, Bi-YiG with different atomic percentages of bismuth is prepared and the absorption, $\varepsilon1'$ and $\varepsilon1''$ spectrum is compared with those of pure YIG. Bismuth doping does not create new transitions, so the enhancement of FR cannot arise from transitions within the Bi ions. The contribution of bismuth is manifested by increasing transition strength and excited state splitting that already exist in the YIG. Wittekoek [7] suggested the large FR is caused by an increase of the spin orbit splitting in the excited states caused by formation of hybrid molecular orbits between the 3d orbital in Fe^{3+} and 2p orbital in O^{2-} mixed with the 6p orbital in Bi^{3+}, which has a large spin orbit interaction coefficient. This mechanism is widely accepted [10, 11].

1.4 Motivations of current research and our approaches

Optical isolators are commercially available in bulk form. Fig.1.8a shows an isolator manufactured by Electro-optic Technology Inc. The performance of this kind of isolator has been proven to be excellent, i.e., commercially available isolator has isolator ratio range from 30 to 65 dB/cm and insertion loss from 0.2 to 1dB/cm. However, they are expensive, with the price range from several hundreds to several thousands dollars depending on isolation ratio and aperture size [78]. In addition, objective lenses are needed to couple in and out the laser beam. Periodic alignments are also required to offset the temperature or wavelength deviation.
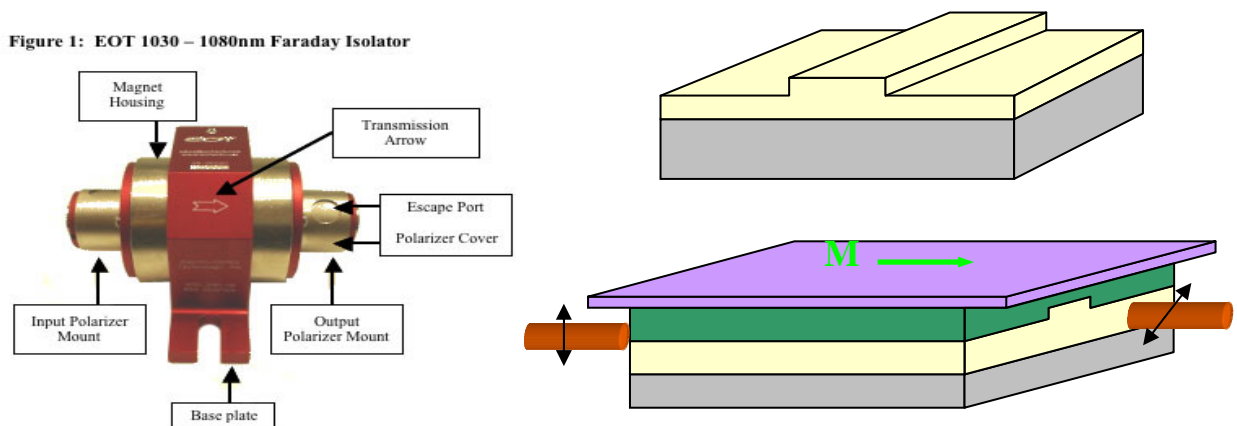
Figure 1.8 *(a) schematic of a commercial isolator (from www.eotech.com) and (b) a waveguide isolator*

To establish an affordable technique, it is essential to be able to integrate optical components, such as lasers, isolators, circulators, modulators, splitter, etc. onto a single substrate, as compared to its electronic counterpart. Thus waveguide isolators, as shown in Fig.1.8b, are desired. In this configuration, focus optics are eliminated and the isolator can be magnetized by a ferromagnetic overlayer film. This allows standard monolithic processing and reduces cost significantly.

Levy *et al* [58] have already demonstrated an integrated thin film waveguide isolator with film magnet on LPE grown garnet films. A 29 dB isolation ratio has been obtained with negligible excess loss. LPE technique has the advantage of growing high crystalline quality, in stoichiometric composition and low loss garnet films. However, the drawbacks of this technique have prevented LPE from practical application to fabricate waveguide isolators. These drawbacks include poor thickness control, high bismuth content can not be incorporated and contamination from the melt. Typical growth rate of LPE is about 1μm/min so it is difficult to precisely control the film thickness. Precise thickness control is critical to eliminate linear birefringence and achieve high Faraday rotation. High bismuth content YIG is unstable at high temperatures and can not be achieved by LPE. Lead oxide is normally added to lower the growth temperature. This environment is not friendly to semiconductor devices. New approaches should be found for waveguide isolator fabrications.

The specific Faraday rotation of YIG is 214°/cm at λ=1310nm. Depending on the amount of bismuth incorporated, bismuth substituted YIG (Bi-YIG) can increase the FR to more than 1000°/cm. A few hundred micron path-length is still needed for 45° rotation. Reduction of this length will increase packing density and thus reduce cost. One dimension magnetic photonic crystal (1D-MPC) has been shown an effective way to reduce path-length. Two structural designs have been proposed so far: one-defect (phase shift) [66-68, 70-72] and two-defect [69, 73, 74] 1D MPC. One defect structure, however, can not achieve both high FR and high transmission [66-68, 70-72]. To solve this problem, two defects structures were proposed. However, the bandwidth for FR and transmission in these cases is only a fraction of 1nm and can not withstand temperature or

central wavelength fluctuations. A new structure is needed for broadband application.

Sputtering is a technique commonly used in the semiconductor, data storage and optical coating industry. Sputtering deposition of garnet thin films has been extensively studied and good quality films have been obtained [31, 33]. Sputtering has a moderate growth rate and can precisely control film thickness. Multiple layer films can be fabricated easily by sputtering technique. In addition, the crystallization temperature for sputtering growth is much lower than that for LPE and hence it can be possibly applied to deposit crystallized garnet films on semiconductor devices. Despite these obvious advantages, the birefringence control, composition control of deposited films and multilayer single mode structure fabrication through sputtering has not been studied much or not at all. In this thesis research, the above questions are addressed in connection with RF-Magnetron sputtering.

Magnetic photonic crystal structures for flat-top rotation enhancement are also presented in this thesis. Our approach is to design multiple defects to reduce the length and expand the bandwidth for multi-channel application. Standard coupled mode theory is used to derive the analytical results and the transfer matrix method is used to simulate the spectral response.

Chapter 2

Simulation Modeling of Flat-top Response One Dimensional Magnetic Photonic Crystals

2.1 Introduction

Photonic crystals are artificially engineered structures with periodic refractive index. A photonic band gap can be created by controlling the period or lattice spacing. This phenomenon provides the capability to control and manipulate light, sending it to assigned routes and around loops and bends. Thousands of papers have been published in this field since the pioneering work by Yablonovitch [79] in 1987. However, most photonic crystals are made from dielectric materials or metals. Only a few tens of papers have been devoted to the investigation of magnetic photonic crystals [63-76] or the influence of external magnetic field on the photonic band gap effects [80-81]. I find that Ref. 82 is a good review article on magnetic photonic crystals and contains an excellent list of references.

Magnetic photonic crystals have the advantage to tune the optical properties by controlling the external magnetic field. Of all the potential applications of MPC, FR-enhanced isolators are the most promising one. Theoretical calculations [63-69] and experimental work [70-73, 76] have already shown a giant enhancement in FR with 1D-MPC structure. Consequent reduction in length and cost for 45° isolators is envisaged.

The magnetic photonic crystal is essentially composed of three parts: one magnetooptical layer is sandwiched between two Bragg reflectors. In this sense, the 1D-MPC operates

like a Fabry-Perot resonator. The Bragg reflectors are composed of thin layers with periodic index of refractions, n_H and n_L. Each layer is quarter wave plate, with thickness equal $\dfrac{\lambda_B}{4n_H}$ and $\dfrac{\lambda_B}{4n_L}$, where λ_B is the Bragg resonance wavelength. The Bragg reflector is totally reflective at this wavelength. Light is then trapped between the two Bragg reflector and bounce back and forth within the magnetooptical layer, thus increases the total optical path and results in the FR enhancement and also the absorption. So the MO layer should also have low absorption. Otherwise the transmission will be decreased.

Fig.2.1 shows a schematic of 1D magnetic photonic crystal with a single defect (phase shift). The so-called defect is the layer that breaks the period.

L   H   L   H   L   H   L   H   H   L   H   L   H   L   H   L
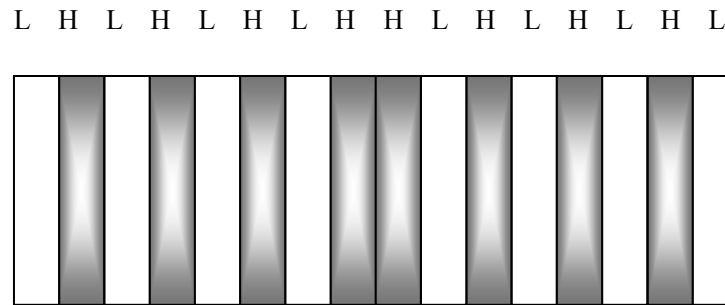
Figure 2.1 *Schematics of a single defect 1D-MPC. It composes of low refractive index (L) and high index (H) stacks, each is a quarter wave plate. The center part shows a so-called defect or phase shift.*

One dimensional magnetic photonic crystal is a relatively new concept proposed by Inoue in 1996 [63]. Only a few tens of papers have been published in this field so far. Due to the stringent fabrication tolerance, most papers are theoretical studies. Based on the structure of 1D-MPC, they can be divided into 3 categories: MPC with one defect, two defects and multiple defects.

(1)   MPC with one and two defects

Inoue theoretically studied the Faraday effect in one defect MPC structures which contain

Bi-YIG as the MO layer [63-67]. The effects of structure on the Faraday rotation were studied and they found that FR was enhanced when the structures met the non-reflection condition. In particular, the FR was increased up to 300 times [65], compared with a single Bi-YIG film, when the light is localized in the Bi-YIG layer. The stronger the localization, the larger the Faraday rotation. However, the transmissivity is found to be only 2% [66]. The subsequent studies in different groups [70-72, 76], by changing the structural designs, encounter the same problem. Several experimental works have also been carried out to fabricate one defect multiple stacks structure [70-72] by thin film deposition or planar structure [76] in our group by nanofabrication. The experimental works agree well with the theoretical calculations. Due to thickness and surface roughness control problem, the multiple stacks structures target at the visible wavelength region, while the MO properties of planar structures were measured at λ=1.55μm.

The tunablity of the one defect MPC under an external magnetic filed was also studied by Sakaguchi and Sugimoto [80]. By tuning the external magnetic field intensity below that required for saturation magnetization, the FR increases almost linearly with the increased magnetic field and the transmittance also varies linearly, except in the low magnetic field region. This is advantageous for application in magnetic field sensor.

A fatal drawback of 1D MPC with single defect is that one cannot achieve both large FR and high transmission simultaneously [66-68, 70-72, 76], which makes the application of MPC unrealistic. For example, in a device relying on the detection of the magnitude of rotation, the signal to noise ratio would be improved by the increased rotation but worsen by the overall output intensity. To solve this problem, Sakaguchi and Sugimoto [69] proposed double stack structure. They observed some improvement of the transmission

without deterioration of the Faraday rotation. For example, a transmittance of 0.765 with a Faraday rotation of 44.4 degrees was obtained. Kato [73] demonstrated that MPC operated in reflection mode could also achieve 100% transmission and 45 degree rotation. Steel *et al* [74], by utilizing the coupled mode theory, theoretically demonstrated that large FR and transmission can not be achieved simultaneously in single defect structure. The two defects design they proposed is L: fL: L with L and f can be changed freely. Effects of L and f on the transmission were discussed and explicitly explained the reasons behind FR enhancement.

There has been no experimental work done to fabricate the two-defect structure so far.

(2)   MPC with three and more defects

Although 1D MPC with two defects can obtain both 100% transmission and the required 45° for optical isolator, the transmission band is very narrow (less than 0.1 nm). Therefore, devices built upon these principles can only results in single channel operation. While growing attention on miniaturization and wavelength division multiplexing (WDM) is an integral part of the on-going drive towards expanding capacity in mass communications, this makes it essential to realize the full potential of 1D MPC as enhanced Faraday rotation elements. In addition, temperature instabilities may also result in center wavelength fluctuations. Optical transmitted power and faraday response must be made stable against wavelength and temperature fluctuations. So a new design must be realized to accomplish this. We found that three or more defects can result in broadband transmission and Faraday rotation simultaneously. This work has been published in the journal of lightwave technology [75].

2.2 Transfer matrix method and coupled mode theory

There are two methods commonly used in calculation of thin film stacks: coupled mode theory (CMT) and transfer matrix method (TMM). Both theories have advantages and disadvantages and I will briefly discuss below. I found Refs [83, 84] to be good sources for understanding of CMT and Ref [85] for TMM.
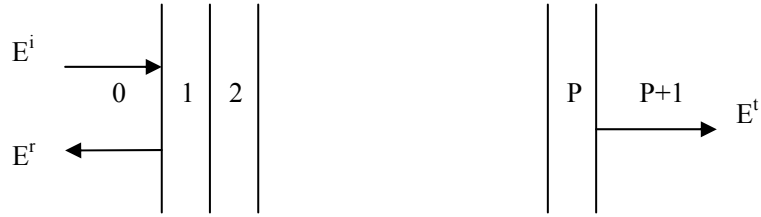
2.2.1 Transfer matrix method

Figure 2.2 *Optical configuration used in the model analysis*

Transfer matrix method is basically a finite element method in which space is divided into a set of cells. Cells are connected by continuity of electric and magnetic fields components at interfaces. So the field at one side of the structure is related to the other side by a transfer matrix T. As shown in Fig. 2.2, for a structure of P layers sandwiched between two semi-infinite media 0 and P+1, the amplitude of incident (i) and reflected (r) LCP(+) and RCP (-) electric filed in layer n-1 and n are related by transfer matrix $T^{(n-1,n)}$ by

$$
\begin{bmatrix} E_+^{i,(n-1)} \\ E_+^{r,(n-1)} \\ E_-^{i,(n-1)} \\ E_-^{r,(n-1)} \end{bmatrix} = \begin{bmatrix} T_{11}^{(n-1,n)} & T_{12}^{(n-1,n)} & 0 & 0 \\ T_{21}^{(n-1,n)} & T_{22}^{(n-1,n)} & 0 & 0 \\ 0 & 0 & T_{33}^{(n-1,n)} & T_{34}^{(n-1,n)} \\ 0 & 0 & T_{43}^{(n-1,n)} & T_{44}^{(n-1,n)} \end{bmatrix} \begin{bmatrix} E_+^{i,(n)} \\ E_+^{r,(n)} \\ E_-^{i,(n)} \\ E_-^{r,(n)} \end{bmatrix} \qquad (2\text{-}1)
$$

The elements in the transfer matrix can be expressed by indices of LCP and RCP and layer thickness. They are calculated by solving the Maxwell's equation based on the four

boundary conditions for every interface.

The transfer matrix T that relates the electric filed in layer 0 and layer p+1 is then calculated as:

$$T = \prod_{n=1}^{p+1} T^{(n-1,n)}$$

(2-2)

and the electric field is related by T as:

$$\begin{bmatrix} E_+^i \\ E_+^r \\ E_-^i \\ E_-^r \end{bmatrix} = \begin{bmatrix} T_{11} & T_{12} & 0 & 0 \\ T_{21} & T_{22} & 0 & 0 \\ 0 & 0 & T_{33} & T_{34} \\ 0 & 0 & T_{43} & T_{44} \end{bmatrix} \begin{bmatrix} E_+^t \\ 0 \\ E_-^t \\ 0 \end{bmatrix}$$

(2-3)

The transmission and reflection coefficient of LCP and RCP are then derived:

$$t_+ = \frac{1}{T_{11}}$$

$$t_- = \frac{1}{T_{33}}$$

$$r_+ = \frac{T_{21}}{T_{11}}$$

$$r_- = \frac{T_{43}}{T_{33}}$$

(2-4)

The rotation angle and ellipticity of transmitted light can be calculated from the ratio χ^t of transmitted circularly polarized electric field amplitude:

$$\chi^t = \frac{E_-^t}{E_+^t}$$

$$\theta = -\frac{1}{2} \arg(\chi^t)$$

(2-5)

$$\psi = \arctan \frac{|\chi^t| - 1}{|\chi^t| + 1}$$

2.2.2 Coupled mode theory

The coupled mode theory is an approximate method. This method permits significant simplifications in analysis without compromising accuracy of results in various geometries and is a common tool dealing with uniform waveguide and perturbations (grating).

The common derivation of CMT requires assumption of small perturbation (i.e. small index jump) and small amplitude variation so that higher order derivative vanishes. So a first order derivative equation relates the amplitude of forward (+) and backward (-) waves by detuning from Bragg resonance frequency δ and coupling strength κ can be derived.

The amplitude of incident (i) and reflected (r) LCP (+) and RCP (-) electric filed are derived as:

$$\frac{d}{dz}\begin{pmatrix} E_-^i \\ E_-^r \\ E_+^i \\ E_+^r \end{pmatrix} = i\begin{pmatrix} U_{11} & U_{12} & 0 & 0 \\ U_{21} & U_{22} & 0 & 0 \\ 0 & 0 & U_{33} & U_{34} \\ 0 & 0 & U_{43} & U_{44} \end{pmatrix}\begin{pmatrix} E_-^t \\ 0 \\ E_+^t \\ 0 \end{pmatrix}$$

(2-6)

By solving this equation, the fields at front and rear of the grating with a length L are connected by the relation:

$$\begin{bmatrix} E_\pm^t \\ 0 \end{bmatrix} = e^{U_\pm Z}\begin{bmatrix} E_\pm^t \\ E_\pm^r \end{bmatrix} = \begin{bmatrix} \cosh\sigma_\pm L + i\frac{q_\pm}{\sigma_\pm}\sinh\sigma_\pm L & i\frac{\kappa_\pm}{\sigma_\pm}\sinh\sigma_\pm L \\ -i\frac{\kappa_\pm}{\sigma_\pm}\sinh\sigma_\pm L & \cosh\sigma_\pm L - i\frac{q_\pm}{\sigma_\pm}\sinh\sigma_\pm L \end{bmatrix}\begin{bmatrix} E_\pm^t \\ E_\pm^r \end{bmatrix}$$

(2-7)

Equation 2-7 will be derived in the following section and expressions for $\sigma_\pm$, $\kappa_\pm$ and $q_\pm$ can be found there.

By solving Eq.2-7 for the unknown of $E_\pm^t$ and $E_\pm^r$, we can find the transmission and

reflection coefficient, Faraday rotation and ellipticity:

$$t_\pm = \frac{E_\pm^t}{E_\pm^i}$$

$$r_\pm = \frac{E_\pm^r}{E_\pm^i}$$

$$\theta_F = \frac{1}{2}\tan^{-1}(\frac{2\,\mathrm{Re}(\chi_F)}{1-|\chi_F|^2})$$ (2-8)

$$\eta_F = \tan(\frac{1}{2}\sin^{-1}(\frac{-2\,\mathrm{Im}(\chi_F)}{1+|\chi_F|^2}))$$

Although CMT is an approximate method, the results are surprisingly close to exact solutions. For some simple geometry, one can even extract analytical solutions. Even for higher index contrast system, i.e. YIG and SiO$_2$, the assumption is not valid; the insight and basic physical pictures remain valid.

2.2.3 Comparison of TMM and CMT

TMM is straightforward and simple for computer calculation. However, analytic solutions are impossible to be derived due to large number of matrices involved. So it provides little insight into the underlying reasons for enhancement. While CMT can simplify the system and treat a large class of structures in terms of just a few parameters, making it easier to explain the reasons behind enhancement. In addition, the CMT can be easily extended to other geometry for photonic integrated circuits, such as corrugated waveguide. But for higher index contrast structure, such as YIG/SiO$_2$, TMM is the only accurate method.

In this thesis, I will use CMT to derive the analytical solution and TMM to simulate the spectral response.

2.3 Simulation modeling and calculations

2.3.1 CMT model to derive the analytical solution

The model is based on treatment of lossless medium with cubic crystal structure. Linear birefringence is not considered in the model. The basic geometry is shown in Fig. 2.3. Linearly polarized light is incident on the magnetic photonic crystal. The
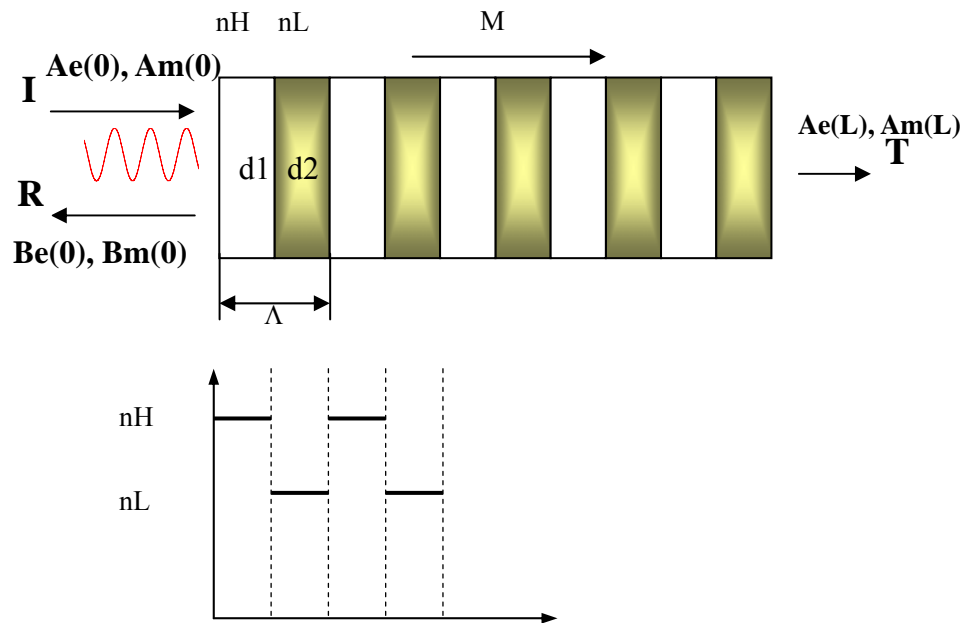
Figure 2.3 *Thin film stacks used in the coupled mode formalism*

magnetic field is applied in the same direction as the propagation direction. Due to the magnetooptical properties of the MPC, the output light is not ideal linearly polarized but with some rotation of polarization θ_F and some ellipticity η. Our aim is to find the structure that produce 100% transmission and 45° rotation required for optical isolation. For a source free media Maxwell's equations are:

$$\nabla \times E = -\mu \frac{\partial H}{\partial t} \qquad \text{(a)}$$

$$\nabla \times H = \varepsilon \frac{\partial E}{\partial t} \qquad \text{(b)} \qquad (2\text{-}9)$$

$$\nabla \cdot E = 0 \qquad \text{(c)}$$

$$\nabla \cdot H = 0 \qquad \text{(d)}$$

If we assume the field is a plane wave and has the following form:

$$\vec{E} = \{[\vec{E}_+(z)\exp(i\frac{2\pi z}{\Lambda}) + \vec{E}_-(z)\exp(-i\frac{2\pi z}{\Lambda})]\exp(-i\omega t) + C.C$$

$$= \{[\vec{x}\, Ae(z) + \vec{y}\, Am(z)]\exp(ik_B z) + [\vec{x}\, Am(z) + \vec{y}\, Bm(z)]\exp(-ik_B z)]\}\exp(-i\omega t) + C.C \qquad (2\text{-}10)$$

where $\vec{E}_+(z)$ and $\vec{E}_-(z)$ stands for the forward and backward electric fields. Ae(z) and

Be(z) are the amplitude for forward wave and Am(z) and Bm(z) are the amplitude of the

backward wave. Λ is the grating period and defined as:

$$\Lambda = d_1 + d_2 \qquad (2\text{-}11)$$

here we used the Bragg condition for gratings:

$$\lambda_B = 2\bar{n}\Lambda \qquad (2\text{-}12)$$

Now take the derivative of Eq.2-9a and substitute Eq.2-9b into it.

$$\nabla \times (\nabla \times E) = \nabla \times (-\mu \frac{\partial H}{\partial t}) = \mu\omega^2 \varepsilon E \qquad (2\text{-}13)$$

At optical frequency, we can assume $\mu \cong \mu_0$ and $\varepsilon = \varepsilon_0 \varepsilon_r$

For a biaxial anisotropy crystal when a static magnetic field is applied in the propagation

direction, ε_r is a 2nd rank tensor and takes the form:

$$\varepsilon_r = \begin{pmatrix} \varepsilon_{xx} & \varepsilon_{xy} & 0 \\ -\varepsilon_{xy} & \varepsilon_{xx} & 0 \\ 0 & 0 & \varepsilon_{zz} \end{pmatrix} \qquad (2\text{-}14)$$

So Eq. (2-13) becomes:

$$-\begin{pmatrix} \dfrac{\partial^2}{\partial z^2} E_x \\[2mm] \dfrac{\partial^2}{\partial z^2} E_y \end{pmatrix} = \dfrac{\omega^2}{c^2} \begin{pmatrix} \varepsilon_{xx} & \varepsilon_{xy} & 0 \\ -\varepsilon_{xy} & \varepsilon_{xx} & 0 \\ 0 & 0 & \varepsilon_{zz} \end{pmatrix} \begin{pmatrix} E_x \\ E_y \\ 0 \end{pmatrix}$$

(2-15)

now a grating or periodicity is introduced into the problem.

By Fourier expansion:

$$f(x) = a_0 + \sum a_k \cos(\dfrac{k\pi x}{l})$$

(2-16)

If the stack has a small index jump, two terms in Fourier expansion is a good
approximation, provided we study the frequency close to the lowest Bragg frequency.
The influence of higher Fourier compenents is largely felt at the higher Bragg resonance.
Both the diagonal and off-diagonal elements have peorid parts. So the dielectric tensor
has the following form:

$$\varepsilon_r = \begin{pmatrix} \varepsilon_{xx} + \varepsilon_{xx}' g(z) & i(\varepsilon_{xy} + \varepsilon_{xy}')g(z) & 0 \\ -i(\varepsilon_{xy} + \varepsilon_{xy}')g(z) & \varepsilon_{xx} + \varepsilon_{xx}' g(z) & 0 \\ 0 & 0 & \varepsilon_{zz} \end{pmatrix}$$

(2-17)

Where

$$g(z) = \cos(\dfrac{2\pi z}{\Lambda} + \phi) = \cos(2k_B z + \phi)$$

(2-18)

Assume a slow varying wave and discard the second derivative, we have:

$$\dfrac{\partial^2}{\partial z^2} E_x \cong [2ik_B \dfrac{dAe}{dz}\exp(ik_B z) - 2ik_B \dfrac{dBe}{dz}\exp(-ik_B z) - k_B^2 E_x]\exp(-i\omega t)$$

$$\dfrac{\partial^2}{\partial z^2} E_y \cong [2ik_B \dfrac{dAm}{dz}\exp(ik_B z) - 2ik_B \dfrac{dBm}{dz}\exp(-ik_B z) - k_B^2 E_y]\exp(-i\omega t)$$

(2-19)

Where

$$Ex = [Ae \exp(ik_B z) + Be \exp(-ik_B z)] \exp(-i\omega t)$$
$$Ey = [Am \exp(ik_B z) + Bm \exp(-ik_B z)] \exp(-i\omega t)$$

(2-20)

We can define the detuning of Bragg frequency δ as

$$\delta = k - k_B = \frac{\omega \bar{n}}{c} - \frac{\omega_B \bar{n}}{c} = k_B \cdot \Delta$$

(2-21)

where k is the wave number and Δ, $\bar{n}$ is defined as :

$$\Delta = \frac{\omega - \omega_B}{\omega_B}, \quad \bar{n} = \frac{n_1 d_1 + n_2 d_2}{\Lambda}$$

If we conside only the frequency near Bragg resonance, $\Delta \ll 1$, then

$$k^2 = k_B^{\ 2}(1 + \Delta)^2 \cong k_B^{\ 2}(1 + 2\Delta)$$

(2-22)

Now substitute Eq. 2-20 into Eq. 2-19 and discard the term involving $\exp(i3k_B z)$ and $\exp(-i3k_B z)$ since they have rapid spatial variations and presumablly unimportant. By separating the term contain $\exp(ik_B z)$ and $\exp(-ik_B z)$, we have 4 coupled equations:

$$-2i\frac{dAe}{dz} = 2\delta Ae + 2\kappa Be \exp(i\phi) + 2i\alpha_0 Am + i\alpha_1 Bm \exp(i\phi)$$

$$2i\frac{dBe}{dz} = 2\delta Be + 2\kappa Ae \exp(-i\phi) + 2i\alpha_0 Bm + i\alpha_1 Am \exp(-i\phi)$$

$$-2i\frac{dAm}{dz} = 2\delta Am + 2\kappa Bm \exp(i\phi) - 2i\alpha_0 Ae - i\alpha_1 Be \exp(i\phi)$$

$$2i\frac{dBm}{dz} = 2\delta Bm + 2\kappa Am \exp(-i\phi) - 2i\alpha_0 Be - i\alpha_1 Ae \exp(-i\phi)$$

(2-23)

Where we use the definition:

$$\alpha_0 = \frac{\pi \varepsilon_{xx}}{\bar{n} \lambda}$$

$$\alpha_1 = \frac{\pi \varepsilon_{xy}{}'}{\bar{n} \lambda}$$

(2-24)

κ is the coupling strength and for small index jump stack

$$\kappa = \frac{(n_H - n_L)\pi}{\bar{n}\lambda} = \frac{\Delta n\pi}{\bar{n}\lambda} \tag{2-25}$$

In term of left and right circularly polarized light

$$C_{\pm} = \frac{1}{\sqrt{2}}(Ae \mp iAm)$$

$$D_{\mp} = \frac{1}{\sqrt{2}}(Be \mp iBm) \tag{2-26}$$

we can write Eq.2-23 in the matrix form:

$$\frac{d}{dz}\begin{pmatrix} C_{\pm} \\ D_{\pm} \end{pmatrix} = M\begin{pmatrix} C_{\pm} \\ D_{\pm} \end{pmatrix} = i\begin{pmatrix} U^+ & V \\ V & U^- \end{pmatrix}\begin{pmatrix} C_{\pm} \\ D_{\pm} \end{pmatrix} \tag{2-27}$$

where

$$U^{\pm} = \begin{pmatrix} q_{\pm} & \kappa_{\pm}e^{i\phi} \\ -\kappa_{\pm}e^{-i\phi} & -q_{\pm} \end{pmatrix}$$

$$V = 0 \tag{2-28}$$

$$q_{\pm} = q \pm \alpha_0$$

$$q = \frac{(\omega - \omega_0)\bar{n}}{c} \tag{2-29}$$

$$\kappa_{\pm} = \kappa \pm \alpha_1$$

The field at the front and rear of the grating are connected by:

$$\begin{pmatrix} C_{\pm} \\ D_{\pm} \end{pmatrix}_{z=zf} = e^{U_{\pm}L}\begin{pmatrix} C_{\pm} \\ D_{\pm} \end{pmatrix}_{z=0} \tag{2-30}$$

$U_{\pm}$ is a matrix. To solove the equation, we use the Pauli matrix formalism [86].

$$\sigma_x = \begin{pmatrix} 0 & 1 \\ 1 & 0 \end{pmatrix} \qquad \sigma_y = \begin{pmatrix} 0 & -i \\ i & 0 \end{pmatrix} \qquad \sigma_z = \begin{pmatrix} 1 & 0 \\ 0 & -1 \end{pmatrix} \tag{2-31}$$

If $U_{\pm}$ can be expressed as Pauli matrix form, then the equation hs been solved.

$$U^\pm = \begin{pmatrix} q_\pm & \kappa_\pm e^{i\phi} \\ -\kappa_\pm e^{-i\phi} & -q_\pm \end{pmatrix} = iq_\pm \begin{pmatrix} 1 & 0 \\ 0 & -1 \end{pmatrix} - \kappa_\pm \begin{pmatrix} 0 & -i \\ i & 0 \end{pmatrix} = iq_\pm \sigma_z - \kappa_\pm \sigma_y$$

$$= (0, -\kappa_\pm, iq_\pm) \begin{pmatrix} 0 \\ \sigma_y \\ \sigma_z \end{pmatrix} \qquad (2\text{-}32)$$

So the solution of Eq.2-30 if $U_\pm$ has the above form is:

$$e^{U\pm L} = \frac{1}{2}\left(e^{\sigma_\pm L} + e^{-\sigma_\pm L}\right) + \frac{1}{2\sigma_\pm}\left(e^{\sigma_\pm L} - e^{-\sigma_\pm L}\right)\left(iq_\pm \sigma_y + \kappa_\pm \sigma_z\right)$$

$$= \cosh(\sigma_\pm) \begin{pmatrix} 1 & 0 \\ 0 & 1 \end{pmatrix} + \frac{i}{2\sigma_\pm}\sinh(\sigma_\pm L) \begin{pmatrix} q_\pm & \kappa_\pm \\ -\kappa_\pm & q_\pm \end{pmatrix} \qquad (2\text{-}33)$$

$$= \begin{pmatrix} \cosh(\sigma_\pm L) + i\dfrac{q_\pm}{\sigma_\pm}\sinh(\sigma_\pm L) & i\dfrac{\kappa_\pm}{\sigma_\pm}\sinh(\sigma_\pm L) \\ -i\dfrac{\kappa_\pm}{\sigma_\pm}\sinh(\sigma_\pm L) & \cosh(\sigma_\pm L) - i\dfrac{q_\pm}{\sigma_\pm}\sinh(\sigma_\pm L) \end{pmatrix}$$

If there is one defect, which corresponds a π phase shift, the complete response is found from the product of indivifual matrix from each grating.

$$\begin{pmatrix} C_\pm \\ D_\pm \end{pmatrix}_{z=z_f} = e^{U_2^\pm z_2} e^{U_1^\pm z_1} \begin{pmatrix} C_\pm \\ D_\pm \end{pmatrix}_{z=0} \qquad (2\text{-}34)$$

If there are a series of gratings of length z_i, whose phase parameter ϕ changes in each section, then:

$$\begin{pmatrix} C_\pm \\ D_\pm \end{pmatrix}_{z=z_f} = e^{U_n^\pm z_n} e^{U_{n-1}^\pm z_{n-1}} \dots\dots e^{U_2^\pm z_2} e^{U_1^\pm z_1} \begin{pmatrix} C_\pm \\ D_\pm \end{pmatrix}_{z=0} \qquad (2\text{-}35)$$

2.3.2 Materials and parameters used for the simulation

The magnetic and nonmagnetic materials we choose are Ce-YIG and GGG for the simulation studies. This is because Ce-YIG has the largest FR ever reported among garnet films [55] and low absorption at optical communication wavelengths. Thus

devices built based on this material have very small dimensions. GGG are normally used as substrate to grow Bi-YIG or Ce-YIG. The lattice mismatch between GGG (12.383Å) or substituted GGG and Ce-YIG is small. So it is possible to grow thick multilayer or planar structure by thin film growth techniques, such as sputtering or laser beam ablation, etc. In addition, the index difference between Ce-YIG and GGG is not too large at λ=1.55 µm and CMT analysis can be applied.

The dielectric constants used for the calculations are ε_M = 4.884 and ε_N = 3.71, respectively, where M and N stands for magnetic and nonmagnetic materials. The magnetic layer is characterized by a dielectric tensor with off-diagonal components ε_{xy} = - ε_{yx} = 0.009i, corresponding to the published magneto-optical response of Ce-YIG at 1.55µm [55]. The corresponding refractive indices are n_M = 2.21 and n_N = 1.926. Relevant structures are symmetric and defined as $(NM)^a(MN)^b(NM)^a$ for 2 phase shifts, $(NM)^a(MN)^b(NM)^b(MN)^a$ for 3 phase shifts and $(NM)^a(MN)^b(NM)^c(MN)^b(NM)^a$ for 4 phase shifts, with a, b, c as integers indicating repetition number. Ratio f are defined as f=b/a for 3 phase shifts and f_1=b/a, f_2=c/a for four phase shifts structure. The resonance wavelength is chosen as λ_B=1.55µm.

2.4 Results and Discussions

2.4.1 One defect and two defects

For one defect structure, the transmission coefficient at resonance frequency is calculated as

$$t_{\pm} = \frac{\cosh^2(\sigma_{\pm}L_2 - \sigma_{\pm}L_1) - \sinh^2(\sigma_{\pm}L_2 - \sigma_{\pm}L_1)}{\cosh(\sigma_{\pm}L_2 - \sigma_{\pm}L_1)} = \frac{1}{\cosh(\sigma_{\pm}L_2 - \sigma_{\pm}L_1)} \qquad (2\text{-}36)$$

It is clearly shown in Eq.2-36 that L_2 should be equal to L_1 in order to achieve the 100%

transmission. In other words, the structure should be symmetric.

For 2 defect structure, the transmission coefficient near resonance frequency is:

$$t_{\pm} = \frac{1}{\cosh(2\sigma_{\pm}L_1 - \sigma_{\pm}L_2) - i\frac{q_{\pm}}{\sigma_{\pm}}\sinh(2\sigma_{\pm}L_1 - \sigma_{\pm}L_2)} \qquad (2\text{-}37)$$

It is clear shown from Eq. (2-37) that the condition $L_2 = 2\,L_1$ yields 100% transmission and a flat response around the Bragg resonance ($q_{\pm} \neq 0$). Notice that the transmission spectra for right and left circular modes are displaced by $2\alpha_0$ relative to each other, but the phases ϕ_+ and ϕ_- nearly overlap each other (Fig.2.4). In the above equation L_1 is the length of the outer section, $L_1 = a\,(d_M + d_N)$, and L_2 the length of the central section, $L_2 = b\,(d_M + d_N)$, in the two-defect structure.
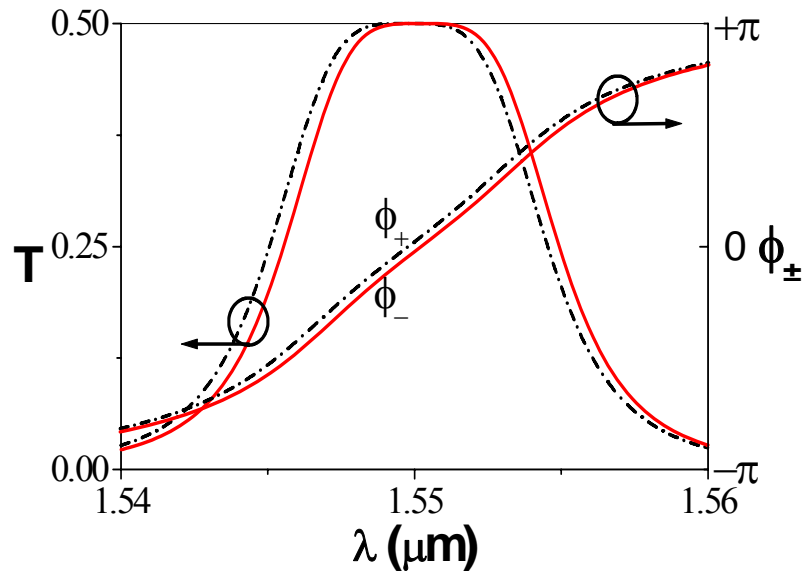

Figure 2.4 *Transmission intensity and Faraday rotation dispersion of LCP and RCP for 2-phase-shift magnetic photonic crystals with f-factor equal to 2*

To overcome the trade-off between Faraday rotation and transmission intensity for the case of two defects one needs to adjust the structure by decreasing the value of f and increasing the length of each outer segment (L_1) simultaneously. If f<2, the structure can no longer be considered as a concatenation of two identical stacks, each sub-stack

having a unit transmission resonance at the same Bragg wavelength. In this case a separation in the resonance (Bragg) wavelength for each circular polarization component becomes apparent, as shown in Fig. 2.5. This has been discussed in [74], where it is shown that resonance overlap, and therefore good transmission, can still be achieved for both circular polarization components at the center of the band by adjusting L_1 and f. But the bandwidth in such a structure remains exceedingly small and the top of the band is not flat any more.
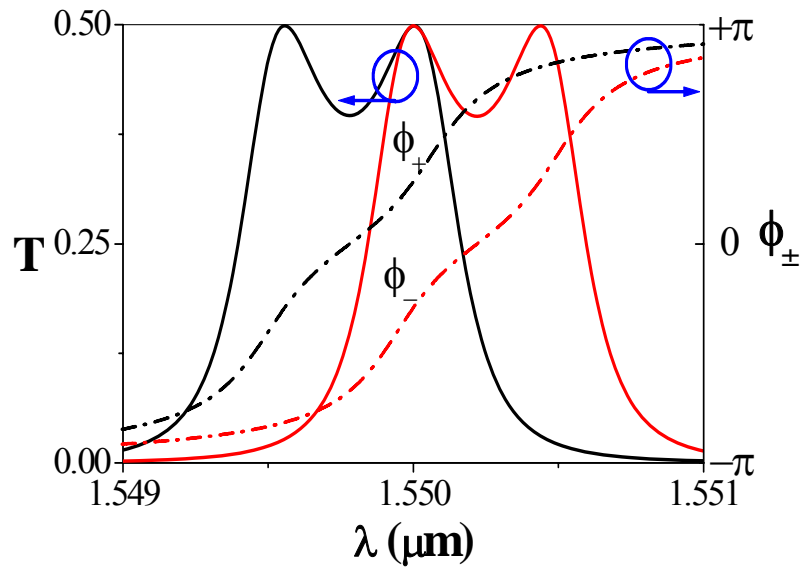

Figure 2.5 *Transmission intensity and Faraday rotation of RCP and LCP dispersion for 2-phase-shift magnetic photonic crystals with f-factor less than 2.*

2.4.2 Three and more defects structure--Flat top response

Wei and Lit have investigated the transmission characteristics of phase-shifted non-magnetic Bragg grating filters with symmetrical structures [87]. They find that two-phase-shifted Bragg filters yield perfect transmission with flattened tops when f = 2, in agreement with the discussion presented above. They also examine the case of three-phase-shifted Bragg filters and find that the optimal length ratio f_1 for flat top transmission is a function of the grating strength κL_1 and always has a value greater than

2. We extend their results to magnetic structures and examine the conditions under which multiple defects, including three- and four-defects, yield a large Faraday response in conjunction with flat top transmission. We find a minimum of three defects is needed to simultaneously optimize the Faraday response and obtain flat top transmission. Gains in bandwidth are possible and its magnitude depends on the number of defects in the structure.

The analytic solution for 3 defects is difficult to obtain. However, we can still draw some general conclusions from the simulation studies. Optimization discussions are based on tuning of ratio f and repetition number a.

(1) f is changed (a is constant and b is varied)

Figure 2.6 displays the transmittance and Faraday rotation spectral response in a 3-defect structure, for a=14 and b=26, 27, 28, 29, 30, computed by the transfer-matrix method. When f<2, the transmission is less than 100% and the transmission band is not flat. The transmission is increased if f is increased. This increase occurs first at the edge and then at the center of the transmission band. There is an optimized f that can obtain a perfect flat top response. Further increase of f beyond the $f_{optimized}$ results in decrease of transmittance and also the flatness of transmission band. The Faraday rotation increase when f is increased. The flatness of FR shows reverse response as that of transmission. It becomes more flat when f<2.

The transmission band width decrease as f is increased. For a optimized 3 defects (f=29/14) structure, it is 1.7nm with 45° of polarization rotation and a flat top spectral shape
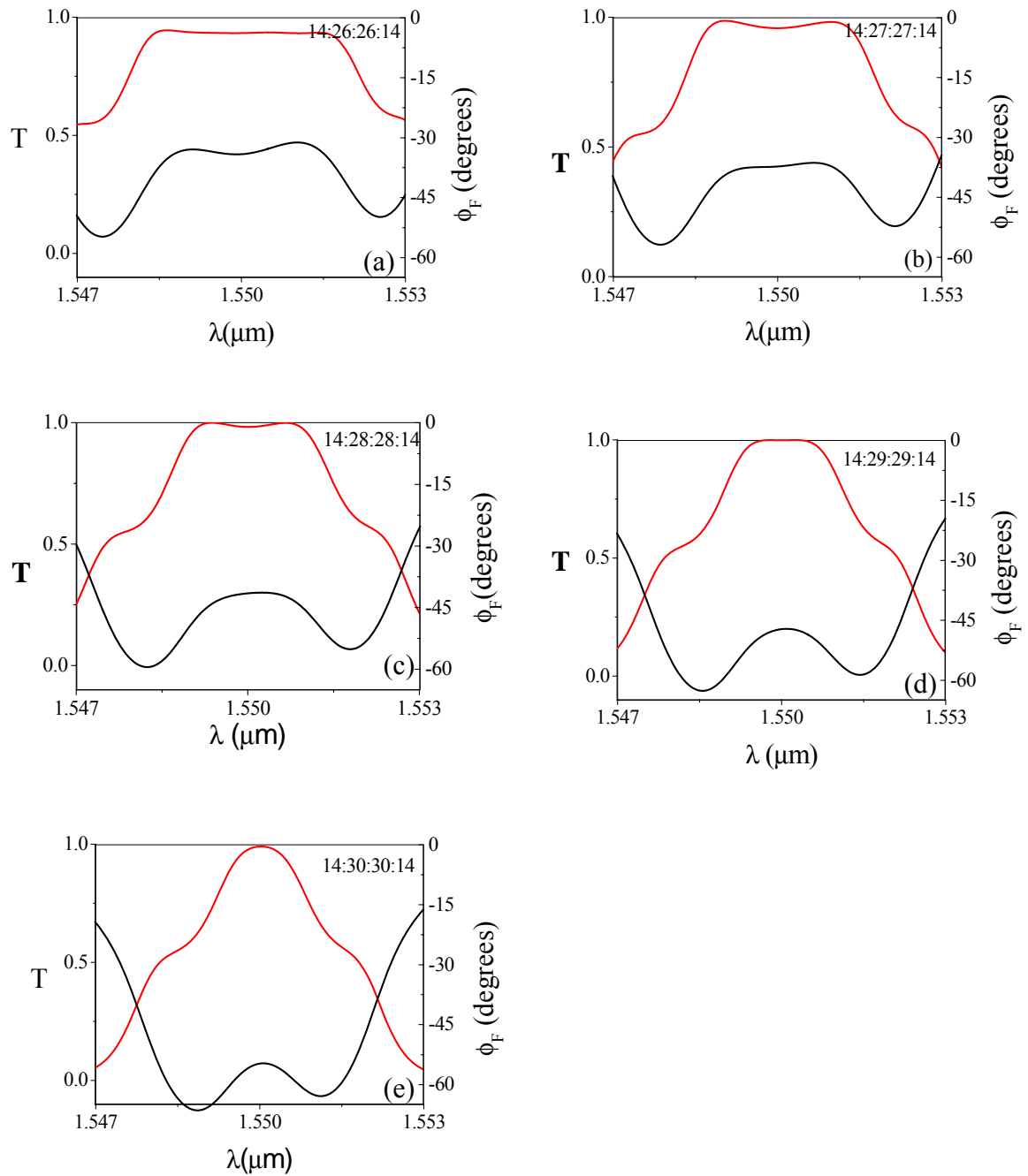
Figure 2.6 *Transmission and Faraday rotation response for a 3 defects structure. The flat-top and 45 degree rotation is obtained when it has $(MN)^{14}(NM)^{29}(MN)^{29}(NM)^{14}$. Note f should be larger than 2. However, further increase of f results in drop of both transmission and flatness.*

(2) f is constant (a and b varied simultaneously to keep f constant)

If we keep $f_{optimized}$ constant and just vary the repetition number a and b, flat-top response can always be obtained. The only change is a decrease in bandwidth. The magnitude of Faraday rotation increase when a is increased. The flatness of Faraday rotation, however, decreases.
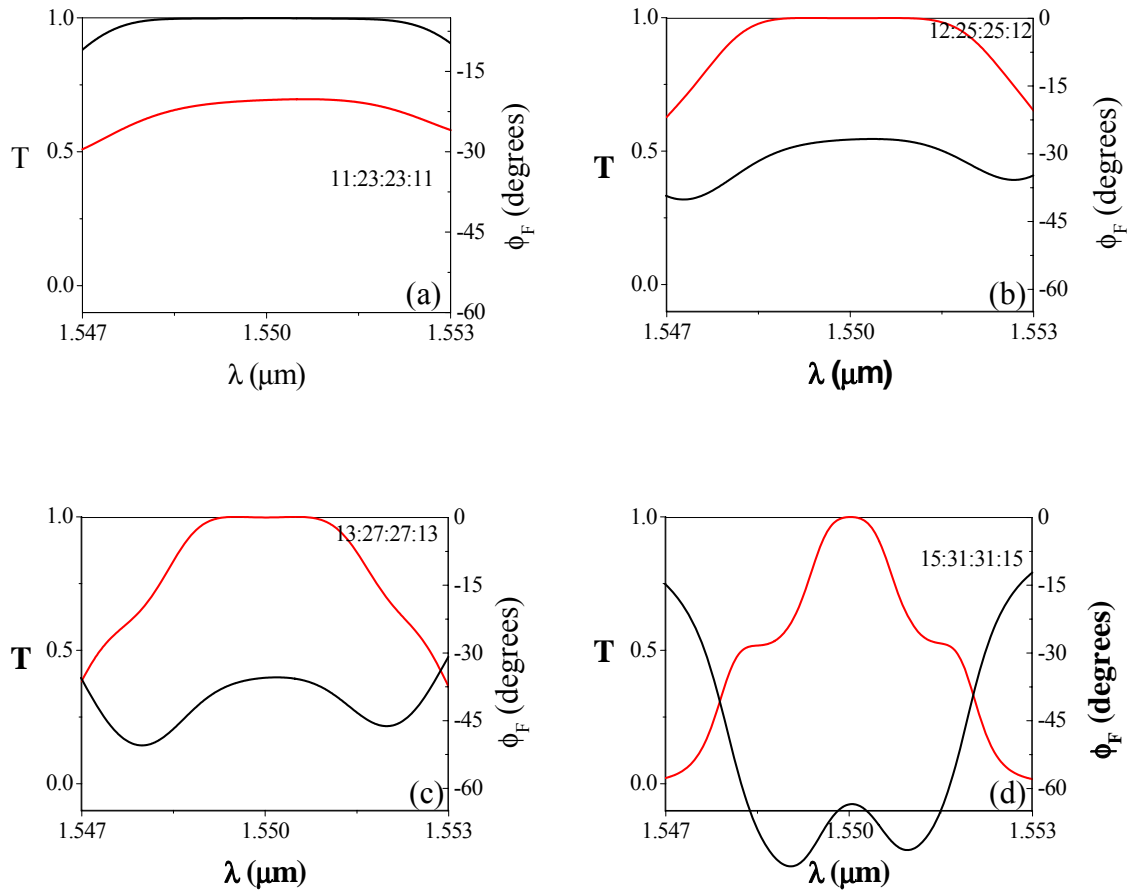

Figure 2.7 *Transmission and Faraday rotation response for 3 defects structure when f is kept constant. The flat-top is observed for all the structures. The only change is the decrease of bandwidth.*

The introduction of a 4th defect yields the optical response shown in Fig.2.8.   Here a=12, b=26, c=28, and the bandwidth is equal to 3.0nm. The ratios f_1 and f_2 are both larger than 2.   Notice, however, that the Faraday rotation is not constant across the band, deviating

by as much as 5° from the targeted 45° towards the band edge.   This sets a limit of ~ 20dB in isolation efficiency near the edges, and better than 30dB over most of the bandwidth.
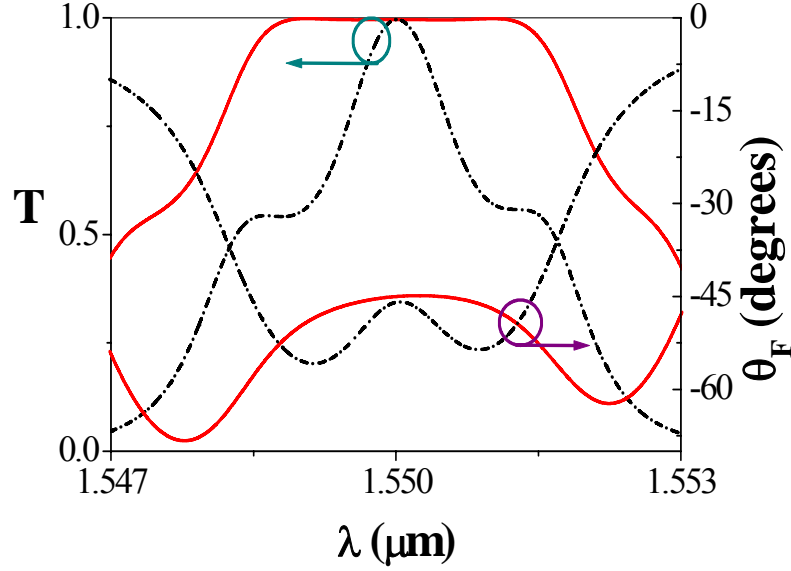

Figure 2.8 *Calculated Faraday rotation and transmittance for a 4-defect structure.   For comparison we also plot the response for a 2-defect structure, depicted by the dot-dash line. The structure for 2 defects is $(NM)^{17}(MN)^{31}(NM)^{17}$, 24.5 μm-thick.*

The spectral shape of the transmission band can be analyzed by defining a ripple factor [87]

$$R_T = \frac{I_{max} - I_{min}}{I_{max} + I_{min}}$$

(2-38)

and a Faraday rotation flatness parameter R_F (Fig.2.9) ,

(2-39)

$$R_F = \theta_{max} - \theta_{min}$$

Here, I_{max} and I_{min} correspond to the maximum and minimum transmission intensities, and θ_{max} and θ_{min} to the maximum and minimum values of the Faraday rotation angle, within the transmission bandwidth of the signal. The spectral bandwidth is defined as the full width at 95% maximum transmission intensity. The 95% value is chosen because it

lies beneath the intensity ripples considered here. These parameters track the spectral flatness of the transmission intensity and Faraday rotation.
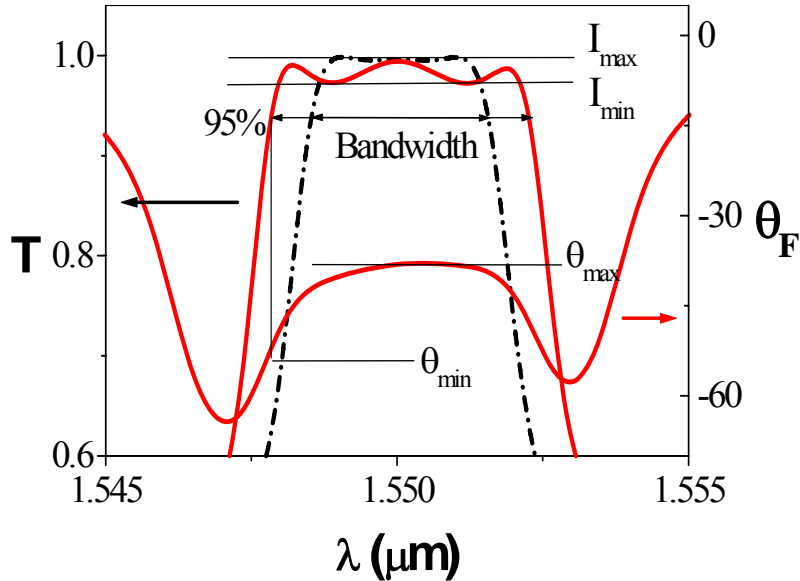

Figure 2.9 *Illustration of ripple effect for transmission and Faraday rotation dispersion. The structure is $(NM)^{12}(MN)^{25}(NM)^{26}(MN)^{25}(NM)^{12}$. The dot-dash line in this figure corresponds to the structure $((NM)^{12}(MN)^{26}(NM)^{28}(MN)^{26}(NM)^{12}$, with 45° Faraday rotation.*

Figure 2.10 shows the f_1-dependence of R_T and R_F for the case of three (a) and four (b) defects, respectively. It is clearly shown that a flat top develops for $f_1 > 2$, in contrast to f = 2 for two defects. There is an improvement in the Faraday rotation uniformity beyond $f_1 = 2.05$ that correlates with the calculated linear drop in spectral bandwidth, shown in the inset. Thus, for three-defects, a 1.7nm bandwidth flat top would support a 4° deviation in Faraday rotation angle around the targeted output polarization orientation. Notice, however, that the ripple factor is affected more strongly by bandwidth depletion in the four-defect configuration. Thus, bandwidth depletion yields smaller ripple.
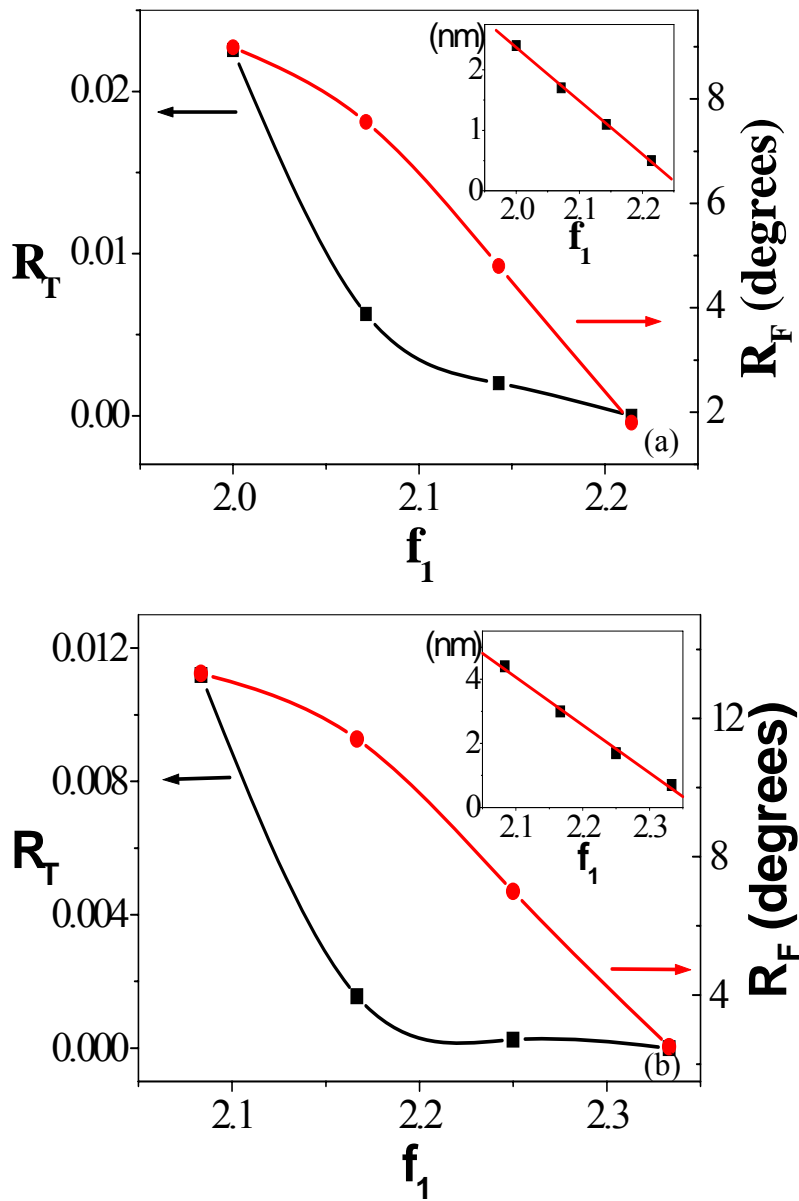
Figure 2.10 *Transmission intensity ripple factor and Faraday rotation flatness parameter for three (a) and four (b) defects as a function of the ratio $f_1 = b/a$. The insets show bandwidth dependence on f_1.*

We also plot the Faraday response as a function of length $L_1 = a (d_M + d_N)$ in Fig. 2.11 (typically $d_M \sim 175$ nm and $d_N \sim 200$ nm.). L_1 is the length of the outer section of the crystal. The plot is given in terms of the parameter a, for flat top transmission bands in

four-defect photonic crystal structures. Notice that θ_F is a function of a, so that this parameter can be adjusted to meet the rotation angle requirements of the device. In this figure 2a+m, m = 1, 2 and 3, correspond to the parameter b, with c = 2(b – a).   c is chosen to yield the smallest ripple R_T in each case. The bandwidth increases and the Faraday rotation decreases with the length of the outer region L_1, and with the f_1 factor, f_1 = 2 + m/a.
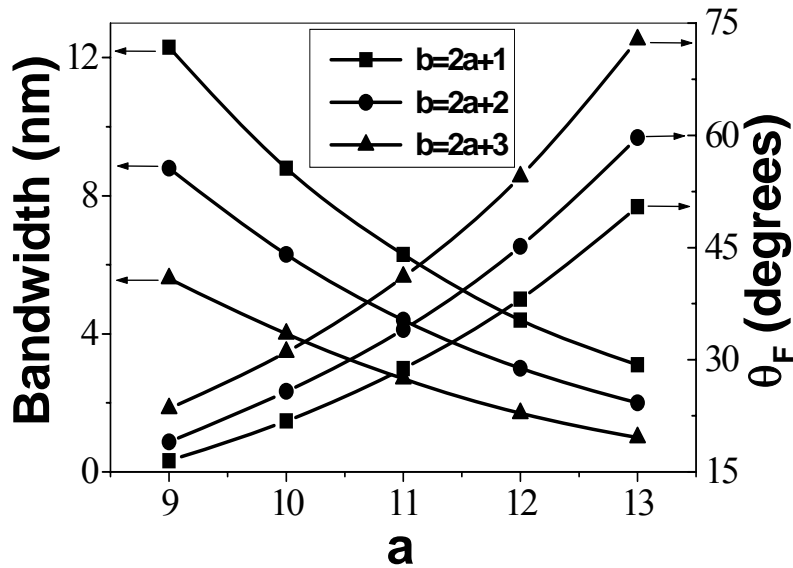

Figure 2.11 *Dependence of Faraday rotation on outer-section-length of Ce-YIG/GGG photonic crystal (parametrized by the repetition index a) for four-defect photonic crystal structures.   The response for different central-region lengths is plotted for comparison*

Table 2.1 summarizes the thickness and bandwidth response for structures containing up to 7 phase shifts. A linear increase in bandwidth with number of defects and number of layers is shown in Fig. 2.12, for up to ~7nm-bands. The value of the a-parameter for 3, 4, 5, 6, and 7 defects is 14, 12, 11, 10, and 9, respectively.

Table2.1 Design of 1D MPC with 100% transmission and near 45° rotation for up to 7 defects structure. The number of layers, total thickness and bandwidth are listed.

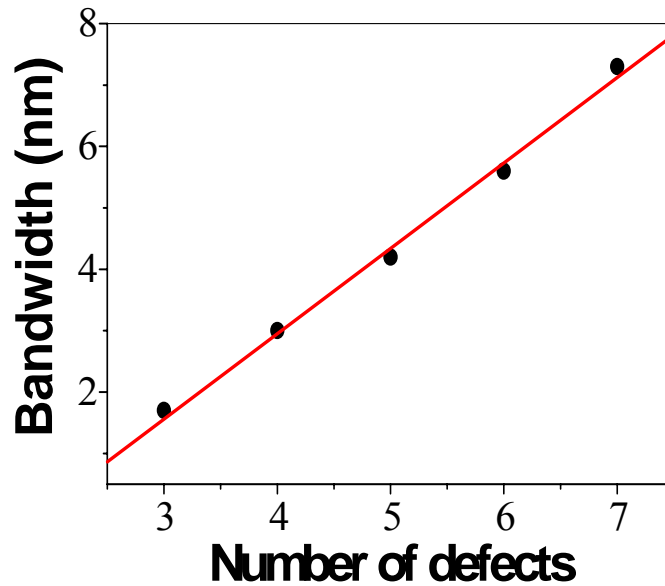| Number of defects	Number of layers	Thickness (μm)	Bandwidth (nm)	FR at 1.55μm (deg)
3	86	32.4	1.7	45.6
4	104	39.2	3.0	45.0
5	124	46.7	4.2	45.8
6	140	52.7	5.6	47.4
7	152	57.2	7.3	44.1

Figure 2.12 *Bandwidth dependence on number of defects and layers shows linear relationship dependence*

Increasing the number of layers would, of course, complicate the fabrication process. In-situ surface smoothing may be required to maintain layer thickness uniformity and film crystallinity. Suitably, it has been reported that one can obtain a significant reduction in surface roughness (down to 0.4 nm) in sputtered Ce-YIG films by ion-beam etching at 0.2 keV [34]. At the same time, the formation of multiple garnet layers with superior magneto-optic properties embedded in dielectric layers such as silicon dioxide, has been shown to be problematic[66, 70, 71]. Although GGG/Ce-YIG multi-stack formation may

prove less complicated, a simpler solution may be the patterning of planar photonic crystals on a single Ce-YIG layer.

All the results presented above correspond to lossless propagation in the material. Typically the material loss in Ce-YIG at 1.55 μm is ~10 dB/cm [32, 55]. Its effect on transmitted power would correspond to a decrease of less than 0.1 dB for three and four-phase-shift structures. This is ordinarily a negligible effect on optical isolator performance. Moreover, the added absorption would only introduce a characteristic phase shift of ~ 0.7° in circularly polarized propagation over the length of the optical path for the structures of interest, which is inconsequential to the interference phenomena comprising the flat top response.

The diffraction characteristics of non-guided waves across a magneto-optic film are of significance because they affect the type of isolator devices that can be engineered on the basis of magnetic photonic crystals. Sakaguchi and Sugimoto point out that the possibility of realizing a Faraday rotation of 45° through a magnetophotonic film several microns thick "means that there would be no diffraction-induced optical loss if it were inserted in a waveguide device to form an optical isolator." [69] We have simulated the propagation of non-guided waves across the 30.3μm-thick 3-defect structure described above, with layer numbers a=14 and b=29. The calculation uses a finite-difference time-domain (FDTD) technique developed by R-Soft, Inc. It simulates the electromagnetic field as a function of time and space based on a given input excitation. Gaussian beams with 7 μm-wide beam waists at 1.55μm
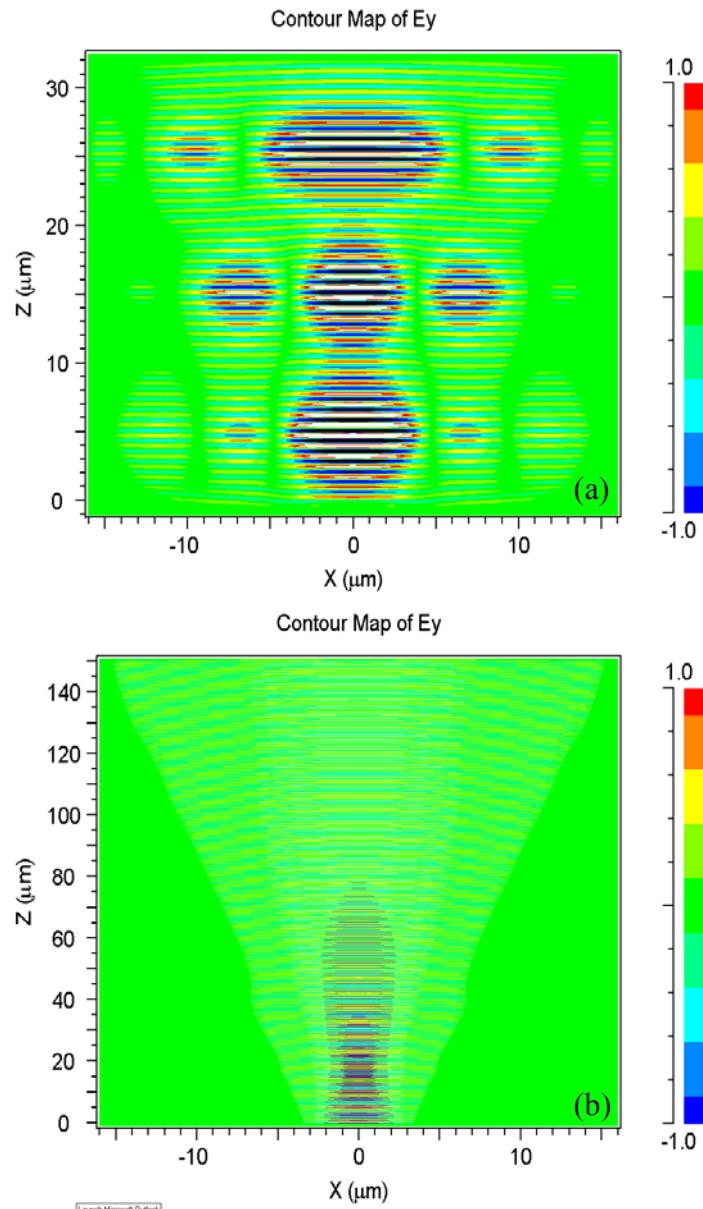
Figure2.13 *Contour maps for the beam-propagation simulation of a 3-phase-shift photonic crystal. The cross-sectional beam width at the output of the photonic crystal (a) is found to approximate that of the uniform (non-layered) material for an optical path length of ~100±20 μm (b), rather than the 30.3μm-thickness of the flat top structure*

operating wavelength are launched, which is typical for waveguide devices. We simulate the continuous wave (CW) propagation in the proposed structure and the resulting field distribution is plotted in Fig.2.13. As expected, no significant reflected light is observed at the input. It should also be noted that the field within and outside

the flat top structure does not have a Gaussian distribution anymore due to diffraction of the input beam. In order to estimate the effective optical path length in the proposed structure, propagation through a uniform Ce-YIG crystal is also simulated for comparison. The cross-sectional beam width at the output of the photonic crystal is found to approximate that of the uniform (non-layered) material for an optical path length of ~100±20 μm, rather than the 30.3μm-thickness of the flat top structure. This means that the optical path within the proposed structure is larger than its film thickness. Thus optical isolators based on a magnetic photonic crystal Faraday rotator must use collimated or waveguided beams to avoid optical loss if the light should couple back to ridge or channel waveguide structures.

Finally, we have also estimated the effect of thickness fluctuations on the structures in question. Typically, we find that a small systematic deviation of up to 0.3% (0.6nm) in layer thickness will not affect device performance. However, correlated departures of more than 1% (2nm) per layer will strongly affect the Faraday rotation response of the device, although not the spectral flatness or transmission efficiency (Fig.2.14). On the other hand these structures are more tolerant to random fluctuations in layer thickness. Thus, random fluctuations up to 5% (10nm) would still yield small changes in spectral flatness (<5%), forward loss (<5%) and isolation efficiency (<2dB). The requisite single-layer thickness uniformity in this case is within achievable limits in sputtered structures. A planar structure fabricated by E-beam lithography or focused ion beam (FIB) etching techniques would also satisfy the thickness fluctuation requirement. Single defect structure has already been successfully fabricated in our group by FIB [76]. 2 or more defects are currently in progress.
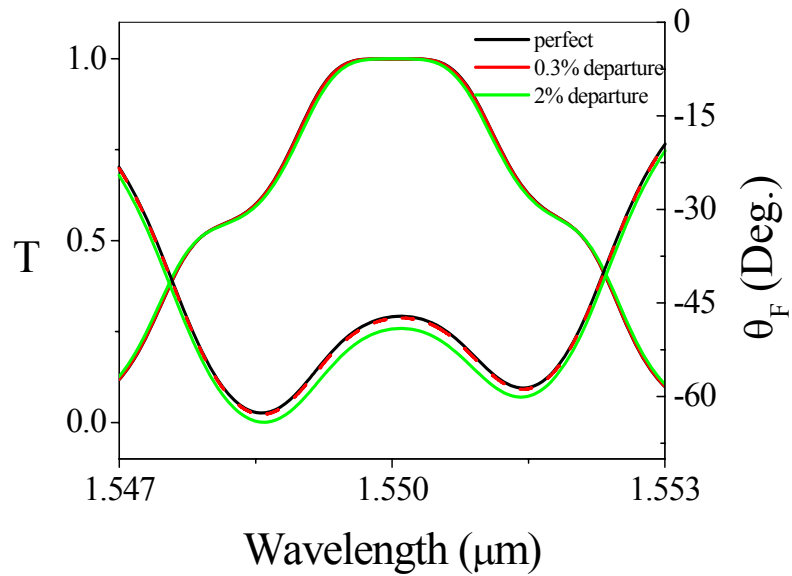
Figure 2.14 *Effect of systemic thickness fluctuation on spectral response of 1D MPC. For 0.3% departure, there is little effect on the performance. For 2% departure, the Faraday rotation response is strongly affected while the transmittance remains flat.*
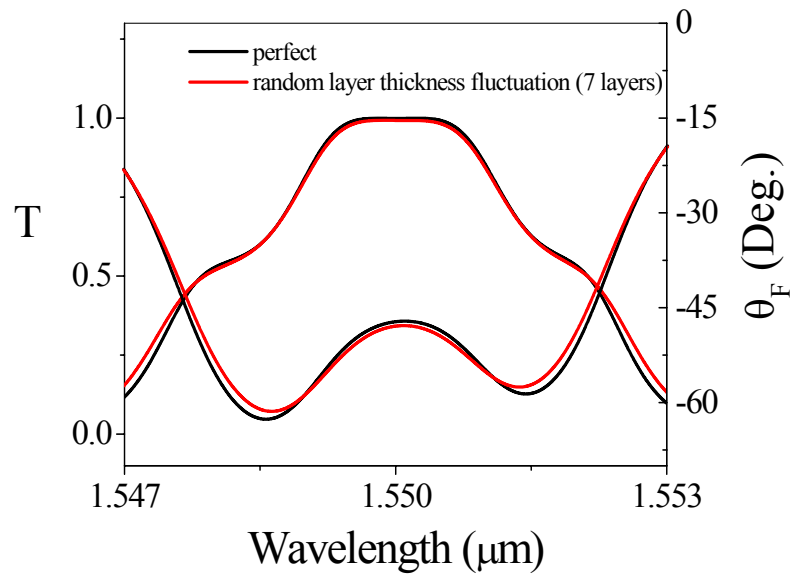

Figure 2.15 *Effect of random layer thickness fluctuations on spectral response of 1D MPC with 5% deviation for 7 layers. The device performance is more tolerant for random layer thickness fluctuation than systematic thickness deviation*

Chapter 3

Garnet Thin Films Growth and Characterization Techniques

3.1 Magnetic garnet thin films epitaxial growth methods

To realize the integrated on-chip isolators, magnetic garnet thin films with suitable Faraday rotation must be fabricated. There are a few methods used to fabricate thin film garnet. Table 3.1 lists the three major methods (LPE, PLD and Sputtering) and compares the advantages and disadvantages of these methods. There are some other methods used in fabricating garnet films, including MOCVD [47], pyrolysis [48], crystal ion slicing [49] and sol-gel [50]. However, they have not gained much popularity and will not be discussed here.

3.1.1 Liquid phase epitaxy (LPE)

The liquid phase epitaxy (LPE) method was first applied to grow garnet films in 1968 [88] and became the most widely used method due to its crystalline perfection and high growth rate (1μm/min) (It is the only commercially available technique to fabricate film type Faraday rotators). LPE is a technique that can grow high quality films at temperature well below the melting temperature of the crystal by adding a low melting temperature element to the melt. For example, lead oxide mixed with boron oxide is normally added to grow garnet crystal. A single crystal garnet substrate is dipped into the undercooled solution and rotates at certain speed. After the growth process is over, the film is pulled out to just above the melt and rotates to spin off the excess melt. Film thickness can be roughly controlled by rotation speed and content of bismuth incorporated can be controlled slightly by undercooling conditions. The composition of the grown crystal can

be maintained in stoichiometry as that of solution since it is a thermal equilibrium method. However, this method has some inherent drawbacks. First, Bi^{3+} has a large ionic radius of 1.17Å compared to 0.95Å of Y^{3+}. This results in very large lattice constant expansion. At high temperature combinatorial entropy becomes energetically favorable and makes full bismuth substitution of yttrium into a nonequilibrium phase. Second, LPE has a very high growth rate, typically 1 μm/min. It is difficult to precisely control film thickness, which is critical to eliminate linear birefringence, as will be discussed in chapter 5. Third, lead is highly toxic and environmental protection is a concern. In addition, lead can also increase the optical absorption. Although lead free LPE technique to grow garnet films has been developed [89], the first two problems are still need to be concerned.

3.1.2 Pulsed Laser deposition (PLD)

Recently, pulse laser ablation (PLA) or pulsed laser deposition (PLD) has gained popularity [36-46] in research labs after its successful application to high temperature superconductors [90]. A laser beam transfers energy into thermal, chemical and mechanical energy in the target and results in material ablation. One of its major advantages is congruent evaporation, which is a nonequilibrium process. Hence, the method can grow high Bi substituted YIG. In comparison to other techniques, PLD also has the advantages of using laser radiation as a source of "pure" energy: film contamination can be reduced to the lowest level. However, the ablation process includes large particulates and molten droplets [36, 37, 44], resulting rough surface. Structural inhomogeneity was also reported by some authors [46, 91, 92]

3.1.3 Sputter deposition

Sputtering is a physical vapor deposition method. First discovered in 1852 and then developed as a thin film deposition technique by Langmuir in the 1920s, sputtering is the primary technique for metal deposition in modern silicon-based technologies and also widely used for other thin film depositions. A sputtering system consists of a vacuum chamber, an anode (substrate) and a cathode (target), normally faced to each other. The electric field between anode and cathode accelerates the electrons which ionize Ar to Ar^+. These charged particles (also called projectiles) are then accelerated by the electric field: the Ar^+ towards cathode and e^- towards anode. When an Ar^+ ion approaches target surface, one of the following may occurs:

    i.   It may undergo elastic collision and reflected

    ii.   It may undergo inelastic collision and get buried into the target

    iii.   It may produce structure rearrangement in the target material

    iv.   The impact may result a series of collisions between incident ion and target atoms and ejection of one or more atoms from the target material. This phenomenon is termed sputtering.

The sputtered atoms or particles will travel through space and then condense on the substrate surface to form films.

Sputter deposition of thin film garnet has been studied for decades. Good quality thin film garnets have been achieved by sputtering [31, 33]. One of the advantages of sputtering is precise thickness control capability. Since it is a nonequilibrium process, all bismuth substituted garnet ($Bi_3Fe_5O_{12}$, BIG) can be obtained by sputtering [23]. However, this technique suffers from large deviation of film composition from that of the target.

Table 3.1 Comparisons of 3 commonly used methods to deposit thin film garnet: advantages and disadvantages

Liquid Phase Epitaxy (LPE)	Pulsed laser deposition (PLD)	Sputtering
Can not incorporate high Bi	Yes	Yes. High Bi and Ce incorporation
Need lattice matched substrate	Not required	Not required
Impurity in solution (Pb)	High purity	No contamination
Coarse thickness control	Coarse thickness control	Fine thickness control
Multilayer fabrication difficult	easy	Easy multilayer fabrication
Not suitable for on-chip device integration		Yes. Can sputter garnet film on semiconductor substrate
In stoichiometric composition	Off stoichiometry	Hard to maintain stoichiometric composition
Very high crystalline quality	Good crystalline quality	Very good crystalline quality

3.1.4 Description of our sputter deposition system and sputtering conditions used

Fig.3.1 shows the schematic drawing of our RF-Magnetron sputtering system. Two targets are installed; with left side has stronger magnetic field strength than that of right side. The substrate holder can be rotated by 180 degree and face to either target during sputtering.

Sintered ceramic target of 2 inches in diameter and a quarter inch in thickness with nominal stoichiometric compositions of $Bi_{0.8}Y_{2.2}Fe_4Ga_1O_{12}$, $Bi_{0.8}Y_{2.2}Fe_{4.8}Ga_{0.2}O_{12}$, $Bi_{0.8}Y_{2.2}Fe_5O_{12}$ and $Bi_{0.7}Yb_{2.3}Fe_5O_{12}$ are used as targets. The distance between target and substrate are adjusted from 3.7cm to 4.0 cm for left side target and 4.0cm to 5.0cm for right side. The base pressure is lower than 10^{-6} Torr. (111) single crystal $Gd_3Ga_5O_{12}$ (GGG) substrate of $1cm^2$ square cut along [110] and [112] directions is adhered to the substrate holder with silver paint. Substrates are cleaned in acetone, methanol and then de-ionized water in an ultrasonic bath before sputtering. The substrate is heated at
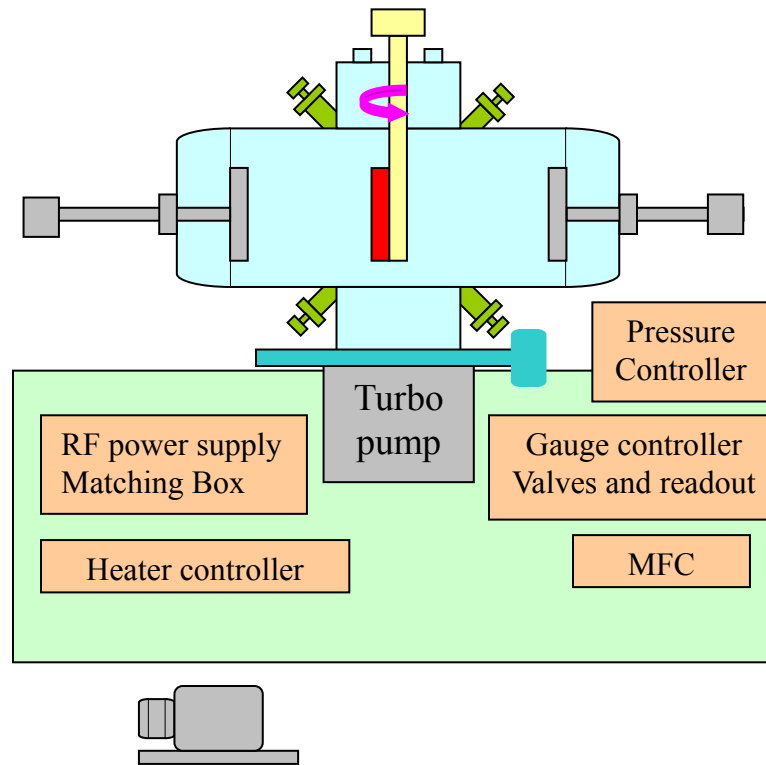
Figure 3.1 *Schematic drawing of our sputtering system*

around 200°C during the pumping process to further clean the substrate. The substrate holder is spring loaded to the heater block. Due to the contact, there is about 150 $^{\circ}$C difference between the measured substrate surface temperature and the heater control temperature, which is the set temperature of the heater controller. However, the substrate surface temperature shows a linear dependence on the heater control temperature and the calibration is shown in Fig. 3.2
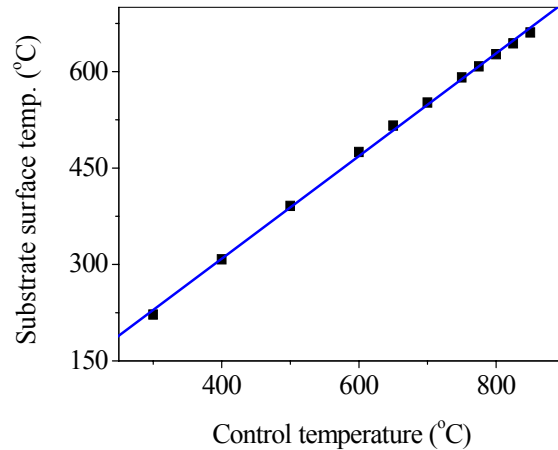
.

Figure 3.2 *Substrate surface temperature calibrated against heater control temperature. A linear dependence can be clearly seen.*

3.2 Characterization techniques

3.2.1 Crystalline structure

To characterize film crystallinity, a Scintag XDS2000 powder diffractometer and a Bede D1 high resolution x-ray diffractometer (HRXRD) were used. Powder diffractometer use Cu K_α lines which contain both $K_{\alpha 1}$ and $K_{\alpha 2}$ lines, with $K_{\alpha 2}$ line intensity normally half of the $K_{\alpha 1}$ line. Triple axis HRXRD use channel cut crystals to eliminate $K_{\alpha 2}$ line and collimate x-ray beams. 12 arcsec beam divergence can be achieved by two channel cut crystals. HRXRD also has more flexibility to do Phi scan and asymmetric scan. It was primarily used in this thesis research to accurately measure film lattice parameters.

3.2.1.1 X-Ray diffraction Geometry and scanning methods

3.2.1.1.1 Symmetric Geometry

Symmetric geometry means the experimental arrangement such that the diffracting plane is parallel to the sample surface such that the incident and diffracted beam make the same angle with the sample surface. In this case, $\theta = \omega$. An example is the scan of (444) plane for a (111) GGG substrate. Perpendicular lattice parameter of Bi-YIG film on (111) GGG

substrate can be measured by symmetric geometry as:

$$a_\perp = \frac{2\sqrt{3} \cdot \lambda}{\sin(\theta_{444})} \quad (3\text{-}1)$$

The absolute 2θ angle of the diffractometer can be calibrated and both the lattice parameters of substrate and film can be measured. However, since the film is very thin compared to the substrate, we assume that the substrate is undeformed and use the substrate as an internal standard. By measuring the peak separation Δθ between substrate and film, perpendicular lattice parameter of film is calculated as:

$$a_\perp = \frac{2\sqrt{3} \cdot \lambda}{\sin(\theta_{B\,444,substrate} - \Delta\theta)} \quad (3\text{-}2)$$
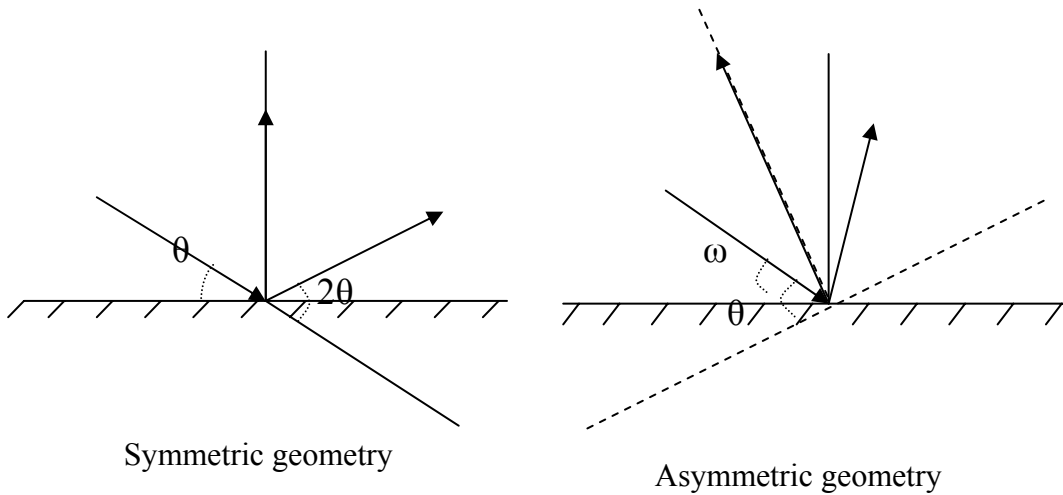

Symmetric geometry

Asymmetric geometry

Figure 3.3 Diffraction geometry for symmetric and asymmetric scan

3.2.1.1.2 Asymmetric geometry

This situation occurs when the diffraction plane is not parallel to the sample surface. An example is to measure the 880 plane for a (111) GGG substrate. In this case, $\omega = \theta - \phi$, where ϕ is the angle between diffraction plane and sample surface plane.

Combined with symmetric scan, parallel lattice constant of Bi-YIG films can be calculated as:

$$a_{//} = \frac{\sqrt{6}}{\sqrt{\dfrac{9}{d_{(110)}^2} - \dfrac{4}{d_{(111)}^2}}}$$ (3-3)

Where $d_{(110)} = \dfrac{4 \cdot \lambda}{\sin(\theta_{880})}$ and $d_{(111)} = \dfrac{2 \cdot \lambda}{\sin(\theta_{444})}$ are the d spacing for (110) and (111)

planes.

3.2.1.1.3 Scanning method

Most of the measurements were scanned with ω-2θ geometry. In this geometry, sample

and detector angles are rotated in a 1:2 ratio. Since only the separation is of interest,

substrate peaks were calibrated as 0.

3.2.2 Morphological characterization

Surface roughness is critical to propagation loss in MO devices. To measure the surface

roughness, Digital instrument Dimension 3000 atomic force microscopy (AFM) was used.

The AFM was operated with silicon tips in tapping mode. In tapping mode, the cantilever

and tip are oscillated at or near its resonance frequency as the tip raster across sample

surface. The tip lightly taps on the samples' surface. A laser beam is reflected by the

backside of the cantilever and the reflected intensity is measured by a detector. The signal

changes when the tip approaches a surface because the interaction between tip and

surface changes the resonance frequency of the tip. The roughness information is

calculated automatically by the software.

3.2.3 Compositions

The major drawback of sputtering technique for multiple components material is large

compositional deviation of deposited film from that of target. To measure the

composition, we use several techniques, including electron probe microanalysis (EPMA),

Rutherford backscattered spectrometry (RBS) and X-ray photo spectrometry (XPS) with sputtering. Microprobe measurements were carried out at Michigan Tech while samples were sent out to Charles Evans analytical group for RBS and XPS measurement.

3.2.3.1 Electron Probe Microanalysis (EPMA)

Electron microprobe is a non-destructive method for determining the chemical composition of tiny amounts of solid materials. An electron microprobe uses a high-energy focused electron beams to bombard samples' surface and generate characteristic X-rays of the elements within a sample. Chemical composition is determined by comparing the intensity of X-rays from standards (known composition) with those from unknown materials and correcting for the effects of absorption and fluorescence in the sample. The electron microprobe is designed specifically for detecting and measuring characteristic X-rays. It uses an electron beam current from 10 to 200nA, roughly 1000 times greater than that in a scanning-electron microscope (SEM). These higher beam currents produce more X-rays from the sample and improve both the detection limits and accuracy of the resulting analysis. The electron microprobe can quantitatively analyze elements from boron (Z=6) to uranium (Z=92) at routine levels as low as 100 ppm.

3.2.3.2 Rutherford Backscattering spectrometry

In Rutherford backscattering spectrometry, a high energy beam (in MeV) of particles, usually $^4He^{++}$, bombard the sample surface. These incident particles will be scattered back when they collide with the sample materials. The energy of the backscattered particles will depend on the atomic mass and also the depth of the atoms which collide with the incident particles. The backscattered energy is high (almost as high as the

incident energy) for the case of heavy target atoms such as tungsten. For the case of light target atoms such as oxygen, the backscattered energy is low. The number of backscattered ions is proportional to the square of the atomic number of the target element. Therefore we can determine the chemical composition and also the depth of various elements within the sample. A model based on the actual scattering cross section and the stopping power is used to generate a theoretical spectrum which is then adjusted until a fit is obtained to the experimental data.

3.2.3.3 XPS with sputtering

RBS can give compositional information with respect to film thickness. However, the resolution is lost when the film is thick. To better resolve the composition across film thickness, XPS with sputtering is used. XPS is based on the photoelectric effect outlined by Einstein in 1905 where the concept of the photon was used to describe the ejection of electrons from a surface when photons impinge upon it. The XPS technique is highly surface specific due to the short range of the photoelectrons that are excited from the solid. The energy of the photoelectrons leaving the sample is determined and this gives a spectrum with a series of photoelectron peaks. The binding energy of the peak is characteristic of each element. The peak areas can be used (with appropriate sensitivity factors) to determine the composition of the materials' surface. The shape of each peak and the binding energy can be slightly altered by the chemical state of the emitting atom. Hence XPS can provide chemical bonding information as well. XPS is not sensitive to hydrogen or helium, but can detect all other elements. Combined with sputtering technique, it can be used to detect the compositional variation as a function of thickness.

3.2.4 Magnetic, optical and Magneto-optical characterization

3.2.4.1 Vibrating sample magnetometer

Magnetic properties are measured at room temperature by vibrating sample magnetometer (VSM). VSM are calibrated using a Ni standard in magnetic fields parallel and perpendicular to the plane of film. The measurements were done at Texas State University, San Marcos.

In VSM, a sample is made to undergo a sinusoidal motion in a uniform magnetic field. The resulting magnetic flux changes induce a voltage in the sensing coil that is proportional to the magnetic moment of samples. The induced voltage depends on the geometry of the coils, amplitude and frequency of the vibration, and the magnetic moment of the sample. This voltage is then phase-sensitively measured using the lock-in, and read in to a computer along with the current dc-field (solenoid current) value and the outcome is an M-H loop.

3.2.4.2 Film indices, thickness and birefringence measurement

A Metricon Model 2010 prism coupler thin film thickness/refractive index measurement system with ±0.001 for film index and ±50 Å for thickness accuracy was used to measure the thickness, index of TE and TM mode. The schematics of a prism coupler are shown in Fig. 3.4a.
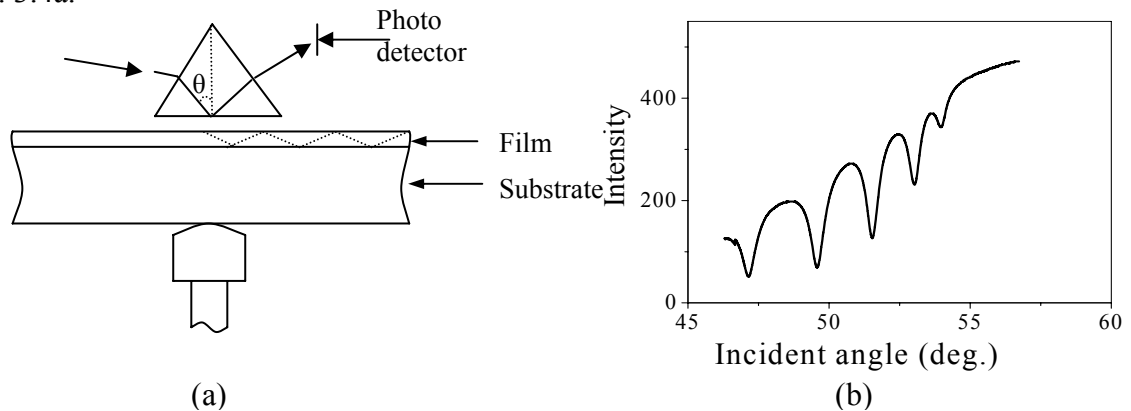

(a)   (b)

Figure 3.4 *(a) Illustration of a prism coupler and (b) measured spectrum*

A laser beam strikes the base of a high refractive index prism and is reflected onto a photo detector. At some certain θ angle, called mode angles, photons violate the total internal reflection criterion and tunnel from the base of the prism into the film and enter into propagation modes, causing a sharp drop in the intensity of light striking the photo detector (as shown in Fig.3.4b). The film thickness and refractive index can be calculated by solving the following equations:

$$k_x T = (m+1)\pi - \tan^{-1}\left(\frac{k_x}{\gamma_s}\right) - \tan^{-1}\left(\frac{k_x}{\gamma_c}\right) \qquad \text{TE Modes} \qquad (3\text{-}4a)$$

$$k_x T = (m+1)\pi - \tan^{-1}\left(\frac{n_s}{n_{0f}}\right)^2\left(\frac{k_x}{\gamma_s}\right) - \tan^{-1}\left(\frac{n_c}{n_{0f}}\right)^2\left(\frac{k_x}{\gamma_c}\right) \qquad \text{TM Modes} \qquad (3\text{-}4b)$$

Here m = 0, 1, 2… denotes the mode number, T is the thickness of the film. γ_c, k_x, γ_s are given by the following expressions:

$$\gamma_c = k_0\sqrt{n^2 - n_c^2}, k_x = k_0\sqrt{n_{0f}^2 - n^2}, \gamma_s = k_0\sqrt{n^2 - n_s^2} \;, \quad \text{where } k_0 = \frac{2\pi}{\lambda} \;, \quad \text{and } \lambda \text{ is the}$$

optical wavelength. n_{0f} is the film index, n_s is the substrate index, n_c is the cover (air) index, equal to 1, and n is the effective index of TE (n_{TE}) or TM (n_{TM}) modes.

Total linear birefringence data are measured from prism coupler fitted with rutile prisms cut at 45° and 60°. The linear birefringence is then the difference between the mode index of TE and TM modes. The birefringence is different for each mode and only the birefringence of the fundamental mode is discussed for single layer film. Following standard convention, we define the mode birefringence as positive when the index of the TE mode is larger than that of the corresponding TM mode.

The prism coupler can also be used for double layer measurement, provided the top film has a higher refractive index. Both index and thickness for each film can be measured.

The only priori knowledge required is a starting value for the lower film index. The dead

zone then allows the software to reliably separate the found modes into upper film modes

and lower film modes. If only one single mode is found for upper layer, according to Eq.

3-4, either thickness or film index is required to calculate the other parameter (index or

thickness). The measured mode index, however, is still accurate.

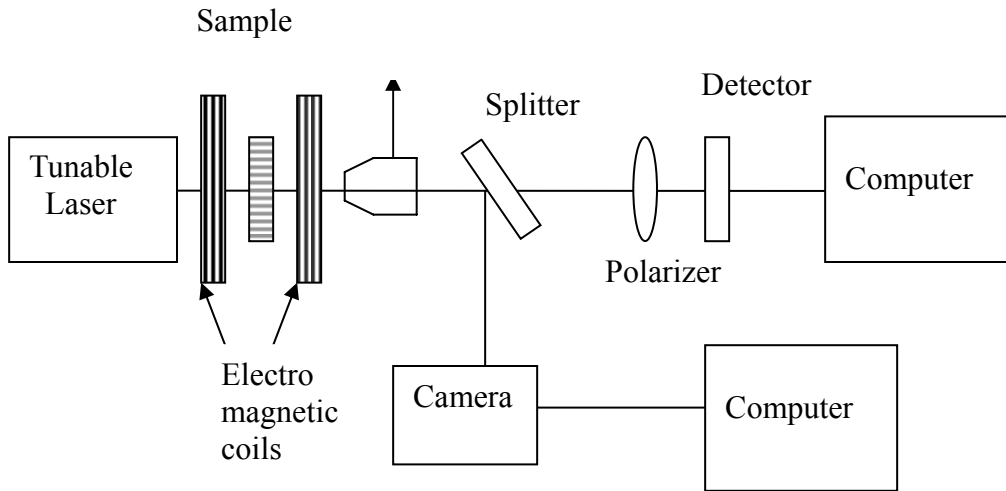### 3.2.4.3 Faraday rotation measurement

Figure 3.5 *Faraday rotation measurement set up*

Faraday rotation was measured by both perpendicular incidence and optical waveguide

coupling geometry. The perpendicular incident geometry was measured at Prof. Inoue's

group in Japan. The advantage of this method is that one does not need to worry about the

detrimental effect of linear birefringence. The drawback of this method is that the FR at

near infrared region is hard to measure due to the limited thickness. To measured the FR

at $\lambda=1.55\mu m$, ridge waveguides were fabricated by the standard photolithography and

plasma etching methods (see appendix for the fabrication process). Faraday rotation was

measured by optical fiber end butt coupling techniques. The set up is shown in Fig. 3.5.

A magnetooptical film is magnetized by the electric magnet. Before putting the sample,

the polarization plane of the polarizer is set to be perpendicular to the electric field of the incident linearly polarized beam. Thus the output intensity recorded by the detector is at minimum. If a MO waveguide is placed in the path of propagating laser beam, output intensity will increase due to polarization rotation of the incident beam. Minimum intensity will be obtained again by rotating the polarizer. The recorded rotation angle of polarizer is then the polarization rotation. The output intensity can also be recorded using a motorized polarizer. The intensity in a sinusoidal form can be recorded after the polarizer rotates 360°. The angle corresponds to the minimum intensity is then the polarization rotation. Ellipticity can also be measured by recording the maximum and minimum intensity. One major issue of the optical fiber coupling technique is the effect of linear birefringence. In order to observe the FR, linear birefringence has to be controlled as small as possible. The linear birefringence control will be discussed in chapter 5.

Chapter 4

Sputter Epitaxy of Bismuth substituted iron garnets: structural, compositional and magnetooptical studies

4.1 Introduction

4.1.1 Structural studies of sputter deposited garnet thin films

Structure and lattice deformation control of garnet thin films are very important for MO waveguide isolator applications. This is because they induce optical scattering, birefringence and magnetic anisotropy, all of which impact on isolator performance.

Besser et al. [93] studied the lattice deformation of garnet films prepared by CVD and developed a simple model. In this model, the parallel lattice constant of the film matches that of substrate. The latter is considered massive compared to the film so that it does not deform when the lattice mismatch ($\Delta a = a_s - a_f$) is relative small. The range of Δa where lattice mismatch is accommodated by elastic deformation of the film is defined as Region I. Upon increase of the mismatch above a certain value, the film is supposed to relax and become undeformed at deposition temperature. The stress is relieved possibly by formation of misfit dislocations at the film/substrate interface. This region is defined as region II. In Region I, the stress depends only on the room temperature lattice constant mismatch, whereas in Region II it is due only to thermal expansion mismatch.

The phenomenon of dual layer structure formation during the deposition process was observed in Ce-YIG system by sputtering [28, 33, 94, 95] and Bi-YIG system by pulsed laser deposition [46, 91, 92]. Throughout the literatures on the growth of $Ce_xY_{3-x}Fe_5O_{12}$ by RF sputtering heteroepitaxy on GGG and other closely related gallium-based garnet

substrates there have been a number of reports [28, 33, 94, 95] that under certain deposition conditions two distinct films with different vertical lattice constants are formed.   The consensus in the literatures has been that the difference in lattice constant between the two films is not due to compositional variations, but rather due to the separation of an initially uniform film into two films that have the same composition but differ in that the bottom layer is pseudomorphologically strained to the substrate. The top layer, on the other hand, is in a relaxed state. Besser's analysis of a single film belonging to either region I or region II has been evoked to argue that a misfit dislocation array appears in the bulk of the compositionally uniform film as a result of stress buildup during RF-sputter deposition and separates the relaxed top layer from the pseudomorphologically strained bottom layer of the film [94]. Recently, studies on PLD deposition of YIG [91, 92] observed the same phenomena. Bending of the substrate resulting from lattice constant mismatch was proposed to explain the layered structure in Ref.91. This results in discrete layers of film with different lattice parameters.

4.1.2 Compositional studies of sputter deposited garnet thin films

Normally, garnets and other multi-element compounds undergo compositional change when they are used to form films by sputtering. To reduce the compositional change, targets have been well studied and selected. However, it is still difficult to obtain the same stoichiometry as that of target due to the complexity of the garnet structure and sputtering process itself. Almost all the parameters during the sputtering process were reported to affect the composition, especially bismuth content due to low surface binding energy, of the deposited garnet films. DC self bias on the target [27], RF power [17, 21, 24], negative bias on the substrate [21], chamber pressure [24, 25], oxygen partial

pressure [16, 28], substrate temperature [16] have all been reported to influence deposited film's composition. Among these studies, only Furuya [27] proposed using low dc self bias to compensate for compositional changes. Komuro *et al* [96] reported that only garnet phases were obtained in the wide range of Fe content ranging from 3.9 to 5.4. However, strong FR and saturation magnetization only occur when film is in stoichiometry. This is more important for MO device applications at $\lambda=1.55\mu m$ since the FR is weaker at this wavelength and more vulnerable to compositional change.

Based on our studies, we find that the observed layered structure is more likely caused by compositional gradient rather than strain gradient across film thickness. In this chapter, structural and compositional profiles of deposited bismuth substituted rare earth garnet thin films are presented and compositional control of deposited garnet films are also discussed.

4.2 Structural characterizations of sputter deposited garnet films

4.2.1 Optimization of deposition parameters

To reduce the propagation loss and to lower the magnetic field required to saturate the magnetization, epitaxial growth of garnet thin films are desired. We find that bismuth substituted garnet thin films can be epitaxially grown on (111) GGG single crystal substrates provided suitable growth conditions are met. Only peaks from (444) and (888) planes are observed from XRD analysis for the symmetric scan. No other phases or peaks from the film can be detected (Fig.4.1a and b). The epitaxial characteristic can be seen from the (444) symmetric and (880) asymmetric scans from high resolution XRD (Fig.4.1c and d). However, the crystalline quality is affected by the sputtering conditions. In the following optimization studies, only one of the parameters, substrate temperature,

target/substrate distance, sputtering power/DC self bias, total chamber pressure, oxygen partial pressure was changed at a time while the other parameters were kept constant. Note also the optimization is based only on structural characterization.
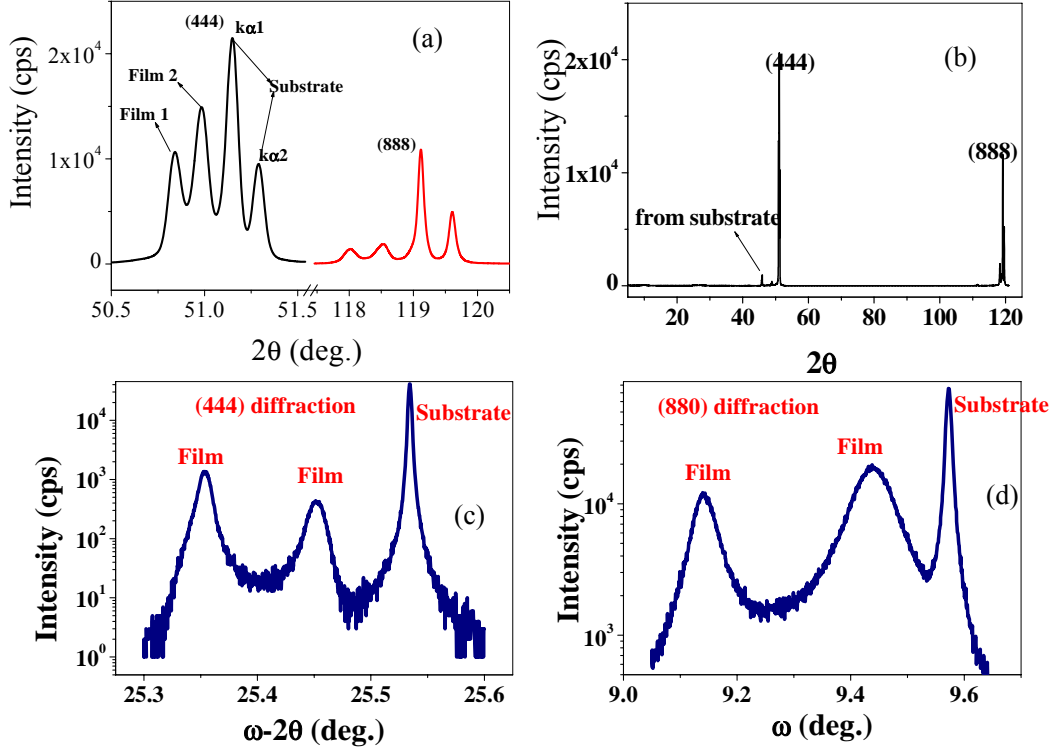

Figure 4.1 *Only (444) and (888) diffractions can be observed (a) and no other phases can be detected by the powder diffractometer. Symmetric（444）scan and asymmetric (880) X-ray diffractions from the HRXTD of sputter deposited Bi-YIG films on (111) GGG substrates clearly indicate the epitaxial growth characteristics. Two layers of films with two distinct diffraction peaks can be also seen from this graph.*

4.2.1.1 Effect of total argon sputtering pressure

XRD patterns of Bi-YIG and Bi-YbIG films sputtered under 10mTorr (sample 1), 25mTorr (sample 2) and 50mTorr (sample 3) of total chamber pressure are shown in Fig.4.2a and Fig.4.2b, respectively. Pure argon was used as the sputtering gas. The sputtering conditions are listed in Table 4.1 for Bi-YIG and Table 4.2 for Bi-YbIG. Note that the deposition rate increases slightly as pressure is decreased from 50mTorr to 10mTorr.

Table 4.1 Deposition parameters for $Bi_{0.8}Y_{2.2}Fe_4Ga_1O_{12}$ target on left side

Sputtering parameters	Experimental conditions		
	Sample 1	Sample 2	Sample 3
Working pressure (mTorr)	10	25	50
Sputtering gas	Ar	Ar	Ar
RF power density (W/cm^2)	3.95	3.95	3.95
Substrate temperature (Ts) (^{o}C)	570	570	570
Deposition rate (nm/min)	6.94	6.89	6.83
Substrate/target distance (cm)	4	4	4

Table 4.2 Deposition parameter for $Bi_{0.7}Yb_{2.3}Fe_5O_{12}$ target on left side

Sputtering parameters	Experimental conditions		
	Sample 1	Sample 2	Sample 3
Working pressure (mTorr)	10	25	50
Sputtering gas	Ar	Ar	Ar
RF power density (W/cm^2)	2.47	2.47	2.47
Substrate temperature (Ts) (^{o}C)	600	600	600
Deposition rate (nm/min)	5.25	5.21	5.17
Substrate/target distance (cm)	3.7	3.7	3.7

We find that crystalline quality decreases upon lowering Ar pressure, as seen from the peak intensity drop, for both Bi-YIG and Bi-YbIG (Fig.4.2). Meanwhile, the film peaks shift to higher 2θ angle with decrease of sputtering pressure and result in smaller vertical lattice parameters. This can be seen clearly from the high resolution XRD scan on Bi-YbIG samples (Fig. 4.2b). Films sputtered at 50mTorr show a brownish color, which is typical for heteroepitaxial bismuth substituted iron garnet films, while films sputtered at 10mTorr show a whitish color on the samples' surface. The reason is still unknown but most probably caused by antisite defect [139-141], i.e., Fe ions occupy the dodecahedral sites and cause different electron transitions and absorptions. The composition measured

by microprobe analysis does show that the increase of iron content corresponds to a decrease in yttrium content for the sputtered films. Films deposited at 10mTorr show only singlet peak while films of same thickness sputtered at 50mTorr show two peaks. This is probably due to poor film quality when films are sputtered at 10mTorr. The perpendicular lattice parameters are also found increase as sputtering pressure increase. This is caused by the combined effect of compositional change and high energy particles bombardment and will be discussed in more details in a later section.
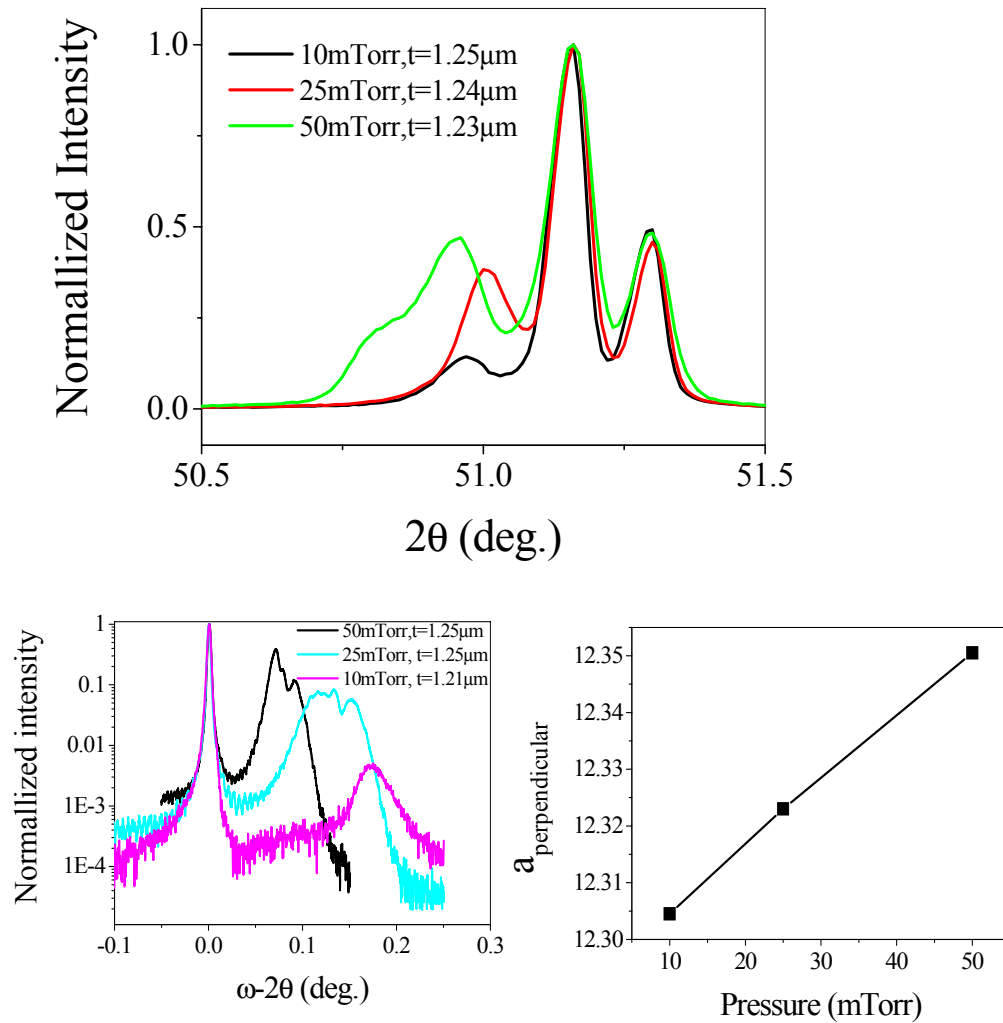
Figure 4.2 *XRD scan of Bi-YIG (a) and Bi-YbIG (b) films sputtered at 50, 25 and 10mTorr of argon. XRD peak intensity indicates the crystalline quality. The peaks shift to higher 2θ and lattice parameters increase as the argon bleeding pressure is increased.*

4.2.1.2 Effect of substrate temperature

Sputter deposited Bi-YIG film is amorphorous when the GGG substrate temperature T_{sub} is lower than $500^{o}C$. Epitaxial growth starts when T_{sub} is higher than this temperature, as implied by the appearance of a strong peak near the substrate peak. However, there is a certain range in which the garnet phase can be formed. We observe that the garnet phase disappears when T_{sub} is higher than 650 ^{o}C, as shown in Fig.4.3. The reasons that epitaxial growth disappear above $650^{o}C$ are due to re-evaporation and strong lattice vibration at higher substrate temperature.
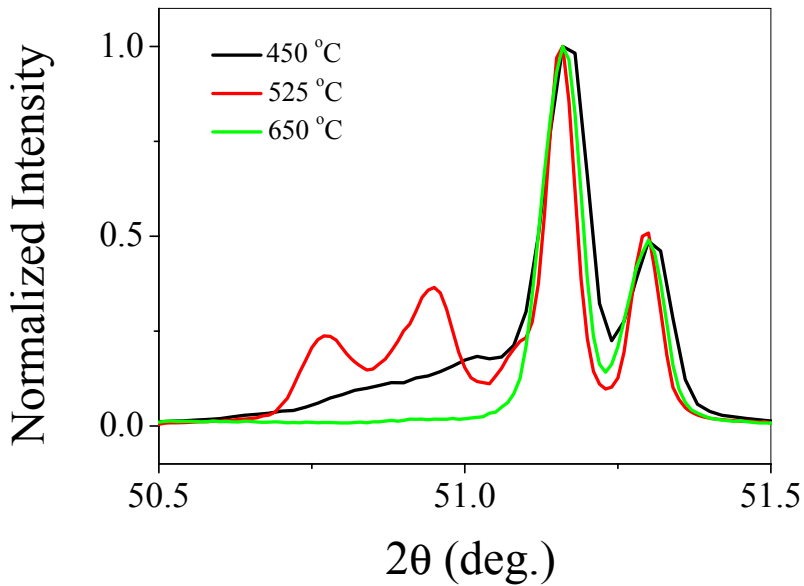
Figure 4.3 *Effect of substrate temperature on XRD pattern. For comparison, substrate intensities are normalized to 1. The garnet phase can not be formed above 650 ^{o}C or lower than 500 ^{o}C. Epitaxial growth of Bi-YIG on (111) GGG substrate occurs in between this temperature range.*

4.2.1.3 Effect of substrate/target distance

Since the permanent magnets behind the two targets have different magnetic field strength, the separation between the substrate and target for each side is set at different distances. This is because the magnetic field strength of RF magnetron sputtering influences the DC self bias: the self bias decreases as the magnetic field strength increase

[97]. Thus right side target was set at a longer distance since the weaker magnetic field at the right side. Fig.4.4 shows the comparison of peak intensity of Bi-YIG films when distances are changed from 3.7 cm to 4.0 cm for left side target and 4.5 cm to 5.0 cm for right side target. The experimental conditions are similar as those listed in Table 4.1
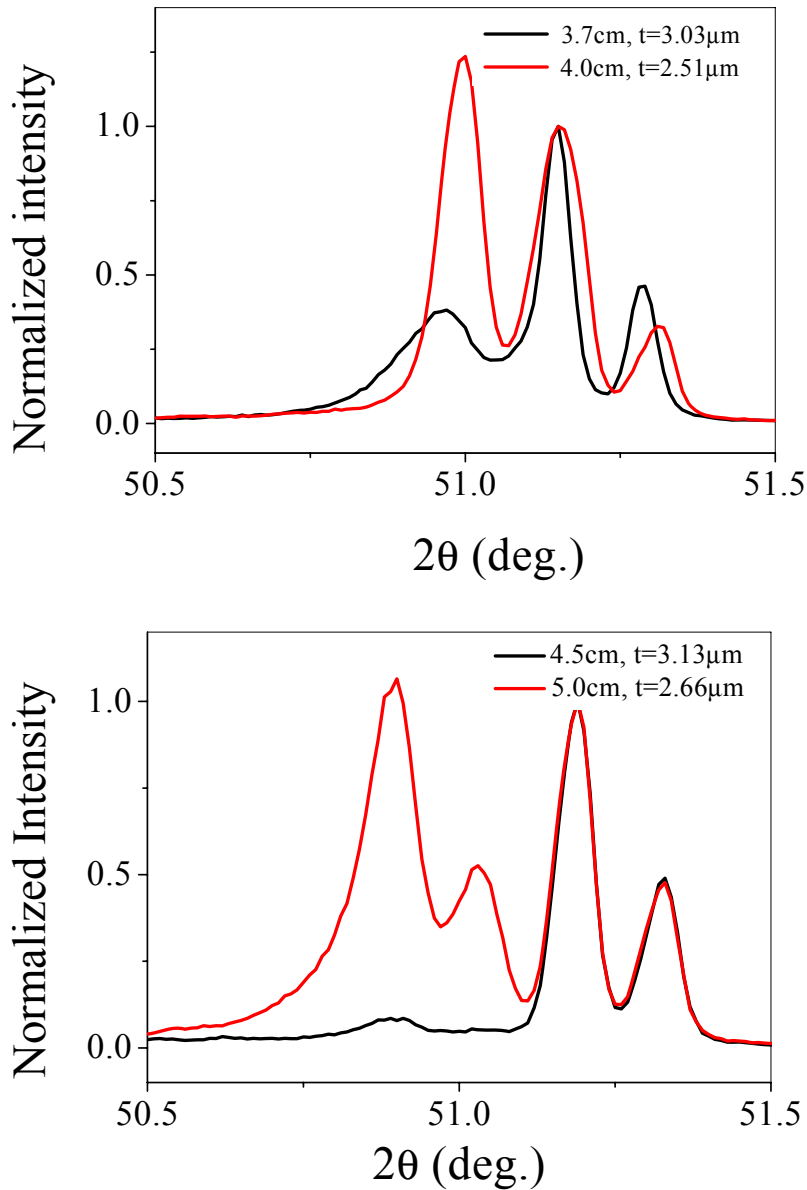

Figure 4.4 *(a) XRD patterns of $Bi_{0.8}Y_{2.2}Fe_4Ga_1O_{12}$ films sputtered from left side with substrate/target distance set at 3.7cm and 4.0cm and (b) $Bi_{0.8}Y_{2.2}Fe_{4.8}Ga_{0.2}O_{12}$ sputtered from right side with substrate/target distance set at 4.5cm and 5.0cm. The deposition rate decreases as the distance increases.*

except the sputtering pressure is kept at 50mTorr. We find that film intensity increase when the substrate/target distance is increased. However, the growth rate also decreases when target/substrate distance is increased.

4.2.1.4 Effect of oxygen partial pressure (Gas composition)

Some reports state that garnet films suffer from oxygen deficiency when the film is sputtered in pure argon [24]. However, we find that films sputtered in a mixture of 20sccm argon and 0.5sccm or higher flow rate of oxygen show no garnet phases (Fig.4.5). The sputtered films show a light reddish color and film surface is not smooth any more. Large particles and cracks are observed on the samples' surface.
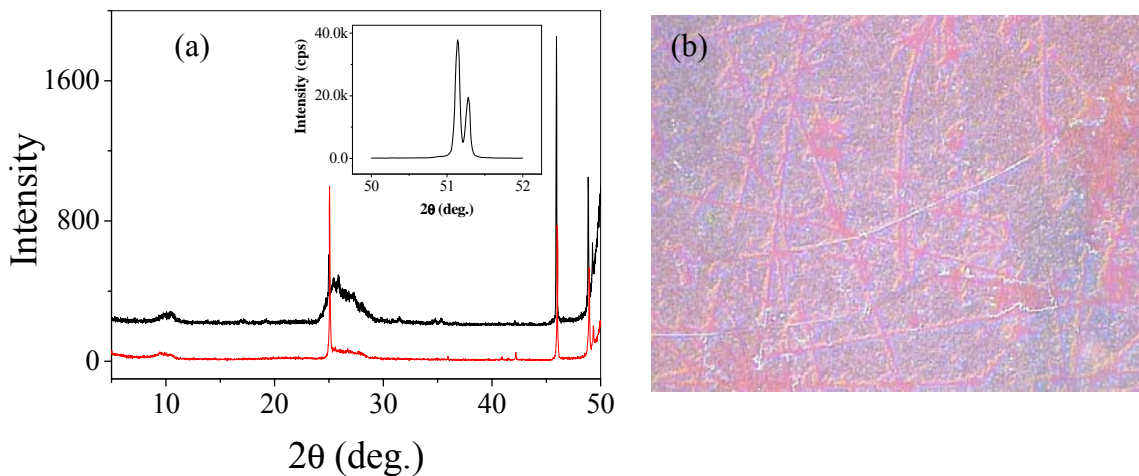
Figure 4.5 *(a) Flow of oxygen at 0.5sccm or higher diminish the garnet phase, as indicated by XRD analysis. (b)Surface image of the film sputtered with a mixture of oxygen*

4.2.1.5   Effect of RF sputtering power/DC self bias

HRXRD scans of $Bi_{0.7}Yb_{2.3}Fe_5O_{12}$ films sputtered on (111) GGG substrate under 50W (sample 1) and 100W (sample 2) are displayed in Fig.4.6. When film is less than 0.9µm thick, sample 1 shows only a single peak. Sample 2 shows an additional weak peak near the substrate and the main peak also shift towards the substrate as shown in Fig. 4.6a.

When film thickness exceeds 1μm, multiple peaks begin to develop. But the XRD patterns are different for the two samples. As shown in Fig.4.6b, sample 2 shows another peak at the left side of substrate. This is probably due to compositional variations within films and will be discussed in the next section. Our analysis show that film sputtered at 50W has a more uniform composition.
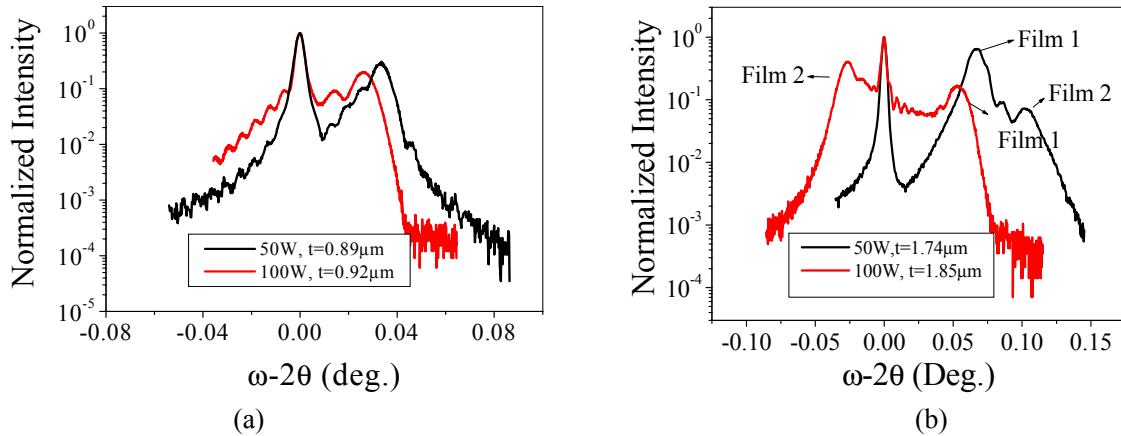

Figure 4.6 *ω-2θ scan of a film less than 1μm (a) and over 1μm (b). The red line shows film sputtered at 100W and the black line shows the film sputtered at 50W*

4.2.1.6 Discussion on effects of sputtering parameters on film structure

The above results are all related to and can be explained by the different energies of sputtered particles when they arrive on the substrate surface. In RF sputtering, argon ions are accelerated by target sheath and bombard the target surface thus result in the sputtering of target atoms (Fig. 4.7). The incident energy and flux of Ar^+ ions are determined by RF system design, working pressure, RF power applied on the target. These parameters, combined with material properties of target atoms, define the initial energy, flux and angular distribution of sputtered particles. The sputtered particles then travel through plasma from target to the substrate and suffer collisions and loose their energy upon collision. Therefore, the energies of sputtered particles when they arrived on the substrate surface are determined by substrate/target distance, chamber gas pressure

and composition of gas and initial energy of sputtered particles. Ar^+ ions also strike the substrate surface even the substrate sheath is much lower than target sheath.
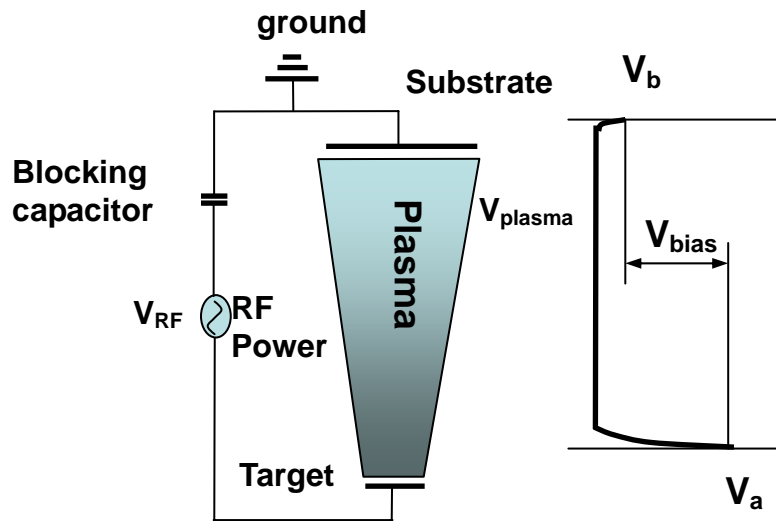

Figure 4.7 *Definition of sheath and bias in a diode sputtering system*

The initial energy of sputtered particles is known to be on the order of eV, corresponding to the temperature on the order of 10^4-10^5 K. After a finite number of collisions, the energy of sputtered particles is reduced to the thermal energy (k_BT) and the sputtered particles are said to be "thermalized". This thermalized distance is expressed as a product of the number of collisions and the mean free path of the sputtered particles. Thus the distance depends on (1) sputtering gas pressure (2) mass of sputtered particles and sputtering gas atoms (3) initial energy of sputtered particles (4) distance the sputtered particles traveled (substrate/target distance if assumed perpendicularly incident). For example, as the sputtering gas pressure increases, the thermalization distance of sputtered particles is decreased by an increase of collisions. The thermalization distance of sputtered particles was calculated by Westwood [98] using argon gas as the sputtering medium:

$$D = \frac{1}{2}\eta \cdot \lambda \cdot (1 + \cos\langle\theta\rangle) \tag{4-1}$$

λ is the mean free path of an atom with mass M_s travels through a gas consisting of atoms

of mass M_g and we assume an atom which is ejected at an angle $\frac{1}{2}\langle\theta\rangle$ to the normal

and it always makes an angle of $\frac{1}{2}\langle\theta\rangle$ to the target normal.

$$\lambda = \left[\sqrt{2}\pi N_s \sigma_s^2 + \frac{1}{4}\pi N_g (\sigma_s + \sigma_g)^2 (1 + \frac{M_s}{M_g})^{0.5} \right]^{-1} \tag{4-2}$$

Where N_s and N_g are the numbers per unit volume of sputtered and gas atoms and σ_s and

σ_g are the atomic diameters.

Ns<<Ng is satisfied even for very high deposition rate, thus the above equation can be

simplified as:

$$\lambda = \left[8.34 \cdot 10^{14} \cdot p \frac{(\sigma_s + \sigma_g)^2}{4}(1 + \frac{M_s}{M_g})^{0.5} \right]^{-1} \tag{4-3}$$

η in Eq.4-1 is the number of collisions after which the energy of sputtered atoms are

reduced to average energy E_g and can be calculated as:

$$\eta = \frac{\ln(\frac{E_0}{E_g})}{\ln(\frac{E_1}{E})} \tag{4-4}$$

E_0 is the initial energy of the sputtered atom. The majority of sputtered atoms have

energies below 10eV although some are with energies up to a few hundred eV, which is

comparable to the incident ion energy. E and E_1 stand for the energy before and after

collision. If we define $W = \ln(\frac{E_1}{E})$, W can be calculated from the integration of scattering

angle as:

$$W = 1 - \left[\frac{(1-M)^2}{2M}\right] \ln(\frac{1+M}{1-M}) \qquad \text{for } M<1 \qquad (4\text{-}5a)$$

$$W = 1 - \left[\frac{(M-1)^2}{2M}\right] \ln(\frac{M-1}{M+1}) \qquad \text{for } M>1 \qquad (4\text{-}5b)$$

Where $M = \dfrac{M_g}{M_s}$. Using the values listed in Table4.3, the thermalized distances for Bi,

Y, Yb and Fe at 10mTorr, 25mTorr ad 50mTorr are calculated.

Table 4.3 Calculated thermallization distances at 10, 25 and 50mTorr. The atomic diameters are adopted from http://science-park.info/periodic/

	Ar	Bi	Y	Yb	Fe	Ga
Atomic diameter (nm)	0.36	0.31	0.36	0.39	0.25	0.24
Atomic mass	40	209	89	173	56	70
D @10mTorr (cm)		3.5-5.7	2.1-3.4	2.5-4.1	2.5-4.1	2.8-4.5
D @ 25mTorr (cm)		1.4-2.3	0.84-1.4	1.0-1.66	1-1.7	1.1-1.8
D @ 50mTorr (cm)		0.7-1.1	0.42-0.68	0.51-0.83	0.5-0.8	0.6-0.9

It is clearly shown in Table 4.3 that the thermalization distances for these elements are

around 2cm to 5cm under 10mTorr bleeding pressure. Since the target/substrate distance

were changed from 3.7cm to 4cm for left side target (stronger magnetic field thus lower

DC bias) and 4.0cm to 5.0 cm for right side target (weaker magnetic field strength thus

higher DC bias), respectively, we could not guarantee that most of the sputtered particles

lose their initial energy before reaching the substrate. On the other hand, the thermalized

distance is less than 1cm under 50mTorr sputtering pressure thus most of the sputtered

particles lose their initial energy and reach to the thermalized states. As reported, the

garnet structure is more sensitive to the energetic particles bombardment. A small

negative bias (-15V) applied on the substrate dramatically altered the properties of the

bismuth doped gadolinium iron garnet films has been found [21]. Thus we could expect the peak intensity drop for lower pressure sputtering. When the sputtered particles deposited on the substrate with higher energy, a more dense structure with smaller lattice parameter should be expected due to the higher energy particles bombardment. This can be seen from the 2θ shift to higher angle in Fig.4.2. Effect of sputtering pressure on lattice parameters change was also observed in $BaTiO_3$ films but the opposite trend was found: larger lattice parameter associate with low pressure sputtering [99]. This phenomenon maybe explained by the different material properties of these two materials. In addition to the bombardment effect, compositional change due to different sputtering pressures has also been found and it also causes the lattice parameters to change. This will be discussed in the next section.

When the sputtered particles arrive and condense on the substrate, they vibrate with certain thermal vibration energy. However, if the thermal vibration is too intense, for example, due to high substrate temperature, it is difficult to form a crystalline structure and thus result in an amorphorous structure.

Westwood [98] and Somekh [100] also reported that the energy of sputtered particles is related to the mass of the sputtered atoms. They concluded that the energy loss of the sputtered particles increase with increase of the mass of sputtering gas atom. Since oxygen is lighter than Ar, we could expect that the sputtered particles have lower energy and shorter thermalization distance if sputtered in pure Ar.

In conclusion, lower pressure, shorter substrate/target distance, higher substrate temperature and mixture of oxygen, all the parameter will increase the sputtered particles energy when they arrive on the substrate surface. If most of the sputtered particles can not

be thermalized, the outcome is a poor crystalline quality film.

Based on our results, the optimized parameters are listed in table 4.4.

Table 4.4 Optimized sputtering parameter

Sputtering parameters	Experimental conditions	
	Left side	Right side
Working pressure (mTorr)	50	50
Sputtering gas	Ar	Ar
Substrate temperature (Ts) (^{o}C)	550-620	550-620
Substrate/target distance (cm)	4.0 for Bi-YIG 3.7 for Bi-YbIG	5.0 for Bi-YIG

4.2.2 Structural properties of sputtered films

The film thickness depends linearly on sputtering time (Fig.4.8). This is critically important for linear birefringence control, as will be discussed in chapter 5 since film thickness can be controlled precisely. Single layer thin films deposited on (111) single crystal GGG substrates, both in tensile ($Bi_{0.7}Yb_{2.3}Fe_5O_{12}$) and compressive ($Bi_{0.8}Y_{2.2}Fe_5O_{12}$, $Bi_{0.8}Y_{2.2}Fe_{4.8}Ga_{0.2}O_{12}$ and $Bi_{0.8}Y_{2.2}Fe_4Ga_1O_{12}$) stress, do not crack with thickness up to 4 μm.
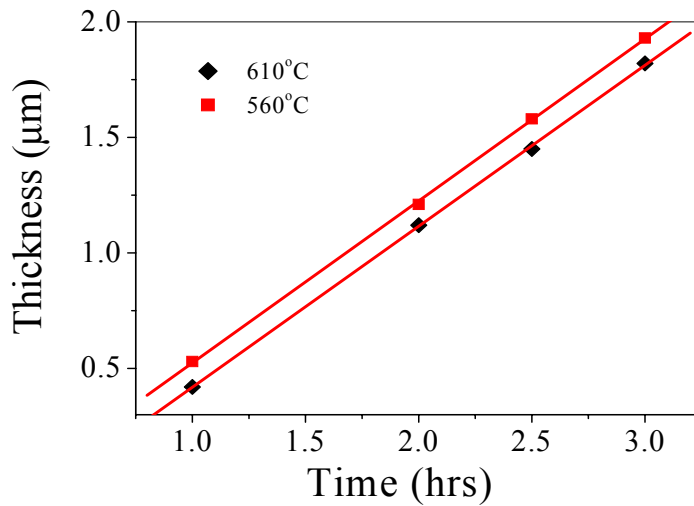
Figure 4.8 *Linear dependence of film thickness on sputtering time.*

HRXRD analyses show that the film lattice deformations are thickness dependent. Deposited Bi-YIG films show only a single XRD peak and very high crystalline quality when films are thin (i.e., a few hundred nm). The films show very narrow FWHM (0.003^o for substrate and 0.016^o for film) and very nice fringes. However, films tend to segregate into dual layer structure when they are grown thicker than 1μm (Fig. 4.9).
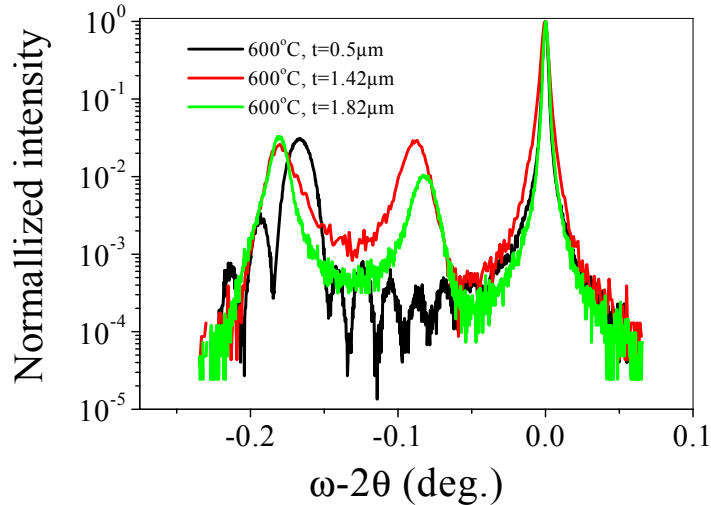

Figure 4.9 *HRXRD patterns of Bi-YIG films. Dual layer films begin to develop when film is grown thicker than about 1μm.*

More interesting is the sputtering of $Bi_{0.7}Yb_{2.3}Fe_5O_{12}$ film, which has a smaller relaxed lattice parameter (a_R=12.3774Å) and is in tension if deposited on (111) GGG (a_R=12.383Å) substrate. All the films deposited at RF sputtering power of 50W, no matter how thick show peak or peaks at 2θ angle higher than the substrate's. In other words, both upper and lower layers are in tension. Films sputtered at 100W, if thinner than 1μm, show single layer film in tension. If the film is grown thicker, however, upper layer tends to develop in compression (2θ angle lower than that of substrate), as shown in Fig.4.10. Eventually, two layers of film, one in tension and another in compression are formed. All the films sputtered at 100W, if thicker than 1.5μm, show similar results. Films with thickness in between 1μm to 1.5μm show an indistinct peak between substrate and lower

layer. Notice that the intensities between peaks are very high compared to samples sputtered at 50W. We believe this is due to a gradual compositional gradient across film thickness.
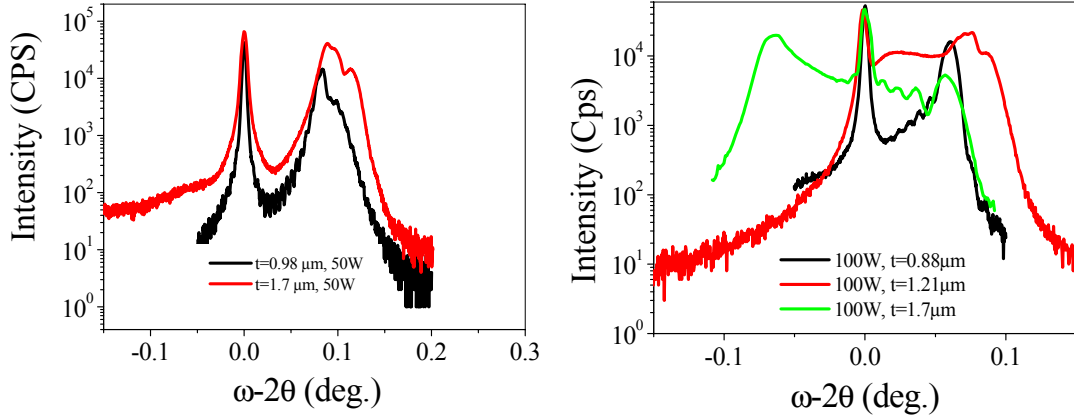

Figure 4.10 *HRXRD scan of films sputtered at 50W and 100 W. When films are grown thicker, both upper and lower layers are in tension if sputtered at 50W. However, films sputtered at 100W display lower layers in tension and upper layers in compression.*

The formation mechanism of dual layer structure has been discussed in Ce-YIG system [94, 95]. A strain gradient across film thickness is proposed to account for this phenomenon. Misfit dislocations are formed within the body of the film, which has uniform composition throughout, to accommodate the strain.

Heteroepitaxial growth of semiconductor thin films have been extensively studied [101-109] and well developed. A heteroepitaxial film will remain pseudomorphologically strained to the substrate provided that the strain energy/area due to the lattice constant mismatch between the substrate and the film does not exceed the energy required to form interfacial misfit dislocations at the film/substrate interface. The increase of this strain energy with film thickness for a given mismatch leads to the familiar concept of critical film thickness, h_C, [101] below which the film will remain pseudomorphologically strained and above which a misfit dislocation array at the substrate/film interface will

cause the film to lose registry with the atomic lattice of the substrate. Typically one would assume that if the film is grown beyond its critical thickness that the misfit dislocation array would occur in close proximity to the film/substrate interface and that the entire film would relax as a whole rather than partially relaxed and partially strained. Both the composition and strain state of a Bi- or Ce- substituted rare earth garnet film can be determined through measurement of the film lattice constants perpendicular to ($a_\perp$) and parallel to ($a_{//}$) the film/substrate interface. Bulk $Bi_xY_{3-x}Fe_5O_{12}$ is cubic with the relationship between lattice constant and Bi concentration "x" given through Vergard's law as: $a_R=12.376+0.083x$ Å [40]. Biaxial strain will distort the cubic lattice of a heteroepitaxially grown film due to lattice mismatch with the substrate if the film remains pseudomorpholorgically strained or, alternatively, thermal expansion mismatch with the substrate if the film does not maintain atomic registry with the substrate at growth temperature. In either case, the bulk or relaxed cubic lattice constant of a biaxially strained film is related to $a_\perp$ and $a_{//}$, assuming isotropic elasticity theory, by the relationship

$$a_R = a_\perp \frac{1-\nu}{1+\nu} + a_{//} \frac{2\nu}{1+\nu}$$
(4-6)

where ν is Poisson's ratio.   The biaxial strain in the film due to lattice constant mismatch or thermal expansion mismatch is then $(a_{//}- a_R)/ a_R$, defined in a positive sense for tensile strain.

The calculated perpendicular, parallel and relaxed lattice constants are listed in Table 4.5 (see Fig.4.11 for definition of film 1 and film2), assuming a Poisson's ratio of 0.29 for Bi-YIG films (the same as YIG) and an undeformed substrate. It is clearly shown that the $a_{//}$ of lower layer is very close to a_s (12.383Å) and the film is in compression. The upper

layer shows a more relaxed state. The $a_{//}$ is close to $a_{\perp}$ and show a almost cubic structure.

Even the calculated biaxial strain show that the upper layer is in tension, it falls within

the calculated uncertainty. The relaxed lattice parameters a_R calculated based on Eq.4-6

for lower layer and upper layer clearly shows the difference, which indicates the

compositional change between the two layers. Mino [94] also observed the different

relaxed lattice parameters for upper and lower layers For the Ce-YIG system. They

ascribed this difference to the poor quality of upper layer. However, this is not true in our

results. Both upper and lower layers show very strong and clear peaks as shown in

Fig.4.9. Thus the change in relaxed lattice parameter corresponds to a compositional

change.

*Table 4.5 Measured perpendicular, parallel and calculated relaxed lattice parameters for
the dual layer films*

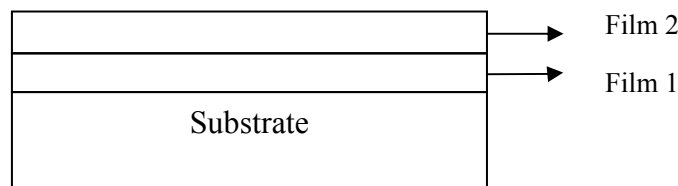|	$a_{\perp}$	$a_{//}$	a_R	$\varepsilon_{//}$
$T_s=560^oC$, t=1.58µm				
Film1	12.469	12.378	12.428	-0.40%
	±0.002	±0.018	±0.009	±0.17%
Film2	12.435	12.462	12.447	0.12%
	±0.001	±0.011	±0.006	±0.10%
$T_s=560^oC$, t=1.21µm				
	$a_{\perp}$	$a_{//}$	a_R	$\varepsilon_{//}$
Film1	12.462	12.389	12.429	-0.32%
	±0.001	±0.007	±0.004	±0.06%
Film2	12.431	12.457	12.442	0.12%
	±0.001	±0.011	±0.006	±0.10%
$T_s=610^oC$, t=1.82µm				
	$a_{\perp}$	$a_{//}$	a_R	$\varepsilon_{//}$
Film 1	12.465	12.385	12.429	-0.35%
	±0.001	±0.005	±0.003	±0.04%
Film 2	12.420	12.468	12.441	0.21%
	±0.001	±0.005	±0.003	±0.04%

Figure 4.11 *Definition of the dual layer films. Lower layer film is defined as film 1 while upper layer is defined as film 2.*

Measurements of film composition by RBS provide additional evidence that compositionally varied layers develop in RF sputtered garnet films. For the 1.8μm sample shown in Fig. 4.9, RBS, however, gives no compositional variation across film thickness (Fig.4.12a). This is because RBS lose resolution when film is thick. We sidestep the inaccuracies in the RBS analysis of thick (μm size) films by examining films sputter-deposited only 1h (~0.6μm).

Fig.4.12b shows the compositional profiles of the thin sample, sputtered under 80W and 50mTorr of Ar. Notice that the gallium content tends to increase with depth, as we probe closer to the GGG substrate, possibly indicating gallium diffusion from the substrate into the film. Bismuth content is lower than the stoichiometry of target and it decreases towards GGG substrate. The XPS with sputtering measurement also verify the bismuth segregation near film surface, as shown in Fig.4.13a. Bismuth has a lower surface binding energy and liable to be preferentially sputtered [16, 17, 20, 21], as shown in Fig.4.13b. Surface segregation of bismuth was also observed in ref [20]. Iron content is also found to be lower than the stoichiometry of the target but does not vary with thickness. The iron deficiency seems like a common problem for sputtering as reported by several authors [16, 28, 30, 32, 34].
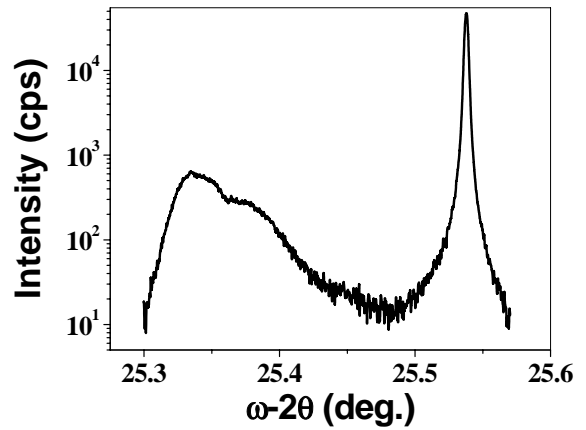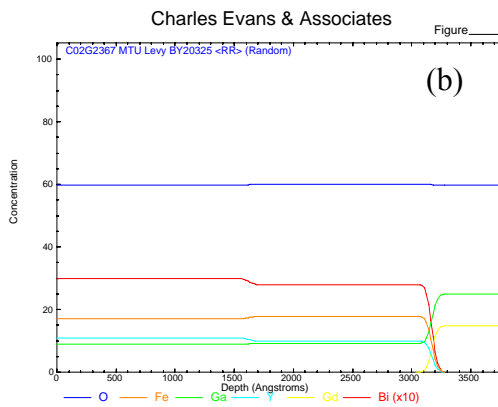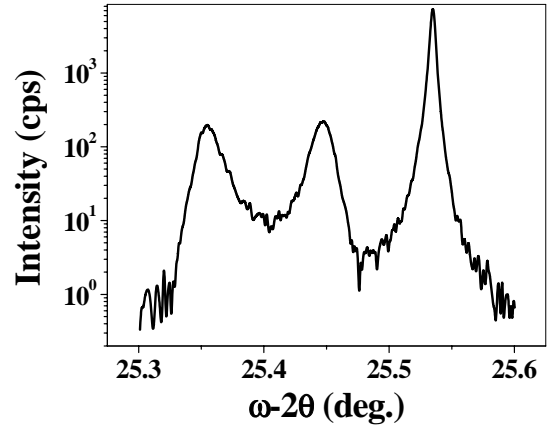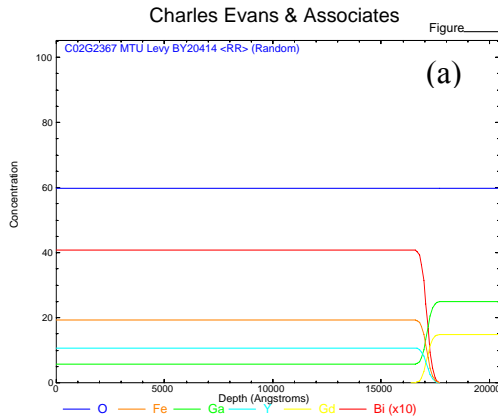
Figure 4.12 *RBS results for sputtered Bi-YIG films. The thin sample shows compositional variations across film thickness while the thicker one does not. This is because the RBS lose resolution as the probe depth is increased.*
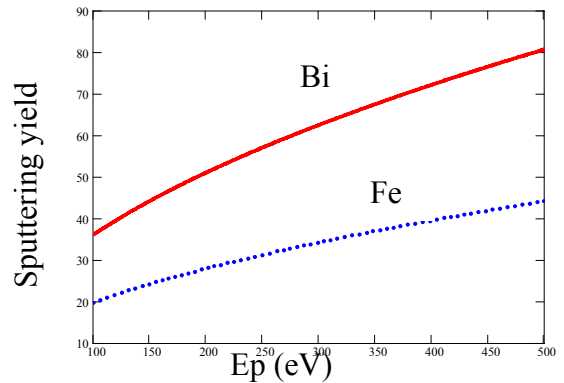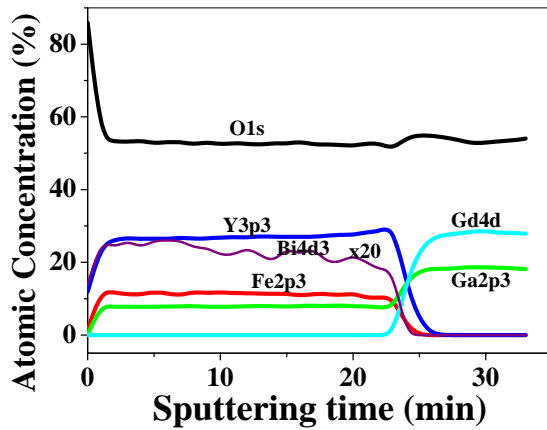

Figure 4.13 *(a) XPS also verify the bismuth segregates near film surface. (b) Sputtering yield of Bi and Fe calculated from Ref.20*

Based on our measurements, however, we can not completely rule out the possibility of strain gradient contribution to the formation of dual layer structure or the combined effect of compositional variation and strain gradient on the dual layer formation. Further studies, such as TEM cross section observations and XPS surface composition analysis combined wet etching should be employed to clarify this issue.

The development of dual layer structure if film is grown thicker can not be suppressed so far. However, we found that lower sputtering power/dc bias (Fig.4.6a), higher substrate temperature (Fig.4.14) is helpful to delay the appearance of 2nd peak, due to more uniform composition across film thickness.
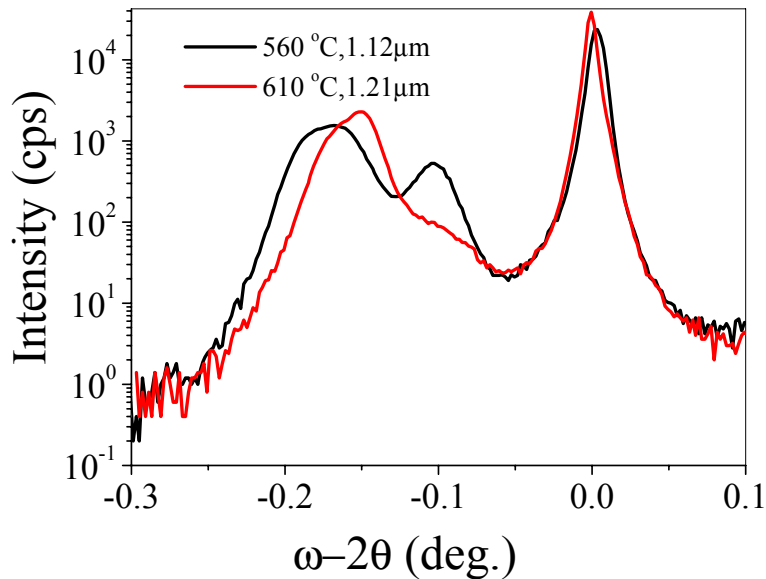

Figure 4.14 *Two films of similar thickness sputtered at $560^{o}C$ and $610^{o}C$. The higher deposition temperature delays the appearance of the 2nd peak.*

4.3 Compositional controls of sputtered films

4.3.1 Control by sputtering pressure

We find that sputtering chamber pressure has a significant effect on optical properties and compositions of deposited films. The index of refraction is found to increase with

decrease of pressure (Fig.4.15a). It can be advantageous for fabrication of double layer structure since the index contrast of the two layers can be controlled. XRD show the film peak shift toward higher 2θ when pressure is lowered (Fig.4.15b).
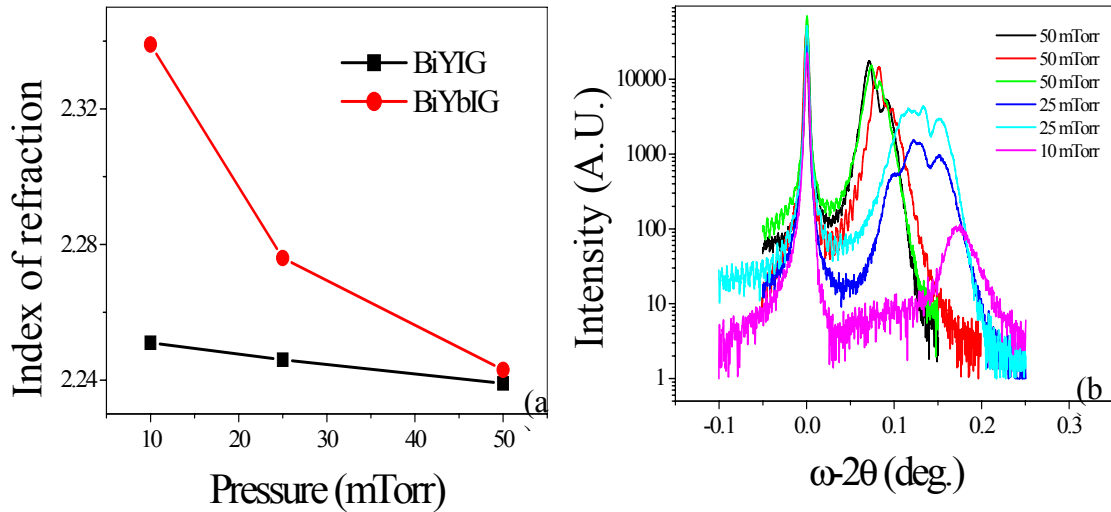

Figure 4.15 *(a) Effect of bleeding pressure on index and (b) XRD scans of the films deposited under 50, 25 and 10mTorr pressure of Ar for Bi-YbIG. The refractive indices are found to decrease with increase of sputtering pressure. XRD peak intensities decrease and shift to higher 2θ as bleeding pressures are decreased.*

The above results can be partially ascribed to the change of film composition and verified by the microprobe analysis. As the total chamber pressure is increased, we find that the bismuth and iron contents decrease while the yttrium or ytterbium contents increase (Fig.4.16). As discussed earlier, bismuth suffers from preferential sputtering due to low surface binding energy. At lower chamber pressure, the preferential sputtering becomes more prominent. Thus it results in decreased bismuth content in the sputtered films. The correlation between iron and yttrium or ytterbium can be ascribed to the antisite defect, which means the Fe and Y or Yb atoms change their occupied sites:
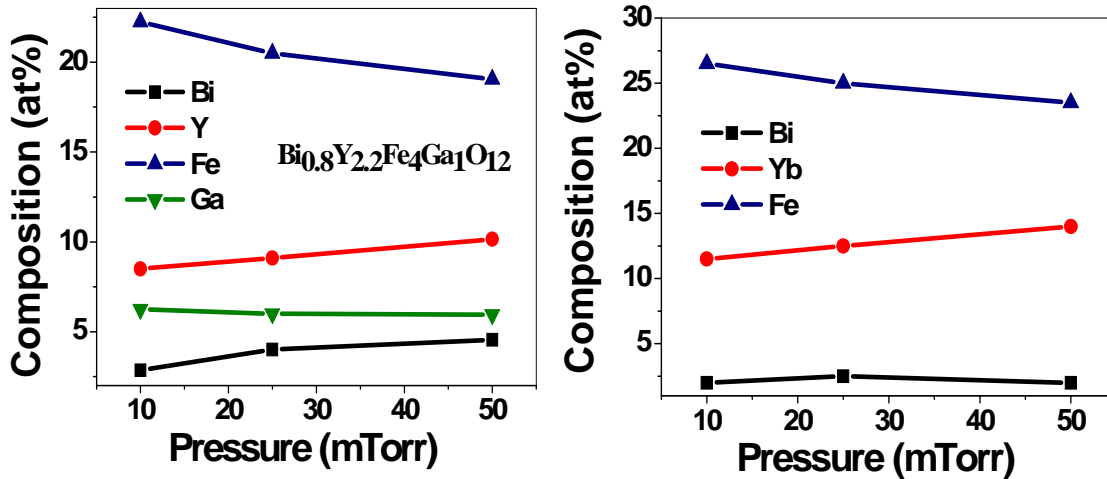
$$Y_Y + Fe_{(a)} \rightarrow Y_{(a)} + Fe_Y \qquad (4\text{-}7)$$

Figure 4.16 *Effect of sputtering pressure on the atomic composition of Bi, Y, Yb, Fe and Ga content*

The formation energy of this type of defect has been calculated by computer simulation [139] and found to be around 0.8eV. While the formation energy of Schottky and Frenkel disorders are between 3-8eV, it is reasonable to assume that our sputter deposited films has the antisite defects and these defects result in the change of Fe and Y composition. A cation ratio for $(Bi_xY_y)(Fe_zGa_t)O_{12}$ can be defined as $(x+y)/(z+t)$ and plotted in Fig.4.17 for films sputtered at 10, 25 and 50mTorr. The stoichiometric ratio of 0.6 is also plotted for comparison. We find that the ratio of $(Bi+Y(Yb))/(Fe+Ga)$ increases with pressure. Close to stoichiometric composition for Bi-YIG and Bi-YbIG is achieved under 25mTorr and 50mTorr chamber pressure, respectively. The optimized pressure difference is caused not only by the target itself but also by different magnetic filed strengths applied on the target during sputtering (magnetic field strength associates with DC self bias in RF magnetron sputtering).

The relationship between total gas pressure and film composition is complex, as the sputtering pressure influences the relative sputtering yield of different species, their angular distribution, the scattering probabilities by the gas ions and resputtering. In

particular, different angular distribution of individual flux impinging on the substrate has been proposed by Im [110] for BST thin films. The different elements have their different pressure dependent angular scattering distribution in the gas phase due to their different masses. Consequently result in a pressure dependent composition profile.
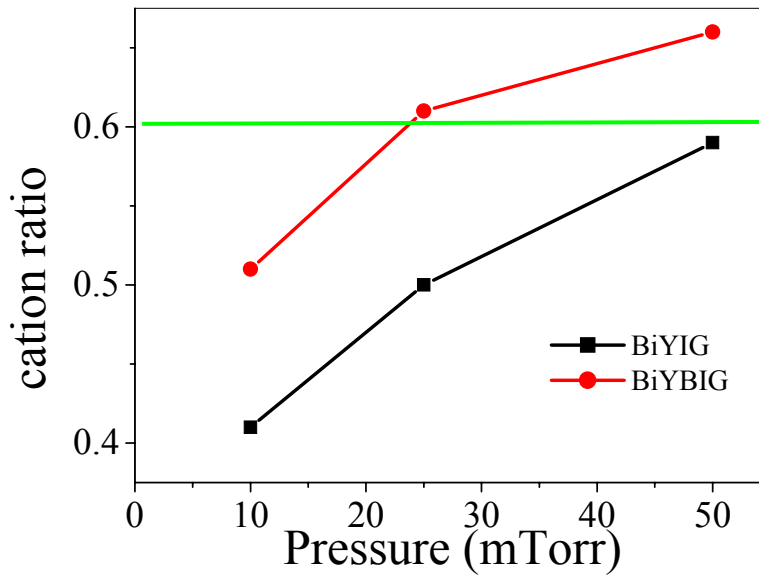

Figure 4.17 *Dependence of cation ratio (Bi+Y (Yb))/(Fe+Ga) on pressure. The ideal stoichiometry is also shown. This ratio is found to increase as sputtering pressure is increased.*

4.3.2 Control by dc bias

Composition changes due to dc bias of superconducting film [111] and BST film [112] have been reported. Furuya and co-workers have discussed the effect of the DC self bias in Bi-substituted dysprosium iron garnet films under RF magnetron sputtering conditions and shown that film composition can be controlled by adjusting the bias voltage through the cathode's magnetic field [21]. They find that low bias (20V) yields a stable composition regardless of sputtering time, surmising that compositional change is prevented because at these low energies the target compound is sputtered mostly in clusters. Our results are consistent with a bias-dependent compositional change. Since

both power and DC self bias of our sputtering system can not be adjusted simultaneously, we tune sputtering power only. There is a corresponding reduction in bias voltage variations during the deposition process. [for Bi-YIG at 100W, bias changes about 8 V at bias levels of ~ -170 V. For Bi-YbIG at 50 W, bias changes only ~ 4V, at bias levels of ~ -100V]. The DC bias is also found to change with the condition of the target, i.e., decreases after long time of target usage.

The compositions of the two films sputtered at 50W (sample 1) and 100W (sample 2), which are displayed in Fig.4.6b were measured by RBS and EPMA. Results from RBS, however, show no compositional change as a function of film thickness within the detection precision for these two samples. Microprobe analysis results, which give an average composition within the pear shape interaction volume, show no compositional difference, either. We believe the discrepancy is caused by the limitations of the measurement techniques used here as RBS lose resolution when film is thicker.

Triple crystal high resolution X-ray diffraction was then used to obtain the lattice parameters of these two samples. The results are listed in Table4.6. Change of relaxed lattice parameter clearly indicates the compositional change across film thickness for both of the two samples. However, film sputtered at 50W shows a more uniformed compositional profile.

Table 4.6 Lattice parameter calculated from HRXRD for sample 1 and 2

	Sample 1		Sample 2	
	Film 1	Film 2	Film 1	Film2
Sputter power (DC bias)	50W (-120V)		100W (-175V)	
Film Thickness (μm)	1.74		1.85	
$a_\perp$ (Å)	12.3516	12.3436	12.3950	12.3593
$a_{//}$ (Å)	12.3855	12.3674	12.3822	12.3842
a_R (Å)	12.3669	12.3543	12.3893	12.3705

4.4 Morphological and magnetic properties of sputtered films

A granular structure with grain size of several tenths nm can be clearly observed by AFM. The grain size depends on film thickness. Deposited thin films have very smooth surface
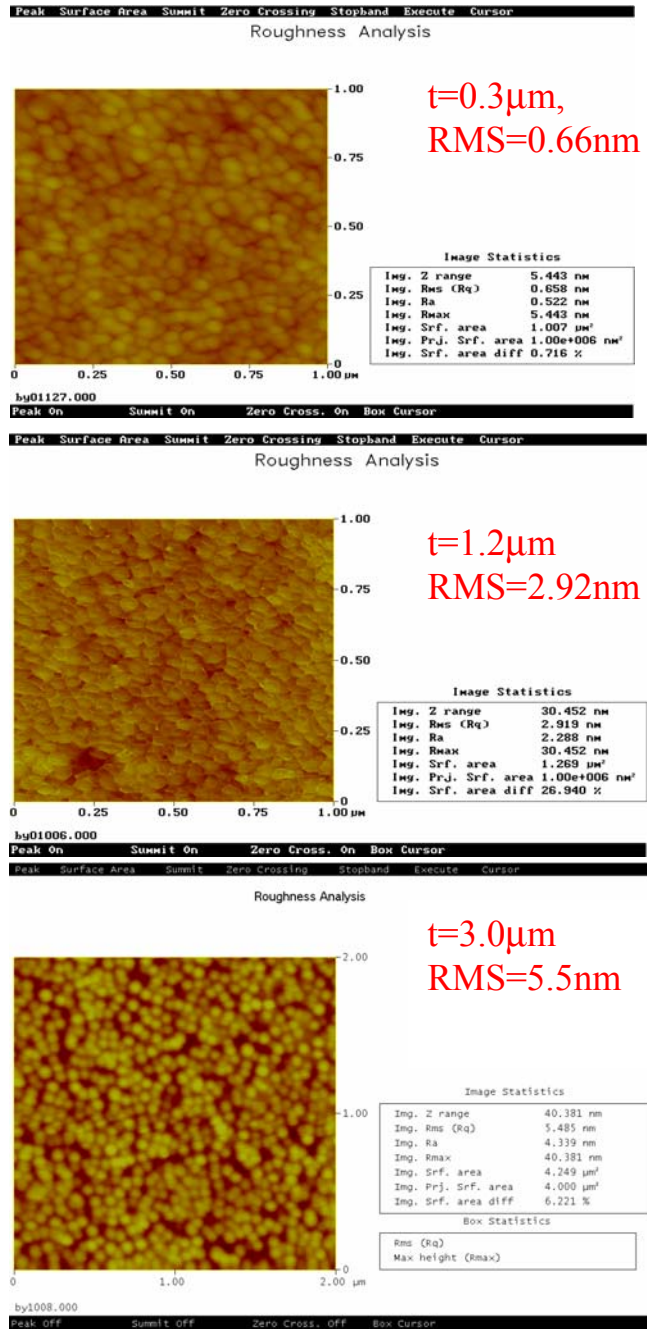

Figure 4.18 *AFM roughness analysis shows that the film RMS roughness increase as film thickness is increased.*

with RMS roughness lower than 6nm for all the samples with thickness up to 4μm. However, we have found that surface roughness increases with film thickness, i.e., RMS roughness increases from 0.66nm for a 0.3μm film to 5.5nm for a 3.0μm thick film. This is in contrast with results from PLD deposition [92], in which roughness is almost constant regardless of film thickness.

All the films deposited on GGG substrate exhibit in plane magnetization with coercive fields in the range of 8-20Oe. This is advantageous for in-plane faraday rotator device fabrication because the magnetization should be collinear with the beam propagation direction. Fig. 4.19 shows the GGG-subtracted hysteresis loops. In plane magnetization exhibits a much square shape with lower coecivity and higher saturation magnetization M_S. No noticeable magnetic anisotropy is detected in the plane of any of the films.
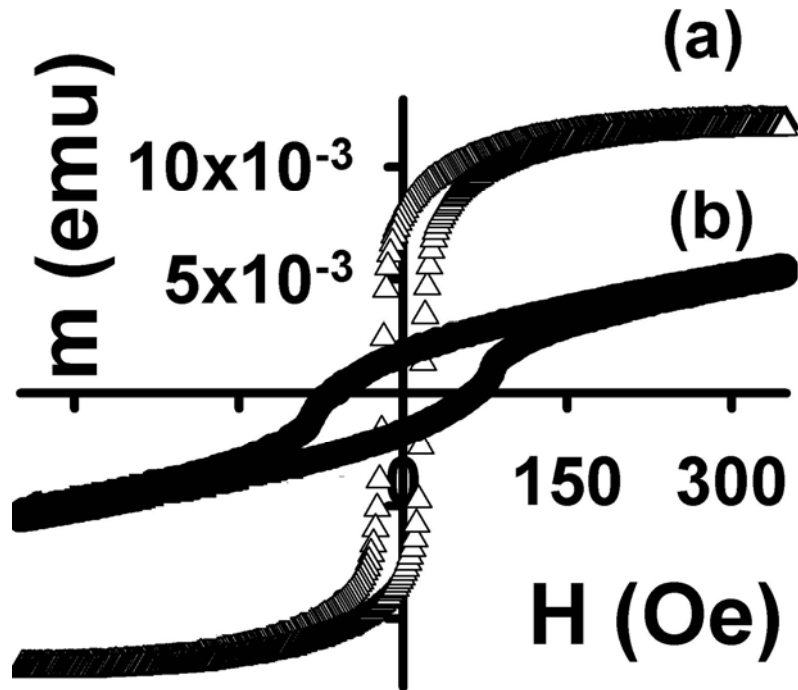

Figure 4.19 *RF sputtered films deposited on (111) GGG substrates are in plane magnetized. The out of plane magnetization shows a larger coercivity and lower saturation magnetization.*

4.5 Optical and magnetooptical characterization

4.5.1 Propagation loss reduction

Propagation loss should be kept as small as possible to increase the signal to noise ratio for an optical isolator. In addition to the scattering loss, sputtered films may suffer another loss due to the presence of Fe^{2+} ions. Unlike the LPE films where Fe^{2+} or Fe^{4+} is the result of charge compensation due to impurities, Fe^{2+} in sputtered film is the result of oxygen vacancies, as shown below:

$$2Fe^{3+} + O^{2-} \Leftrightarrow 2Fe^{2+} + \frac{1}{2}O_2 + V_o \qquad (4\text{-}8)$$
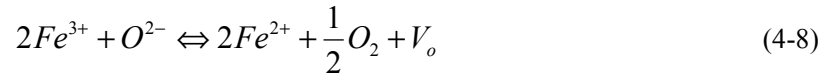
Where V_o stands for oxygen vacancy. The charge transfer from Fe^{3+} to Fe^{2+} can increase the absorption coefficient up to a factor of 100 [77].

Oxygen content was measured by RBS and XPS with sputtering technique for our sputter deposited films. We find that there is a certain degree of oxygen deficiency within the film (atomic concentration<60%) from RBS measurement (Fig.4.20a). The compositions in Fig. 4.20a were measured directly by RBS and the oxygen content was fit by using grazing angle spectra. Results from XPS also verify the oxygen deficiency (Fig. 4.20b). The Fe2p3 binding energies are centered at 708eV and 722eV for $Fe2p_{3/2}$ and $Fe2p_{1/2}$, respectively, which are correspond to energies reported for Fe_2O_3. We also observe shoulder peaks occurring at a slight lower binding energy from the $Fe2p_{3/2}$ and $Fe2p_{1/2}$ peaks. Other elements do not show this shoulder peak. Considering the FeO reference energy is 1.5eV lower than that of Fe_2O_3, this shoulder peak indicates the Fe in the film partially transforms from trivalent to bivalent form. This shoulder peak is not noticeable a few monolayer below sample surface but pronounced within film. This is because oxidations of Fe^{2+} to Fe^{3+} near the sample surface when film is exposed in air.

Figure _____
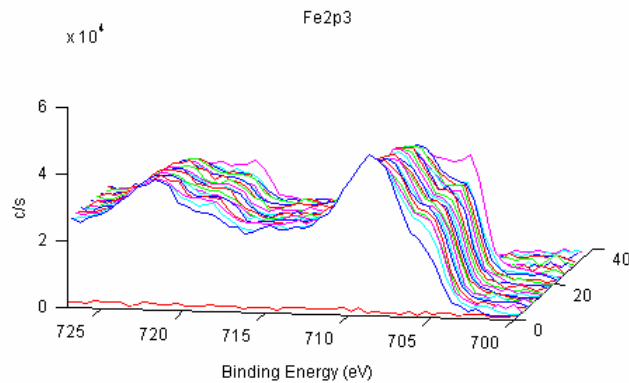
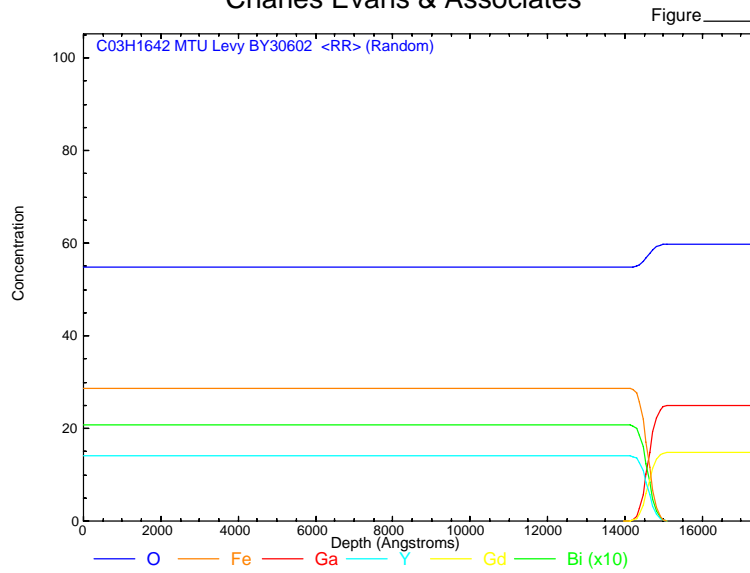C03H1642 MTU Levy BY30602 <RR> (Random)

Figure 4.20 *RBS (a) and XPS (b) show oxygen deficiency in the sputtered garnet films. Fig.4.20b also indicates that Fe^{3+} partially convert to Fe^{2+} due to the oxygen vacancies, as seen from the shoulder peaks of Fe2p3 binding energy.*

To reduce the oxygen vacancies and absorption coefficient, one would prefer to sputter in

an oxygen containing environment.   However, our result shows that crystalline structure

is suppressed when the oxygen flow rate is higher than 0.5sccm. Since at the moment we

do not have the capability to control flow rate lower than that, the reduction of absorption

is studied by post annealing in an oxygen environment.

The propagation loss was characterized by the cut back method since it folds out the coupling loss and gives only absorption and scattering loss. This method involves measuring and comparing the transmittances of waveguide having different length by cutting a waveguide to change the length. Propagation loss in dB/cm can be obtained by plotting $\log(I_{out}/I_{in})$ vs. waveguide length. The only drawback of this method is high quality facet should be prepared.
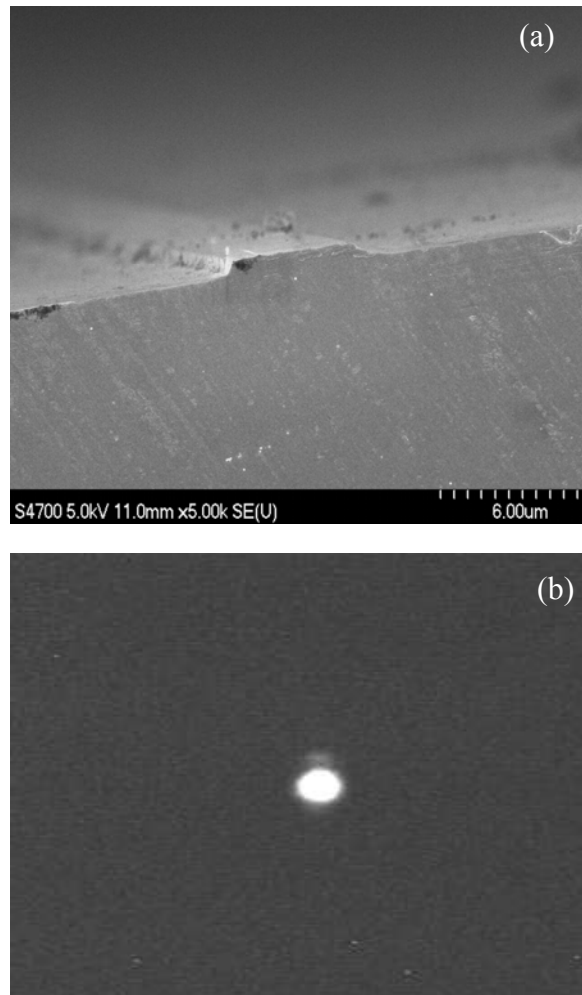

Figure 4.21 *(a) SEM image of a 4μm wide, 600nm deep ridge waveguide (b) Laser beam is well confined in the waveguide, as seen from the output beam shape.*

Ridge waveguides (Fig.4.21a) were fabricated by standard photolithography and plasma etching techniques (see appendix for fabrication procedure). The widths of waveguide range from 2μm to 10μm, while the depth of waveguide is about 600nm. Light through a 1.55μm laser diode is end-butt coupled into the waveguide. The light is well confined in the waveguide, as shown in Fig.4.21b.

Annealing was carried out in a tube furnace hold at 400^oC, 520^oC, 650^oC and 750^oC under the flow of oxygen for 3hrs at each temperature. The film shows no change when annealed below 650^oC, as determined from XRD and AFM analysis. When annealing temperature is increased to $750\,^oC$, film peaks begin to shift to higher 2θ angle (Fig. 4.22). A plausible explanation is the diffusion of gallium atoms from the substrate into the film. Surface roughness also increases with annealing temperature (Fig.4.23). It becomes inhomogeneous and rougher when annealed at 750^oC.
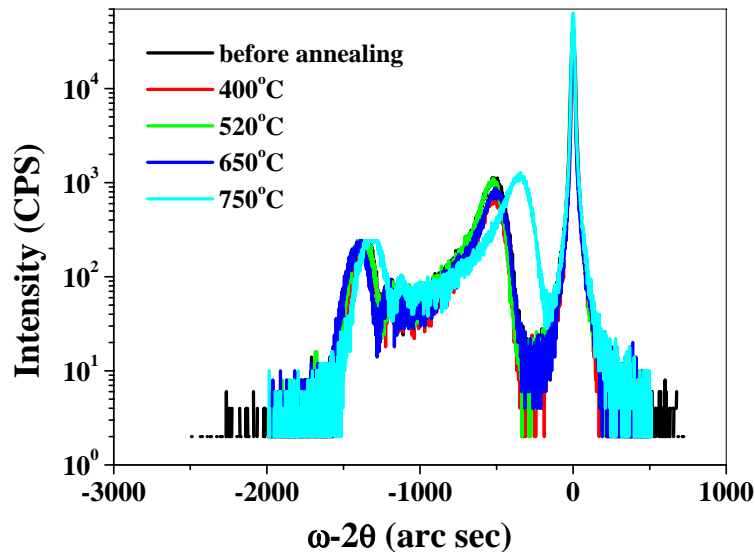

Figure 4.22 *HRXRD patterns of $Bi_{0.8}Y_{2.2}Fe_{4.8}Ga_{0.2}O_{12}$ films before and after annealing in an oxygen atmosphere at $400\,^oC$, $520\,^oC$, $650\,^oC$ and $750\,^oC$. Film peaks start to shift to higher 2θ at $750\,^oC$.*

Before annealing **500°C annealing**

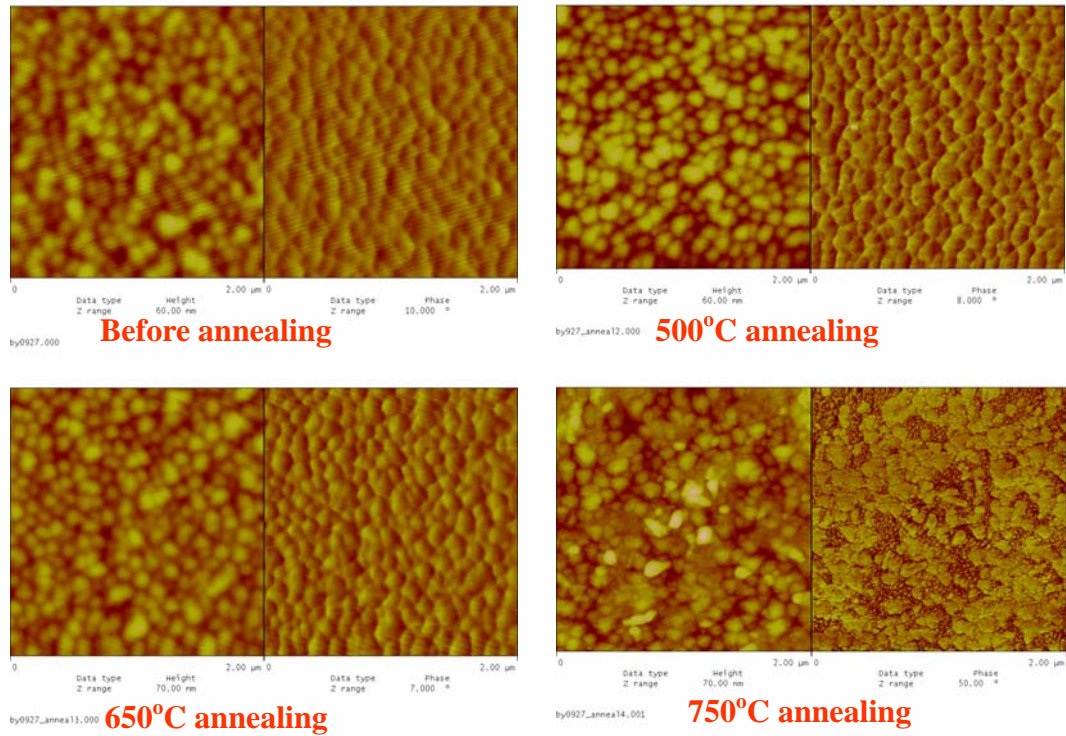**650°C annealing** **750°C annealing**

Figure 4.23 *AFM measurement of surface morphology before and after annealing. Surface roughness increase upon annealing.*

Based on the above results, we choose 500°C and find the oxidation process has already started at this temperature. As shown in Fig.4.24, the propagation loss is reduced to 10 ± 5dB/cm from 25 ± 5dB/cm before annealing. This loss can be further reduced by treatment of waveguide in a H_3PO_4 held at about 120°C [113]. This is because the sidewall damage by plasma etching can be reduced by phosphoric acid etching.
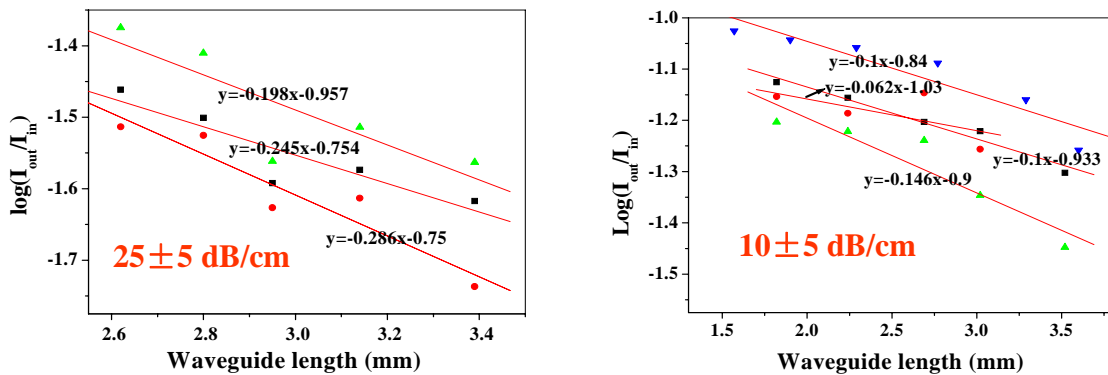

Figure 4.24 *Loss measured by cut-back method before annealing (a) and after 500°C, 3hrs annealing in oxygen environment (b)*

4.5.2 Magnetooptical properties of sputtered films

The Faraday rotation of our sputtered film is shown in Fig.4.25 where the incident beam is normal to the film surface. The maximum FR, θ_F=6.5 ^{o}/µm occurs at λ=430nm. The FR at near infrared region, which is more practical for MO devices, however, can not be determined since the result may fall into the detection limit of this method due to very thin film thickness. Thus we use optical fiber coupling through a waveguide to measure the FR (see chapter 3 for characterization technique) at λ=1.55µm. Instead of reversing

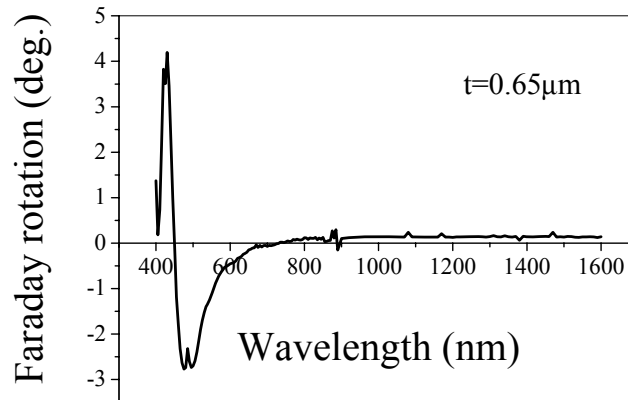
Figure 4.25 *Faraday rotation of a 0.65µm thick film measured by perpendicular incidence.*

the beam propagation direction, magnetic filed is reversed. Fig.4.26 shows the measured intensity profile after switching the direction of magnetic filed. 10 degree FR is obtained when apply magnetic field in one direction and -12 degree obtained when magnetic field is reversed for a 3mm long waveguide. Notice the minimum output intensity is changed when the magnetic filed is reversed. This is due to the combined effects of Faraday rotation and linear birefringence. The result of competition between these two effects is the elliptical polarization output. When magnetic field is reversed, both the orientation

and semi-minor axis of the ellipse is altered and consequence the intensity is changed. Even though the low FR due to birefringence, to the best of our knowledge, we are the first one to report FR of garnet films prepared by sputtering at this wavelength by waveguide coupling method.

0 degree　　2 degree　　4 degree　　6 degree

8 degree　　10 degree　　12 degree　　14 degree

16 degree　　18 degree　　20 degree

-2 degree　　-4 degree　　-6 degree　　-8 degree

-10 degree　　-12 degree　　-14 degree　　-16 degree

-18 degree　　-20 degree　　-22 degree
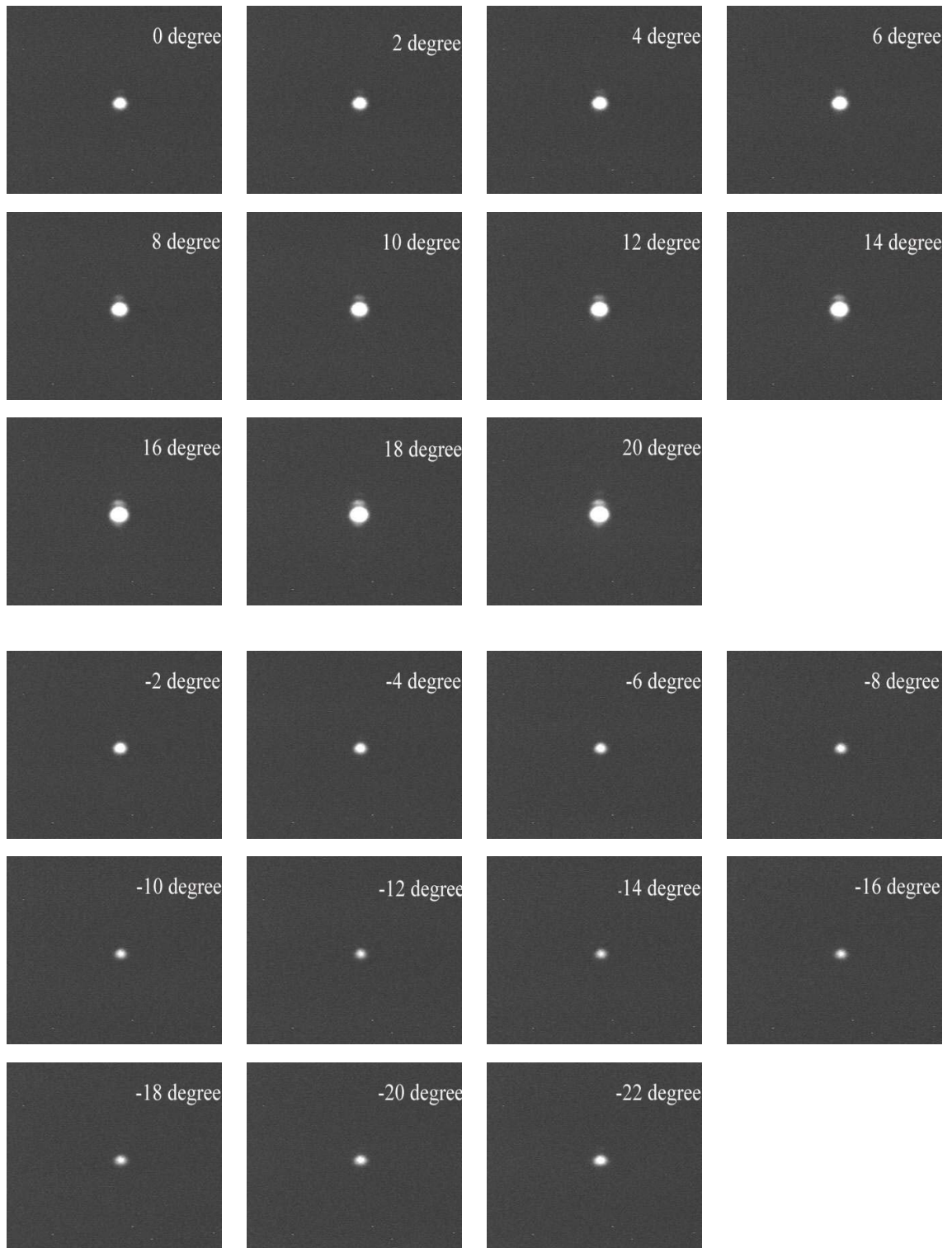
(a)
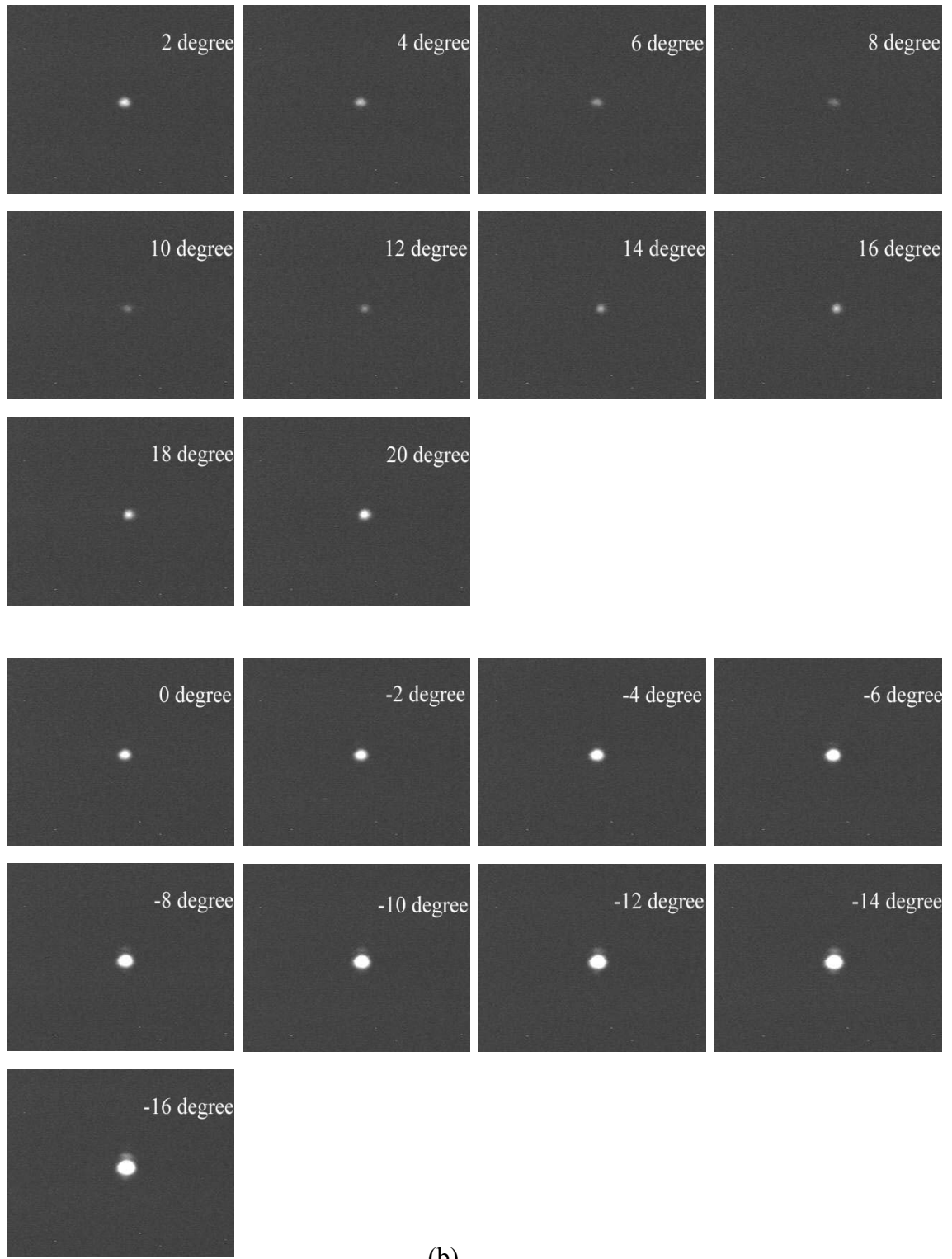
(b)

Figure 4.26 *Beam intensity profiles measured after propagating through the waveguide, before (a) and after (b) reversing the magnetic field. About -12°and 10°polarization rotation are obtained for the two magnetic filed directions.*

Chapter 5

Birefringence control and double layer structures fabrication

5.1 Introduction

Linear birefringence is the index difference between TE and TM modes that propagate in a planar waveguide. This birefringence, which is only prominent in the thin film forms and can be neglected in bulk garnet crystals (only growth induced birefringence may occur in bulk crystals), results in the oscillation of Faraday rotation and make the required 45° Faraday rotation very hard to achieve.
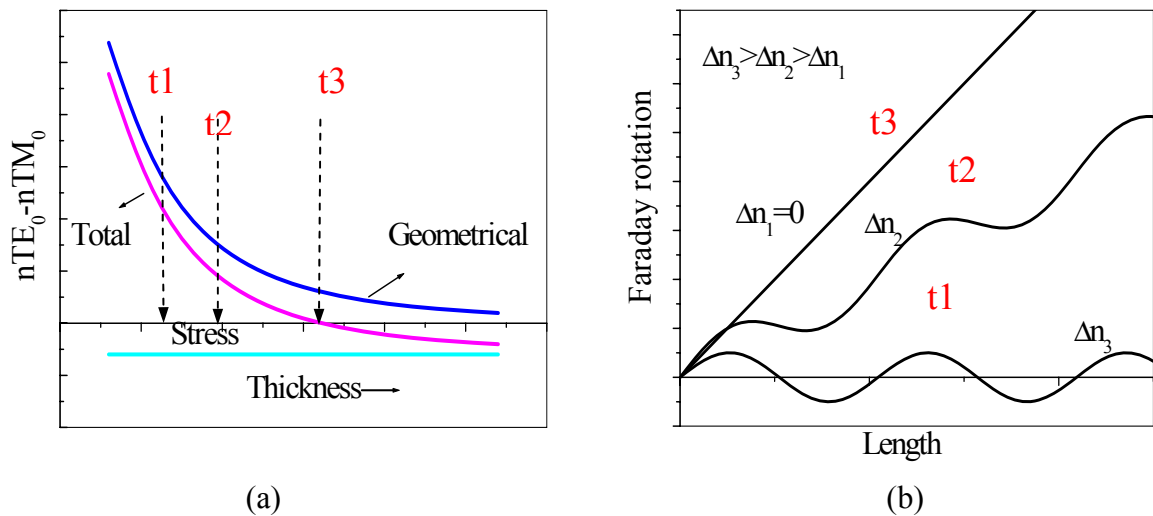
Figure 5.1 *(a) Geometrical, stress and total linear birefringence vs. thickness in a MO planar waveguide and (b) effect of magnitude of birefringence on Faraday rotation*

There are three kinds of linear birefringence [113] in epitaxial garnet films: geometrical or shape birefringence, stress induced or photoelastic birefringence and growth-induced birefringence. There is a fourth effect called magnetic linear birefringence, which is observed when the magnetization is perpendicular to the direction of propagation of the light. Since most configurations in MO devices are in-plane magnetized and the light

beam propagation direction is parallel to $\vec{M}$, this effect is normally neglected. Geometrical birefringence is inherent to asymmetric optical waveguides as a result of the different boundary conditions for TE and TM modes. This type of birefringence is present even in films with the same material refractive indices for in-plane and out-of-plane polarizations. It is positive and significant only when the film thickness is comparable to the wavelength of the light. So as the film thickness increases, the geometrical birefringence decreases towards zero. Its magnitude is higher for higher order modes. Stress-induced birefringence is caused when there is a lattice mismatch between film and substrate. Its sign depends on stress status. It is positive when the film is in tension and negative when the film is in compression. The stress birefringence is independent of film thickness. Growth induced birefringence is observed when there is more than one type of atom on the dodecahedral site. It is normally associated with directional growth from flux, such as LPE and bulk crystal that result in a nonrandom distribution of dodecahedral site atoms. It is in negative sign. For sputtered thin films, this contribution can be neglected since the atoms are randomly distributed due to nonequilibrium growth. This growth induced birefringence from LPE method can be reduced by proper annealing [114]. Total linear birefringence is the combined results of these three contributions. Fig. 5.1 shows the magnitude of geometrical, stress induced and total linear birefringence as a result of film thickness and their effect on Faraday rotation.
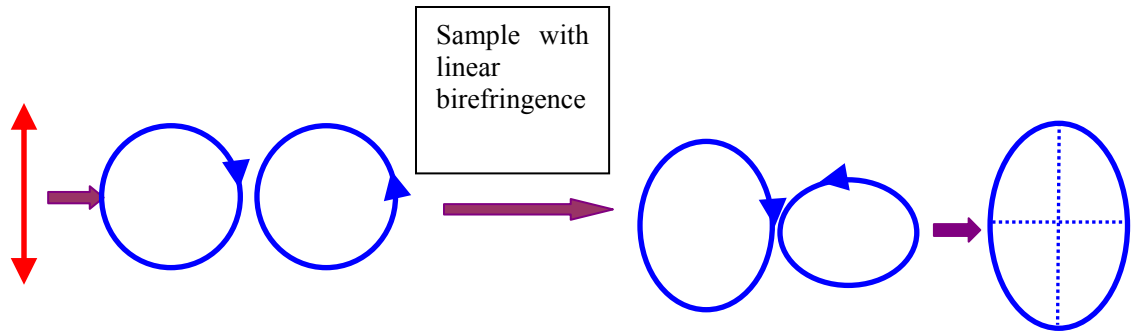
Figure 5.2 *Elliptical polarization output caused by linear birefringence. The linear birefringence combined with Faraday rotation change both the phases and normal modes of the linearly polarized light*

Linear polarization output is only obtained when total linear birefringence is zero or close to zero. If the linear birefringence is nonzero, the output will be elliptically polarized, as shown in Fig.5.2. This is due to linear polarization combined with Faraday rotation change not only the phases but also the normal modes from circularly to elliptically polarized light [143]. The linear birefringence should be very small in order to reach the linear output. For example, a linear birefringence of 1.5×10^{-4} would correspond to phase change of 360°/cm [$\Delta\beta = (2\pi/\lambda) \Delta n$] at $\lambda = 1.5$ μm, which is larger than the Faraday effect in YIG at this wavelength.

The first method to reduce oscillation of rotation was to periodically reverse the sign of Faraday coefficient, as suggested by Paroli [115] and first demonstrated by Tien et al [116], who used a serpentine electrical circuit with appropriate spatial periodicity to reverse the direction of magnetization along the light propagation path. Wolf et al [117] used localized laser annealing of garnet films of specially designed composition to permanently reverse the magnetization direction of sublattice. But these efforts make the processing quite cumbersome and expensive. Other efforts developed over the years have been to reduce the total linear birefringence to a small value so that the film acts as a pure Faraday rotator [113, 118]. As shown in Fig.5.1a, stress induced birefringence is in

negative sign if film is in compression. But geometrical birefringence is positive and decreases with increase of film thickness. The two contributions cancel each other out and the total linear birefringence crosses zero at some certain thickness. Thus the FR increases linearly with path length at this thickness. This method, however, requires stringent thickness control. Very careful thickness tuning must be employed by LPE to achieve the zero linear birefringence since growth rate of LPE is very fast and can't precisely control the film thickness. Normally the technique requires that the film thickness be overshot and then to thin down the film by wet etching and to measure the MO properties and repeat the procedure until the dependence of FR on length becomes linear.
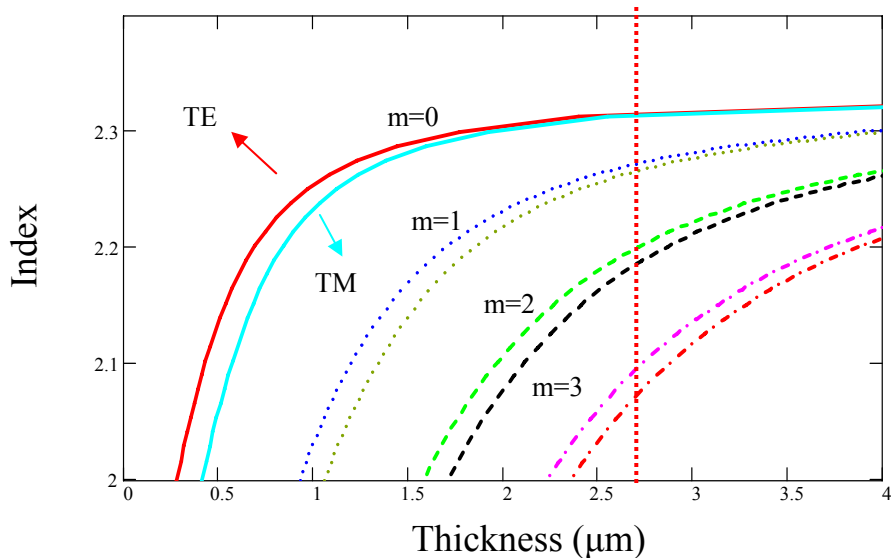
Figure 5.3 *Geometrical birefringence for different modes. Higher order modes have larger birefringence.*

Linear birefringence is different for each propagating mode. Higher order modes have larger birefringence (Fig. 5.3). Since index difference between Bi-YIG and GGG is about 0.3, several modes will be supported in Bi-YIG/GGG structure if film exceeds 1 μm at λ=1.55 μm. Films support only one single TE and one single TM mode is preferred since

the birefringence can be compensated or eliminated for only one pair of modes at a time. In addition, it will greatly simplify the measurement and analysis since only one mode is involved. Single mode films can be obtained by growing a double layer structure with the bottom layer having a slightly lower index. This type of double layer structure was fabricated by LPE exclusively in the past [129-138]. It is fabricated by growing the two layers at different temperatures since the incorporation of bismuth is affected by undercooling condition. More bismuth and lead are incorporated into the film at lower T, which will result in a larger index.

Sputtering has the advantage of more precise control of film thickness, making it a good substitute to LPE. Double layer structures fabricated by sputtering deposition have not yet been attempted in spite of this advantage of the sputtering technique. As far as we know, we are the first one to fabricated double layer single mode structures by sputtering technique. In this chapter, birefringence control and double layer single mode fabrication by sputtering will be discussed. Part of this work has been published in IEEE Transaction on Magnetics [144].

5.2 Birefringence control of garnet films by sputtering method

Bi-substituted iron garnet thin films are fabricated on $Gd_3Ga_5O_{12}$ (GGG) (111) single crystal substrates by RF magnetron sputtering. Two-inch diameter sintered ceramic plates of nominal compositions of $Bi_{0.8}Y_{2.2}Fe_5O_{12}$, $Bi_{0.8}Y_{2.2}Ga_1Fe_4O_{12}$, and $Bi_{0.7}Yb_{2.3}Fe_5O_{12}$ are used as targets. The sputtering conditions are summarized in Table 5.1. Films prepared under these conditions deposit epitaxially on the substrate, as

Table 5.1   RF magnetron sputtering conditions

Sputtering parameters	Experimental condition
Substrate material	GGG (111)
Background pressure (Torr)	Below 1×10^{-6}
Working pressure (Torr)	5×10^{-2}
Sputtering gas	Ar
RF power density (W/cm2)	2.47 to 4.93
Substrate temperature (Ts) (^{o}C)	560 to 630
Deposition rate (nm/min)	5 to 13

determined by X-ray crystallographic analysis (Fig. 5.4). The films show two distinct

peaks in Fig.5.4b due to compositional gradient when film is grown thicker than 1μm, as

discussed in the previous chapter. Film thickness is linearly proportional to the deposition

time (Fig.5.5) at a given substrate temperature.

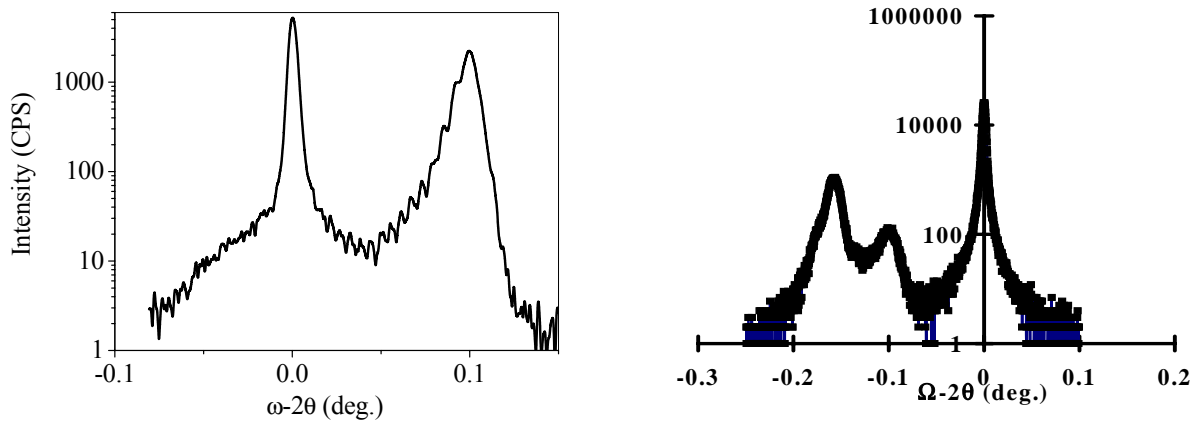Figure 5.4 *HRXRD scan of Bi-YbIG (a) and Bi-YIG (b) films sputtered under the conditions listed in table 1.*

The films behave as single-mode waveguides for thickness below ~ 0.9 μm, and are

multi-mode beyond that thickness at λ=1.55μm, as characterized by prism coupler. No

Faraday rotation, however, can be measured for the samples of this thickness at 1.55 μm
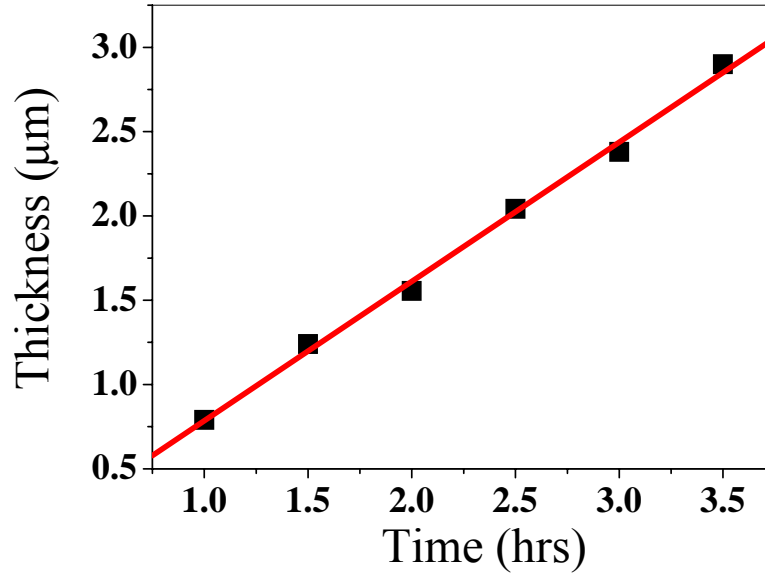
due to larger linear birefringence.

Fig. 5.5 Film thickness increase linearly with sputtering time

Measured fundamental mode birefringence data are shown in Figs. 5.6 as a function of thickness for sputter-deposited $Bi_{0.7}Yb_{2.3}Fe_5O_{12}$, $Bi_{0.8}Y_{2.2}Fe_4Ga_1O_{12}$ and $Bi_{0.8}Y_{2.2}Fe_5O_{12}$ samples, respectively. Bi-YbIG samples (Fig.5.7a) were deposited from left side target (stronger magnetic field strength and lower DC self bias), which was sputtered at 50W of output power compared to 80W output power for right side target. All the Bi-YIG samples (Fig.5.7b and Fig.5.7c) were sputter-deposited from right side target. Other sputtering parameters, such as substrate temperature and Ar pressure were kept the same, except for the 2.9µm-thick film in Fig. 5.6c which was deposited 25°C lower than the rest of the set. The latter two (Bi-YIG) sets of samples are in compression in the plane of the films whereas Bi-YbIG films are in tension as their lattice constant is smaller than that of GGG.   Clearly the mode birefringence decreases as the thickness of the film increases and for both types of Bi-YIG material, with and without gallium, it crosses the horizontal axis. So that at a particular thickness the net birefringence is zero. However, for Bi-YbIG film, the birefringence does not cross zero.
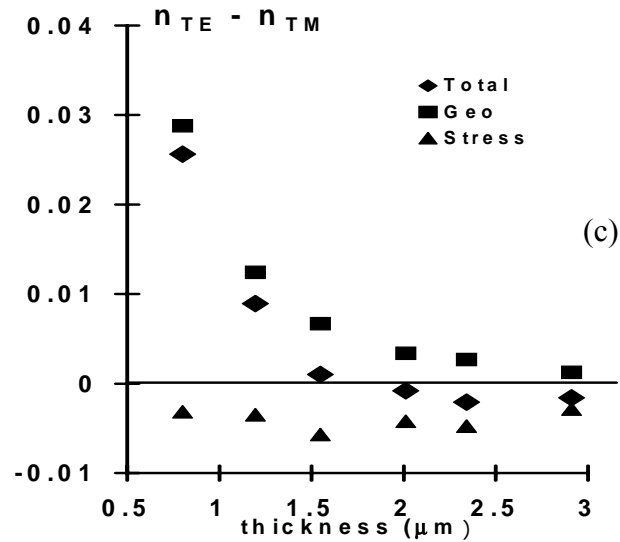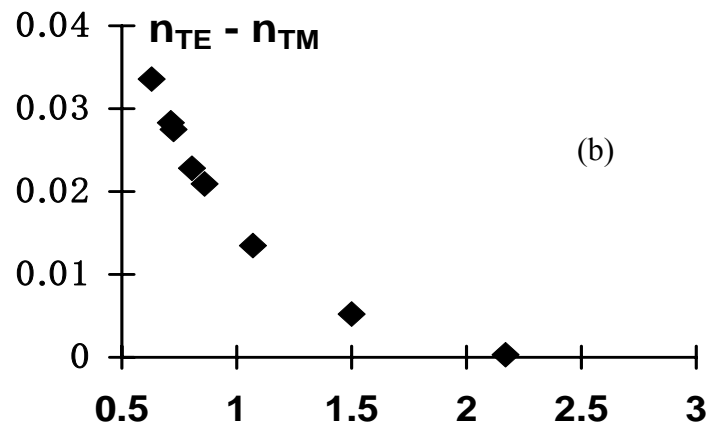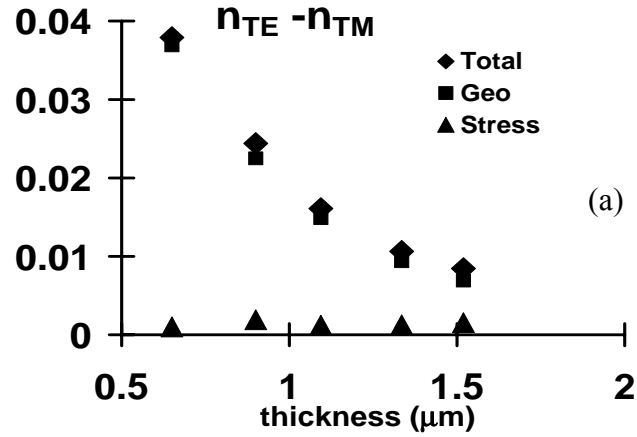
Figure 5.6 *Calculated geometrical birefringence, measured stress induced birefringence and total linear birefringence for Bi-YbIG (a) and Bi-YIG with Ga (b) and Bi-YIG without Ga (c)*

We find the difference between the measured mode birefringence and calculated shape birefringence to be nearly independent of film thickness, as shown in Figs. 5.7. It is negative, with an average value of -0.0041 ± 0.0005 for $(BiY)_3Fe_5O_{12}$ and small but positive (+0.0011 ± 0.0005) for $(Bi,Yb)_3Fe_5O_{12}$.

The stress-induced component of the birefringence for these garnets is expressible in terms of the photoelastic tensor component p_{44} as follows [119]:

$$\Delta n_\sigma = n_{TE,\sigma} - n_{TM,\sigma} = n_{0f}{}^3 p_{44}(\varepsilon_\perp - \varepsilon_\parallel)$$ (5-1)

Here n_{0f} is the refractive index of the isotropic (relaxed) film, and $\varepsilon_\perp$ and $\varepsilon_\parallel$ are the out-of-plane and in-plane components of the strain tensor in the $<111>, <0\bar{1}1>, <2\bar{1}\bar{1}>$ coordinate system. That is $\varepsilon_\perp = \dfrac{a_\perp - a_R}{a_R}$ and $\varepsilon_\parallel = \dfrac{a_\parallel - a_R}{a_R}$. Notice that for any given material, films in tension and compression have opposite signs of photoelastic birefringence. This is verified by our measurements and displayed in Fig.5.7. Values for p_{44} reported in the literature for various iron garnet families range from -0.04 to close to -0.06 [120, 121].

There is a variation in the measured lattice constant of our sputtered Bi-YIG films with thickness that we ascribe to compositional variations and relaxation effects resulting from the sputtering process, as discussed in the preceding chapter. For the thicker films which show two peaks, only the lower layer is considered in the analysis. The upper layer, which is more relaxed, exhibits much weaker strain and their contribution would fall within the estimated error bars of the stress birefringence (making the calculated $n_{0f}{}^3 p_{44}(\varepsilon_\perp - \varepsilon_\parallel)$ slightly less negative and closer to the measured difference in
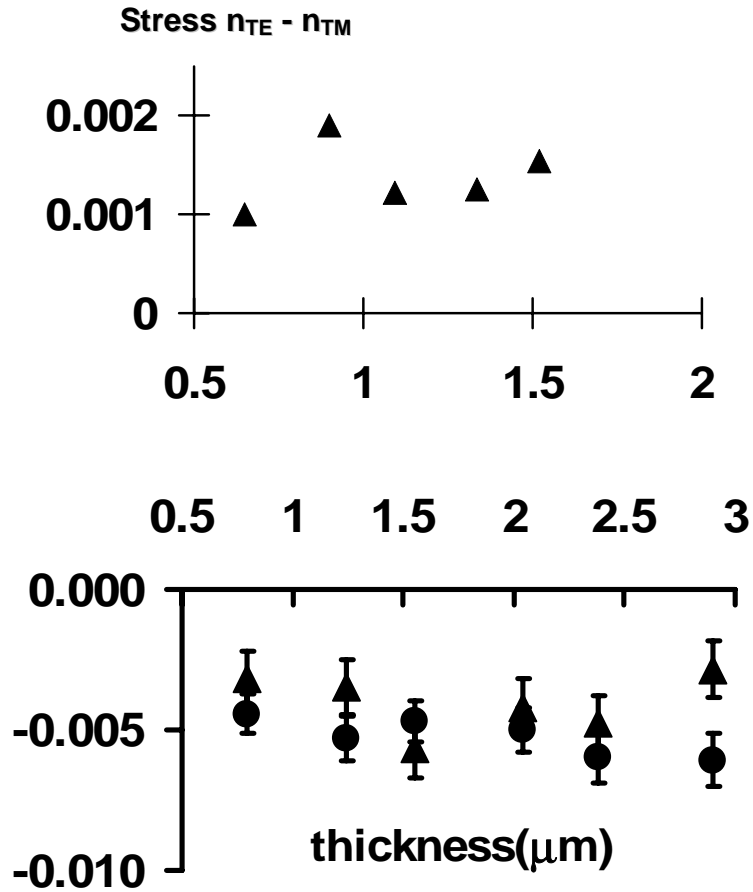
Figure 5.7 *Stressed induced birefringence (triangle) for film in tension (a) and film in compression (b). These data are obtained by subtracting the calculated geometrical birefringence from the measured fundamental mode birefringence. Notice that n_{TE}-n_{TM} is positive for the films under tensile planar strain and negative for films under compressive planar strain. For comparison, the calculated stress birefringence base on photoelastic component p_{44} also displayed (circle). The two set of data fit pretty well within the uncertainty of the data.*

birefringence). We estimate the variability in $\varepsilon_\perp$ - $\varepsilon_\parallel$ to be ±0.0007.   The calculated

birefringence difference (fundamental mode minus geometrical birefringence) is accurate

to within ±0.0005.   Table 5.2 compares the difference between fundamental mode and

geometrical birefringence with the calculated photoelastic birefringence based on Eq.5-1

for all three types of films, $(Bi,Y)_3Fe_5O_{12}$, $(Bi,Y)_3(Fe,Ga)_5O_{12}$, and $(Bi,Yb)_3Fe_5O_{12}$, using

the value of p_{44} reported in Ref. 120. It is clear from these comparisons that the difference in mode and geometrical birefringence can be fully accounted for by the photoelastic effect, within the uncertainty of the data.

Table 5.2 Measured stress induced birefringence and calculated photoelastic effect

Target Composition	Film Average Stress Birefringence	$n_{0f}^{3}p_{44}(\varepsilon_{\perp}-\varepsilon_{\parallel})$
$Bi_{0.8}Y_{2.2}Fe_4Ga_1O_{12}$	-0.0017 ± 0.0005	-0.0022 ± 0.0003
$Bi_{0.8}Y_{2.2}Fe_5O_{12}$	-0.0041 ± 0.0005	-0.0052 ± 0.0003
$Bi_{0.7}Yb_{2.3}Fe_5O_{12}$	$+0.0011 \pm 0.0005$	$+0.0008 \pm 0.0001$

LPE-grown bismuth-substituted yttrium and ytterbium iron garnet films on (111)-GGG substrates exhibit positive uniaxial magnetic anisotropy, $K_u^g > 0$ [114, 122-125]. The preferred magnetization direction in this case is along the uniaxial <111>-axis due to the non-random distribution of Bi^{3+} ions in the dodecahedral site and their effect on the axial crystal field in the garnet. This effect is also tied to the presence of growth-induced birefringence Δn_g in the film; [113, 118] thus a nonzero Δn_g is not expected for preferentially in-plane magnetized films.

Based on the reported magnitude of the growth-induced birefringence for Bi-YIG films (~0.0001), we cannot completely rule out this effect on the basis of the calculated photoelastic contribution. But the absence of a growth-induced out-of-plane magnetic anisotropy (as found in Bi-substituted LPE-YIG films), indicates that the growth-induced birefringence component is negligible here.

5.3 Double layer garnet films fabrication

5.3.1 Single mode double layer fabrication by sputtering deposition

The birefringence for single layer films discussed above are characterized based on measurement of fundamental mode. Birefringence is nonzero for higher order modes

even the fundamental mode crosses zero. Although one can couple 80%-90% of energy into the fundamental mode, as simulated by R-Soft™ integrated optics design software, extremely careful coupling is required for the actual measurement. Therefore a double layer structure which supports only one mode is desired to eliminate the birefringence and simplify the measurement.   Here we focus on using sputtering as a substitute to LPE [129-138] to fabricated double layer structure. Sputtering fabrication of double layer films can be done in two ways. One method is to fabricate films with two targets of different compositions: lower index film is first deposited on GGG substrate as a cladding layer and higher index film is subsequently deposited on top of the lower index film. This can be done easily by rotating the substrate holder to face one of the targets at a time in our sputtering system. Another method is to fabricate with one target but carrying out the sputter deposition at different pressures since the film index can be controlled by sputtering pressure, as shown in Fig.4.13.   The advantage of the latter method is flexible control of index difference between the two layers. We have studied both methods and successfully fabricated single mode double layer structures in both cases.

The double layer structure shows good epitaxial quality. The top layer is heterepitaxially grown on the bottom layer. Fig. 5.8 shows XRD analysis of the single layer $Bi_{0.8}Y_{2.2}Fe_4Ga_1O_{12}$/GGG, $Bi_{0.8}Y_{2.2}Fe_{4.8}Ga_{0.2}O_{12}$/GGG and double layer structure of $Bi_{0.8}Y_{2.2}Fe_{4.8}Ga_{0.2}O_{12}$/$Bi_{0.8}Y_{2.2}Fe_4Ga_1O_{12}$/GGG, deposited from two different targets.

A high resolution XRD of 1.2 μm thick $Bi_{0.7}Yb_{2.3}Fe_5O_{12}$ (n=2.268) deposited on 1μm thick $Bi_{0.8}Y_{2.2}Fe_4Ga_1O_{12}$ (n=2.20) is also displayed in Fig. 5.9. The films show very high intensity and narrow FWHM comparable to that of the substrate, indicating very good film quality.
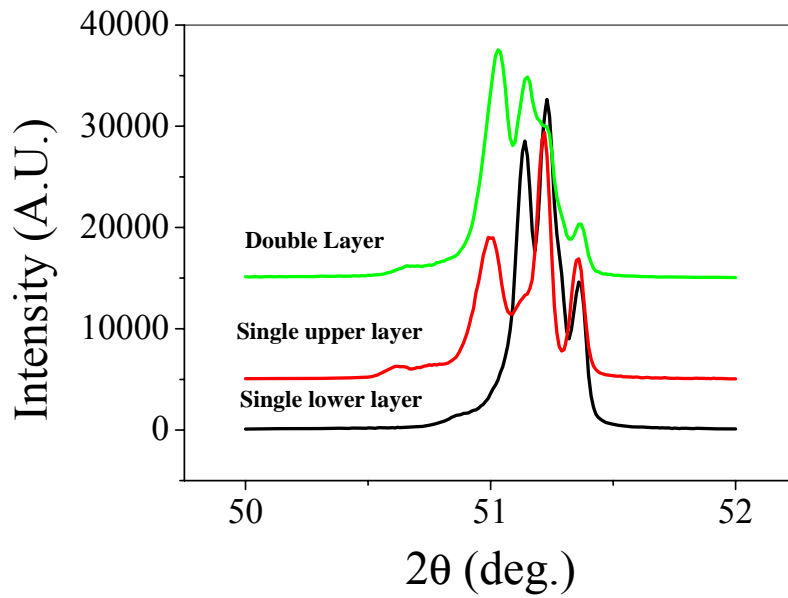
Figure 5.8 *XRD of Bi-YIG double layer structure prepared with two targets with nominal composition of $Bi_{0.8}Y_{2.2}Fe_{4.8}Ga_{0.2}O_{12}$ and $Bi_{0.8}Y_{2.2}Fe_4Ga_1O_{12}$.*

Figure 5.9 *HRXRD of double layer structures prepared with two different targets of $Bi_{0.7}Yb_{2.3}Fe_5O_{12}$ (n=2.268) and $Bi_{0.8}Y_{2.2}Fe_4Ga_1O_{12}$ (n=2.20)*

For double layer structure, we find that if films are in tensile stress, i.e. Bi-YbIG, tend to crack or peel off if deposited on a film in compressive stress (Bi-YIG) when thickness is

higher than about 1.8 μm. On the contrary, films in compressive stress can be grown up to 4 μm without cracking for the double layer structure. The cracks are caused by stress which is not accommodated by other means, e.g., misfit dislocations. While compressive stress can lead to the formation of dislocations in iron garnet films, tensile stress usually leads to fractures [126].

We have also studied the sputter deposition of double layer structure with one target but at different pressures. Fig. 5.10 shows a double layer structure deposited at 50mTorr for 1μm thick bottom layer (n=2.246) and at 25mTorr for top layer (n=2.255) of 3.1μm with a single $Bi_{0.8}Y_{2.2}Fe_4Ga_1O_{12}$ target.
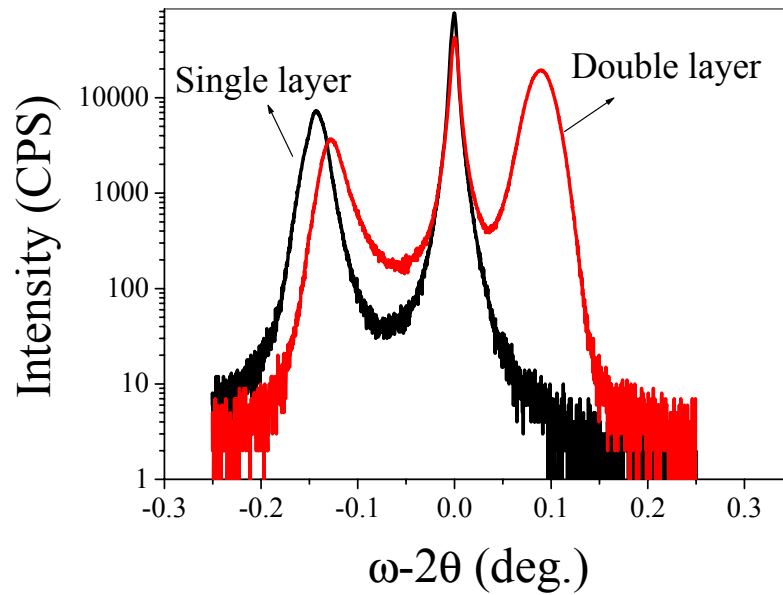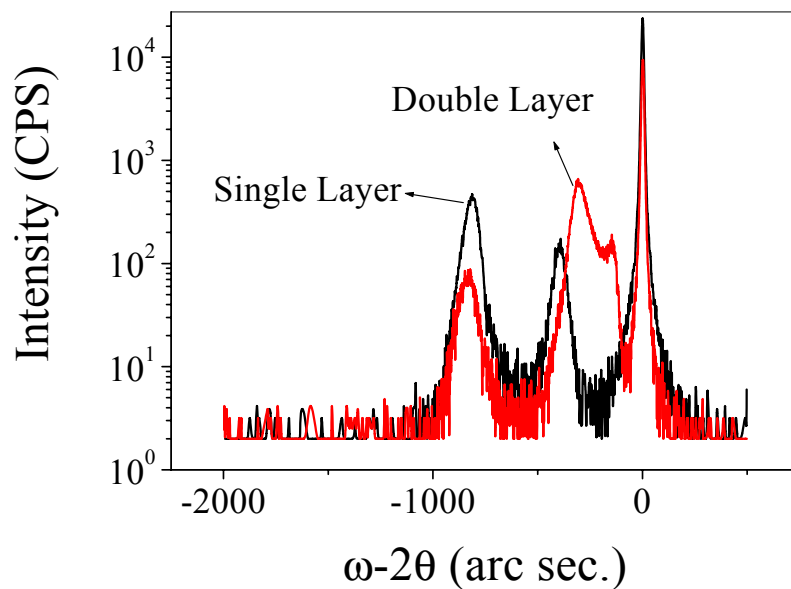

Figure 5.10 *Double layer structure prepared under 25mTorr (bottom layer) and 50mTorr (top layer)*

Notice the small peak shift of the bottom layer toward higher 2θ angle upon upper layer deposition in both Fig. 5.9 and Fig. 5.10. Interdiffusion, most probably Ga due to its smaller atomic radius, accounts for this peak shift. RBS results have already shown the evidence of gallium diffuses from the substrate into the deposited thin film for single

layer growth (Fig.4.10). We believe the double layer structure has the same Ga diffusion mechanism.

Film roughness increases upon deposition of upper layer. For example, RMS roughness increases from 1.4nm of single layer to 6.5nm upon 3μm upper layer deposition. This roughness, however, is still much better than films prepared by PLD method of single layer [92].
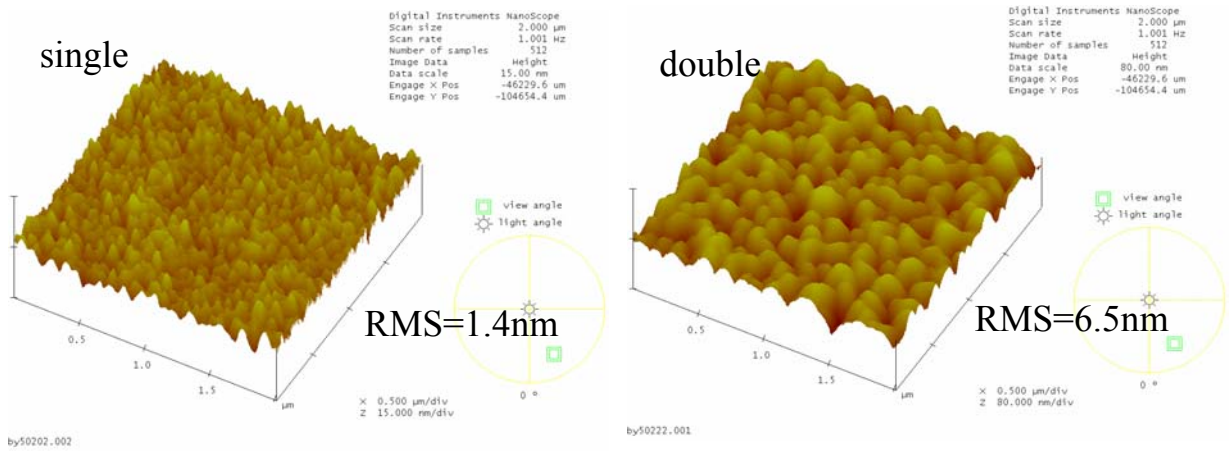
Figure 5.11 *AFM analyses of single layer and double layer show an increase of roughness and grain size after top layer deposition*

The double layer structure is in-plane magnetized, as shown in Fig. 5.12.
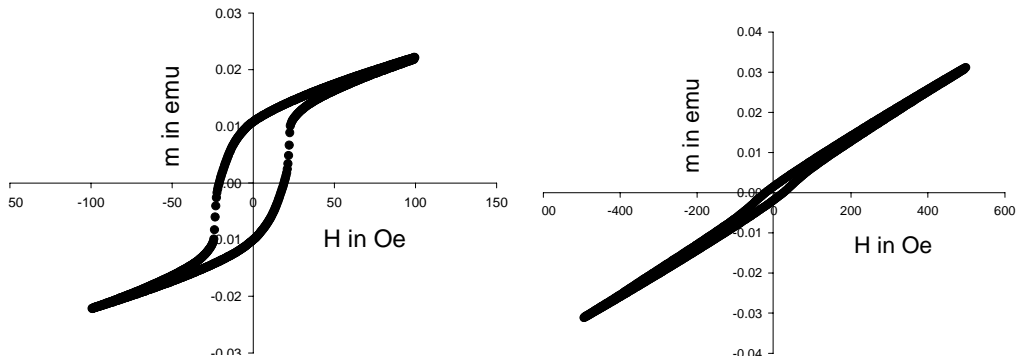
Figure 5.12 *In plane magnetization (a) and out of plane magnetization (b) for Bi-YIG/Bi-YbIG double layer. The thickness for the two layers is approximately 0.95 μm (lower layer) and 1.47 μm (upper layer), respectively.*

Ridge waveguides were fabricated on the double-layer films and Faraday rotation was measured. Similar as the single layers, the double layer structure show good confinement of the propagating beam. The Faraday rotation for a 2mm long waveguide is 10°, shown in Fig. 5.13b.
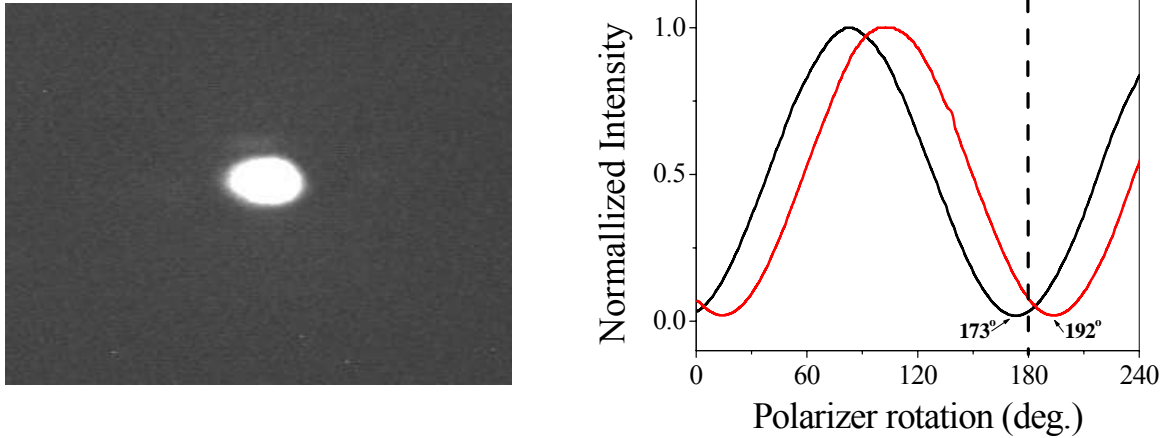
Fig. 5.13 *(a) Beam intensity profile measured after passing through a double layer waveguide. (b) The normalized intensity after rotating the polarization plane of the polarizer. The minimum intensities are found to occur at 173° and 192° when magnetic field is reversed. Thus the corresponding polarization rotation is about 7° and 12° for the two magnetic field direction.*

In a ridge waveguide structure, there exist both horizontal and vertical modes. Even there is single mode vertically, one can still see the multiple horizontal modes if the waveguide width exceeds the single mode limit. Keeping this in mind, we can not confirm that single mode propagates in our waveguides over 3μm wide by the optical fiber coupling. So we use prism coupler to characterize the single mode property. Only one mode is found from prism coupler measurement, as shown in Fig.5.14.

(a)   (b)
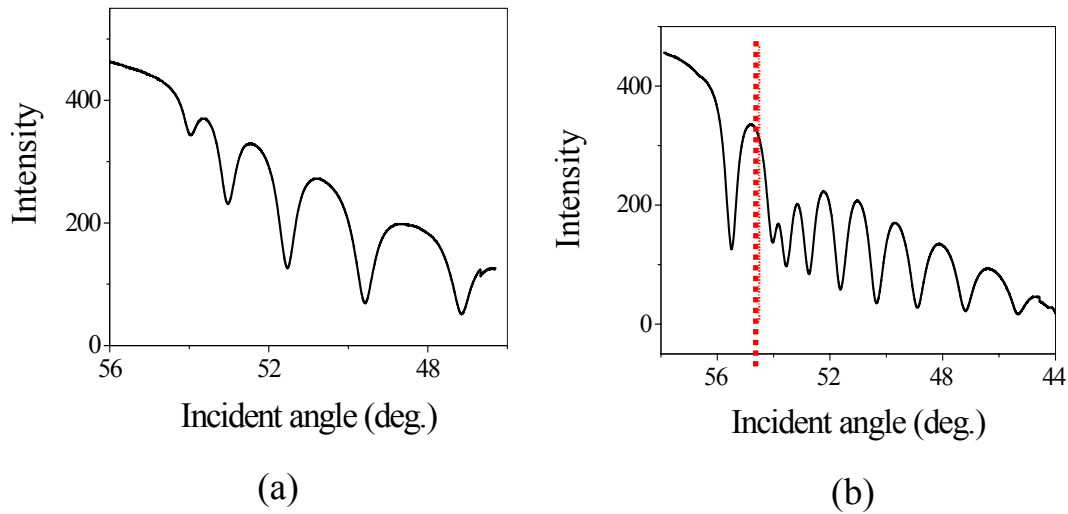
Figure 5.14 *Single mode propagation through the double layer structure is confirmed by prism coupler measurement. (a) shows the profile from the bottom layer while (b) shows the profile from double layer structure*

5.3.2 GGG overlayer deposition

Shape birefringence is caused by the asymmetry of single layer structure. Thus a symmetric cross-section in the waveguide results, in principle, in the elimination of shape-induced birefringence. We find that the sputter-deposition of a 480nm-thick GGG overlayer induces a decrease in the measured linear birefringence of the modes propagating in the Bi-YIG/GGG waveguides, as shown in Fig. 5.15. This is a purely geometrical effect due to the lower refractive index contrast between the core- and cover-layer. It should be pointed out that the mode birefringence is a primary quantity, measured directly by the prism coupler. In other words, it is not derived on the basis of some underlying assumption about the properties of the GGG overlayer.
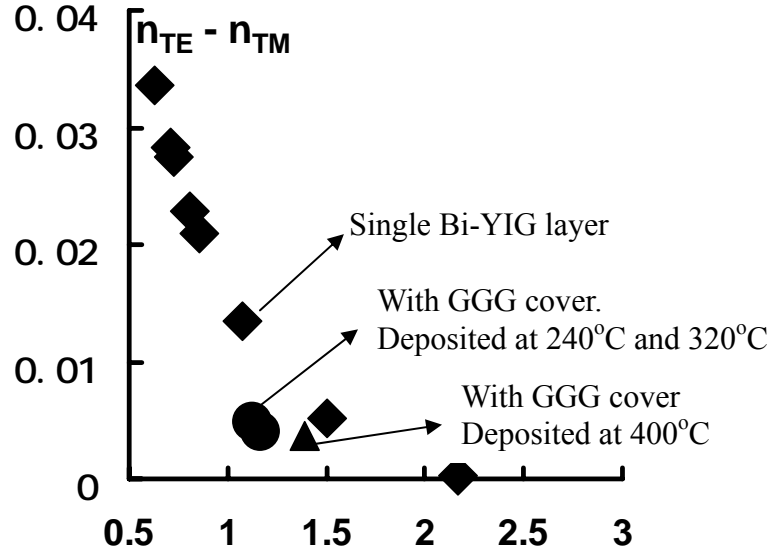
Figure 5.15 *Fundamental mode birefringence data for $(Bi,Y)_3(Fe,Ga)_5O_{12}$ films with and without GGG overlayer. The diamonds correspond to single layer films with Bi-YIG deposited at the same temperature and RF power. Bilayer Bi-YIG and GGG cover film birefringence are displayed by the circles and triangle data points and fall beneath the single layer curve. The Bi-YIG sputter deposition conditions are the same as for the single layer films. The GGG cover is deposited at $240\,^{\circ}C$ and $320\,^{\circ}C$ (circles) and $400\,^{\circ}C$ (triangle).*

The measured birefringence depends on GGG sputter-deposition temperature. It is lower than the single Bi-YIG layer but this decrease, although exhibiting little variance at low deposition temperatures, gets suppressed if the GGG is sputter-deposited at a temperature comparable to the Bi-YIG layer deposition temperature. Figure 5.15 display the effect in Bi-YIG films with GGG cover layer for a given film thickness deposited at different temperatures. The Bi-YIG films in these plots have been sputter-deposited from the same target under the same conditions.

X-ray data taken on these same samples are consistent with a reduced stress birefringence for higher GGG layer deposition temperatures. The trend is exhibited in Fig. 5.16 for 1μm-thick Bi-YIG films with GGG layers deposited at progressively higher temperatures. We note a reduction in the difference between (444) Bi-YIG and GGG substrate peak positions. This corresponds to a lowering of the stress component of the birefringence through a reduction in $\varepsilon_\perp - \varepsilon_{//}$. Thus the (negative) stress term balancing out the geometrical birefringence component gets partially neutralized or diminished in magnitude with increasing deposition temperature. We also notice that a 1h-800 °C annealing in flowing nitrogen partially restores the reduced birefringence in the film sputter-deposited at the highest GGG deposition temperature at the same time that it partially restores the strain anisotropy in the film (Fig. 5.17).
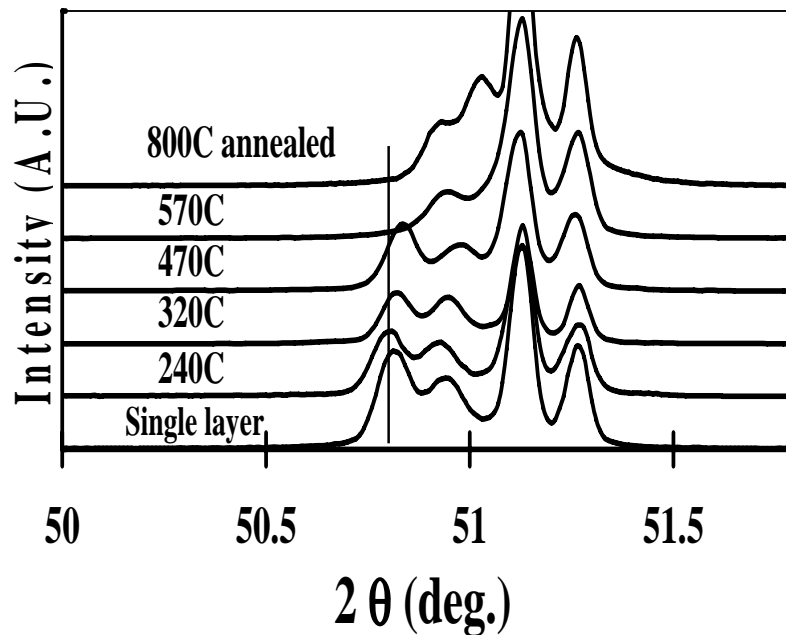
Figure 5.16 (*444) XRD spectra of a single layer Bi-YIG and bilayer Bi-YIG with GGG films at different GGG cover deposition temperatures. $K_{\alpha 1}$ and $K_{\alpha 2}$ lines are displayed for each lattice spacing. Notice the progression toward smaller strain with increasing temperature. The spectrum labeled 800 °C annealed corresponds to the film with GGG cover layer sputter-deposited at 570 °C and subsequently annealed at 800 °C in flowing nitrogen.*

200   300   400   500   600

$-\Delta(n_{TE}-n_{TM})$ (x10^{-3})

GGG growth temperature (^{o}C)
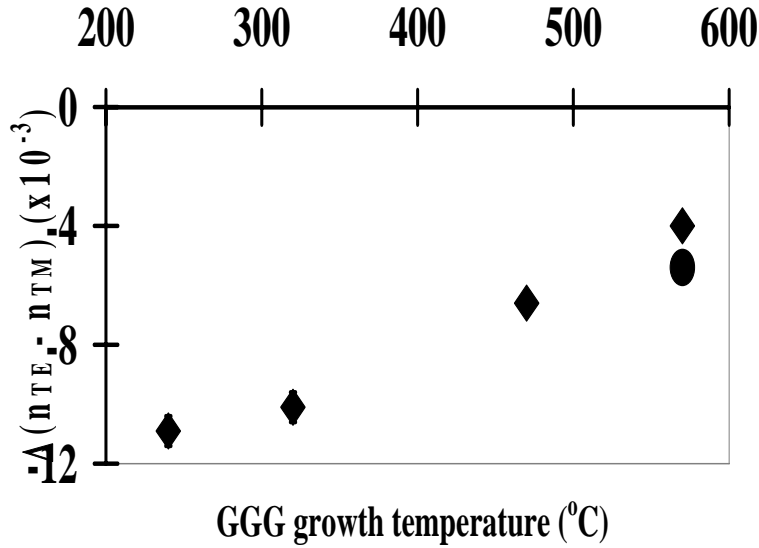
Figure 5.17 *Linear birefringence difference for 1.1±0.05 µm thick Bi-YIG films with and without GGG cover as a function of GGG deposition temperatures. The Bi-YIG layer is sputter-deposited from a $Bi_{0.8}Y_{2.2}Fe_4Ga_1O_{12}$ target at 570 ^{o}C. The vertical axis is $\Delta(n_{TE}-n_{TM})=(n_{TE}-n_{TM})^{with\ GGG}$ minus $(n_{TE}-n_{TM})^{without\ GGG}$. Notice the reduction in the magnitude of $\Delta(n_{TE}-n_{TM})$ with increasing temperature. The circular data point at 570 ^{o}C corresponds to a bilayer film annealed at 800 ^{o}C for 1h in following nitrogen. The sample has a lower birefringence than its unannealed counterpart.*

Upon sputtering the GGG top layer above 470 °C there is a darkening of the film that we ascribe to the conversion of Fe^{3+} ions in the Bi-YIG layer into Fe^{2+}. The presence of Fe^{4+} and Fe^{2+} instead of Fe^{3+} in the garnet is known to result in enhanced absorption. In other words, the deposition promotes a change in the valence of the iron ions in the garnet, most likely by diffusing oxygen out of the Bi-YIG layer. A suppression of the desirable birefringence reduction in the Bi-YIG/GGG waveguide and a lowering of the remnant magnetization in the Bi-YIG are also noted in this case. Annealing at 800 °C for 1h in flowing N_2 recovers the color. It also partially restores the change in birefringence and the remnant magnetization in the iron garnet film.

All the films in the present study exhibit in-plane magnetization, with coercive fields in the 8 to 20 Oe range. This is advantageous for in-plane Faraday rotator device

fabrication because the magnetization should be collinear with the beam propagation direction. No noticeable magnetic anisotropy is detected in the plane of any of the films. For samples with GGG cover sputter-deposited at 570 °C the net magnetization is reduced compared to that of the Bi-YIG film without GGG cover, as shown in Fig. 5.18.

(a)   (b)
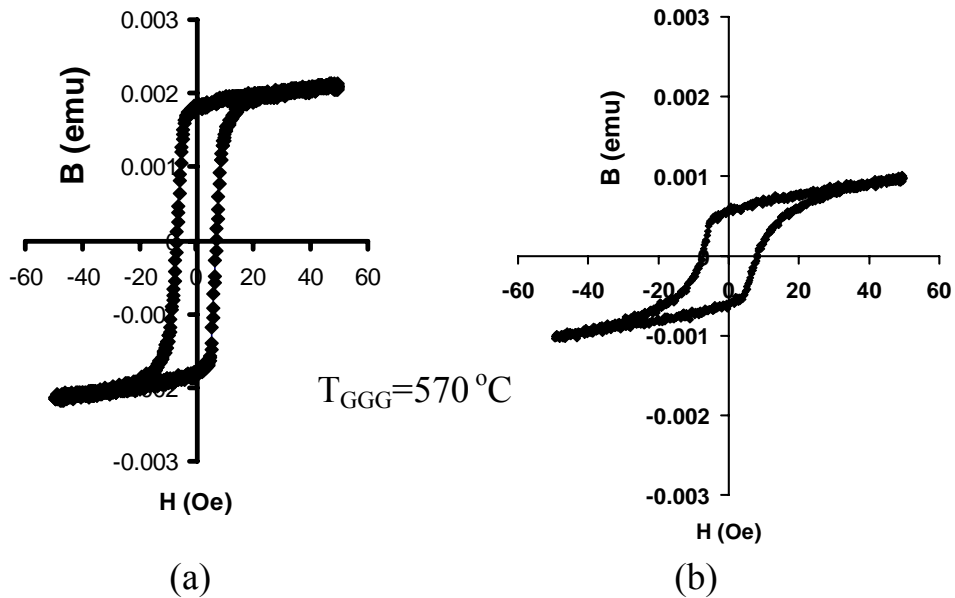
Figure 5.18 *(a) In-plane magnetization hysteresis loop for a 1.1 μm thick single layer film sputter-deposited at 570°C. The background magnetization from the substrate has been subtracted. (b) the same sample after a 480nm thick cover deposited at 570°C. Notice the reduced magnetic moment. The films have equal 1cm² surface area*

After annealing at 800 °C for 1h in flowing N_2 the magnetization and birefringence partially recover. For lower deposition temperatures the magnetization remains close to that of the original film, and the birefringence difference remains large. This is shown in Figs. 5.19
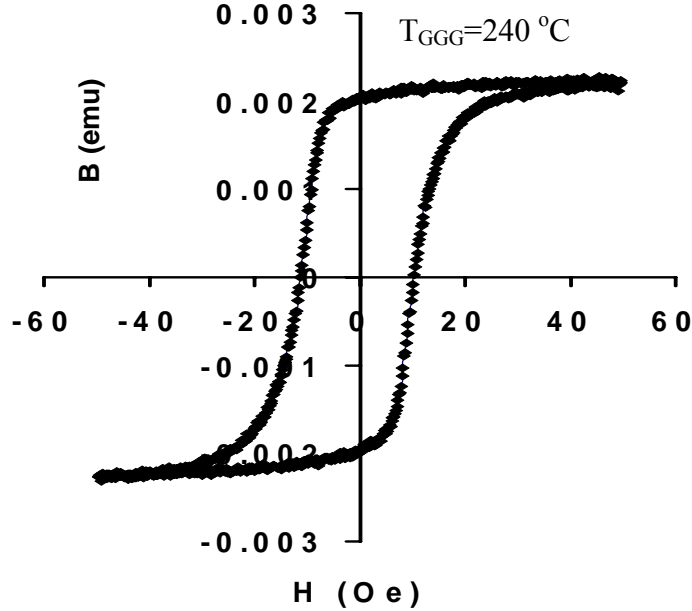
Figure 5.19 *In-plane magnetization hysteresis loop for 1.1 μm thick double layer film sputter-deposited from a $Bi_{0.8}Y_{2.2}Fe_5O_{12}$ target at 570 ^{o}C with 480 nm thick GGG cover deposited at 240 ^{o}C. The background magnetization from the substrate has been subtracted. This hysteresis loop is comparable to that of a single layer films*

It is known that for LPE-grown garnet films annealed at temperatures below the growth temperature the remnant magnetization will go down because of increased Ga incorporation into the octahedral site at the expense of the tetrahedral site [127]. We surmise that a similar phenomenon occurs in our sputtered samples during sputter-deposition, possibly including not just Ga redistribution between sites but an actual diffusion of Ga into the Bi-YIG layer upon GGG deposition. We have recorded some evidence for this by Rutherford Backscattering (RBS) compositional analysis, with some samples showing as much as 0.7 in Ga content increase per formula unit after a top layer deposition.

We suggest that the same phenomena that result in strain relaxation and increased absorption are also responsible for suppressing the remnant magnetization in these films.

These phenomena are the incorporation of Ga into the octahedral site in the Bi-YIG layer during GGG cover deposition and the reduction of Fe^{3+} into Fe^{2+} due to oxygen vacancies.

Chapter 6

Conclusions and future works

Driven by the need of a compact, integratable and wideband optical isolator, a flat-top response 1D-MPC based optical isolator was proposed and RF sputter deposition of bismuth substituted iron garnet thin films applied for the fabrication of 1D-MPC was developed and optimized during the thesis study. Theses include simulation study of multiple defects 1D-MPC and development and optimization of single layer and double layer bismuth substituted iron garnet thin films deposition processing. In particular, we studied the structural, compositional, birefringence and magnetooptical properties of sputter deposited bismuth substituted iron garnet thin films. All of which strongly affect the performance of waveguide isolator.

➤ **Multiple defects 1D MPC modeling – flat-top response**

One defect and two defects MPC designs suffer from either trade off between transmission and FR or very narrow bandwidth. We find that at least 3 defects are required to achieve the flat-top response of 1D-MPC with 45° Faraday rotation. 1.7nm and 3.0nm wide transmission bands are predicted for 3 and 4-defect 1D MPC, composed of Ce-YIG and GGG, with 100% transmission and 45° FR at $\lambda=1.55\mu m$. It is also found that the intensity and FR ripple effects can be minimized simultaneously by optimizing f_1 factor (larger than 2) in both cases. Total film thickness is less than 40μm for both 3- and 4-defects structures. This is almost 3-fold reduction in length compared to single Ce-YIG film for comparable rotation. A linear relationship between number of defects and bandwidth is also found. Beam propagation finite-difference time domain simulations for a 3-defect structure of 30.3μm long with 45° rotation show that the optical path length is

equivalent to 100±20 µm propagation in a uniform Ce-YIG film. So that beam confinement is necessary for integrated photonic circuit application.

➤ Structure and composition of bismuth substituted iron garnet thin films

The deposited bismuth substituted iron garnet thin film is epitaxilly grown on (111) GGG substrate and the epitaxial quality is influenced by sputtering parameters (chamber pressure, target/substrate distance, DC self bias, substrate temperature and flow of oxygen). We have found that films sputtered at substrate temperature between 500^oC and 650^oC, substrate/target distance longer than 4cm (left side target) or 5cm (right side target) and chamber pressure at 50mTorr result in good crystalline quality for Bi-YIG films. Dual layer structures start to develop when film thickness exceeds 1µm. Higher substrate temperature or lower DC self bias on target can increase the thickness for the 2nd layer to develop. The formation mechanism of the dual layer structure is found to be compositional gradient, rather than stress gradient across film thickness, as argued by other authors. We find that lower DC self bias or proper sputtering pressure (50mTorr for Bi-YIG and 25mTorr for Bi-YbIG) are important to maintain the stoichiometry of deposited film as that of target. The deposited films are in plane magnetized without noticeable anisotropy in the film plane. RMS surface roughness increases with film thickness but it is still lower than 6nm with thickness up to 4µm. The propagation loss is found to be 25±5 dB/cm due to the presence of oxygen vacancies but can be lowered to 10±5dB/cm by 500 ^oC annealing in an oxygen atmosphere. The Faraday rotation of a 3mm long waveguide is found to be about 10° at λ=1.55µm. The smaller magnitude is caused by presence of linear birefringence.

➤ Birefringence control by Sputtering deposition

We examine the linear birefringence control in RF sputter-deposited iron garnet films through thickness tuning method. Films in tensile stress show a positive stress induced birefringence and films in compressive stress show a negative stress induced birefringence. This stress induced birefringence is independent of film thickness. The photoelastic contribution to the linear birefringence compensates the geometrical birefringence component in compressively strained epitaxial iron garnet film. Thus zero-birefringence magnetic garnet film waveguides are feasible by RF-sputter deposition. Linear birefringence can be adjusted through cladding modifications to the waveguide structure by GGG over-layer deposition. The deposition of a GGG over-layer lowers the net linear birefringence and is found to reduce the remnant magnetization and enhance optical absorption for deposition temperatures above 470 $^\mathrm{o}$C.

➢ **Sputter deposition of double layer structure for single mode propagation**

Single mode double layer structures were fabricated by RF-sputter deposition. Epitaxial growth of double layer structures was successfully fabricated by sputtering with either two targets of different composition or one target but sputtered at different pressures (50mTorr and 25mTorr). Film roughness increases upon deposition of upper layer. For example, RMS roughness increases from 1.4nm of single layer to 6.5nm upon 3μm upper layer deposited. The single mode was confirmed by prism coupler. The Faraday rotation of the double layer structure is similar as the single layer film. About 10$^\mathrm{o}$ polarization rotation was found for a 2mm long waveguide.

Future work

The following work is recommended as a follow-up to this study:

Further study of composition gradient across film thickness

During the thesis study, we measured the composition by microprobe, RBS and XPS with sputtering technique. EPMA gives only the average composition. Although RBS can give compositional information as a function of film thickness, the resolution is lost when film is thick. Due to the availability of equipment, we did only one test of XPS with sputtering for a thin sample. Our confirmation of compositional gradient across film thickness is mainly based on measurement of lattice parameters by HRXRD. To follow up this thesis study, composition as a function of film thickness should be precisely measured. To overcome the preferential sputtering problem of XPS with sputtering technique, I suggest using Auger or XPS combined with wet etching method to measure the compositional profile. This is because wet etching has less selectivity and thus a fresh surface resembles the real composition can be obtained each time. Therefore an accurate compositional profile could be measured.

➢ **Further Faraday rotation and birefringence studies**

We could see some of the films have FR while some of the films do not have, even they are deposited at the same conditions and the XRD show the similar profile. There are two possible reasons that I believe to cause this problem. First and most important is the linear birefringence. The uncertainty of linear birefringence measured from the prism coupler is estimated as ± 0.0005. No FR of our sputtered films can be seen even for birefringence at a level about 0.0005. However, birefringence less than this value are not accurately measured. So a more precise equipment or measurement method should be

acquired. Second possibility is the compositional change in the films. We see compositional gradient, antisite defect and oxygen deficiency for our sputtered films. Those defects can cause the FR to diminish. So further studies should be carried out to investigate the relationship between FR, birefringence and compositions of the sputtered films.

➢ MPC on Silicon

Most of the optoelectronic devices are made from semiconductor material on semiconductor substrate. Eventually optical isolators are required to be integrated onto silicon substrate. The lattice mismatch between silicon (a=5.431Å) and YIG (a=12.383Å)
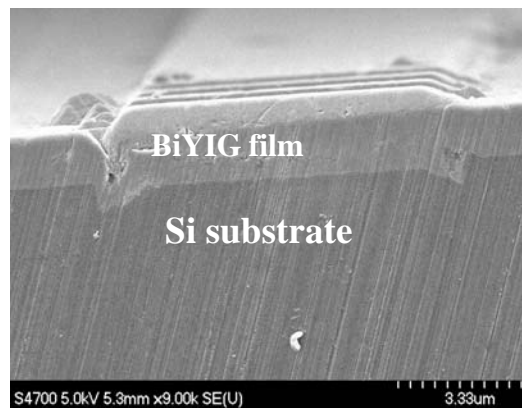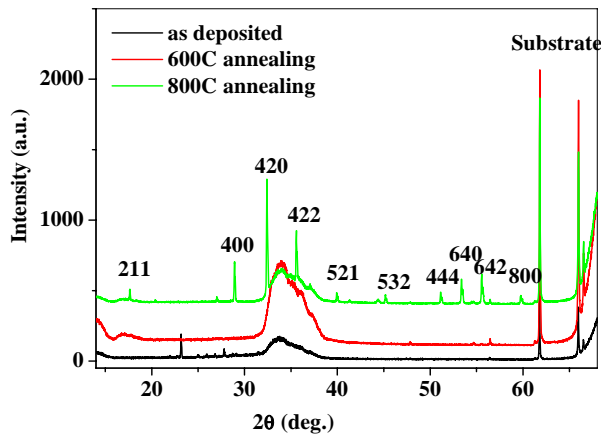

Figure 6.1 *(a) Crystallization of Bi-YIG film deposited on (111) silicon substrate at room temperature (b) Conformal deposition of Bi-YIG film on patterned 600nm deep and 2μm wide grooves.*

is too large and prevent the epitaxial growth. Polycrystalline form of garnet film may show a reduced FR. By fabricating MPC, we hope that the FR enhancement of MPC can compensate this drawback. We have already done some initial work. Fig6.1 shows that the Bi-YIG film can be crystallized at 800 ^{o}C in an oxygen atmosphere. Good conformal deposition of Bi-YIG film on grooves of 600nm deep and 2µm wide can be observed from this SEM picture. Annealing temperature can be further decreased by rapid thermal annealing.

> **2D-MPC fabrication by selective area epitaxy (SAE)**

The unique feature of 1D MPC implies another potential in 2D and 3D spatial symmetry. Some theoretical work [142] has already been devoted to the 2D and 3D models. Experimental work has just started in 2004. Selective area sputter epitaxy, combined with our capabilities of E-beam lithography and focus ion beam etching techniques developed in our group, can be used to fabricate two dimensional MPC in the future.

Recommendations for sputtering system improvement

To further investigate the sputter deposition of garnet films, I recommend the following upgrade to our sputtering system:

> Upgrade the resistive heater to a radiative heater

We are using a resistive heater. Substrate holder is spring loaded to contact the heater. There are always temperature differences from run to run due to the contact problem. A radiative heater has better temperature uniformity and reproducibility, thus resulting better film reproducibility.

> a smaller scale MFC to control oxygen flow

The MFC we are using for oxygen has a 100sccm full scale. The minimum flow rate we can control is 0.5sccm. Although films are oxygen deficient, films are not crystallized

when oxygen flow rate is 0.5sccm or more. A smaller scale MFC may be used to address both the oxygen vacancies and crystallinity problem.

➤ In-situ ion beam cleaning

We are using high temperature to remove the organic contaminants during pumping. In addition, the substrates are adhered to the molybdenum substrate holder by silver pant. There is possibility of contaminant during the process of removing the excessive silver paint. Thus installation of an in-situ ion beam etching system may increase the crystalline quality and also decrease the absorption. Ion beam etching can also reduce the surface roughness in-situ. This is very important for multilayer deposition.

➤ Thickness monitor (oscillator crystal)

The thickness is found to depend linearly on sputtering time. However, there are always variations from run to run, most probably due to contact problem between the substrate holder and the heater. This is tolerable for single layer deposition. However, for multiple stack deposition, the variation in thickness will result in the shift of the resonance frequency. Thus a thickness monitor is necessary for multilayer deposition.

➤ Load lock system

To reduce contamination and pumping time.

References:

1. *Physics of magnetic garnets*, edited by A. Paoletti, (North-Holland, New York) 1978

2. *Thin solid films: Electronics and optics*, Vol. 114, No.1-2, 1984

3. Frederic J. Kahn, P. S. Pershan, and J. Pemeika. "Ultraviolet Magneteo-optical properties of single-crystal orthoferrites, garnets and other ferric oxide compounds", *Phys. Rev.* Vol.185, No. 3, 1969, p891

4. James C. Suits, "Faraday and Kerr effects in magnetic compounds", *IEEE Trans. Magn.* Vol MAG-8, No.1, 1972, p95

5. G. B. Scott, D. E. Lacklison, H. I. Ralph, and J. L. Page. "Magnetic circular dichroism and Faraday rotation spectra of $Y_3Fe_5O_{12}$", *Phys. Rev. B*, Vol.12, No.7, 1975, p2562

6. G. B. Scott and D. E. Lacklison. "Magnetooptic properties and applications of bismuth substituted iron garnet", *IEEE Trans. Magn.* Vol. MAG-12, No. 4, 1976, p292

7. S. Wittekoek, T. J. A. Popma, J. M. Robertson and P. F. Bongers. "Magneto-optic spectra and the dielectric tensor elements of bismuth-substituted iron garnets at photon energies between 2.2-5.2eV", *Phys. Rev. B*, Vol.12, No. 7, 1975, p2777

8. Z. Simsa, H. Le Gall, J. Simsova, J. Kolacek and A. Le Paillier-Malecot. "Spectral dependences of Faraday rotation in $Y_{3-x}Bi_xFe_5O_{12}$ LPE films", *IEEE Trans. Magn.* MAG-20 (5), 1984, P1001

9. Garry A. Allen, Gerald F. Dionne. "Application of permittivity tensor for accurate interpretation of magneto-optical spectra", *J. Appl. Phys,* 73 (10), 1993, p6130

10. Gerald F. Dionne and Gary A. Allen. "Spectral origins of giant Faraday rotation and ellipticity in Bi-substituted magnetic garnets", *J. Appl. Phys.* 73 (10), 1993, p6127

11. L. E. Helseth, R. W. Hansen, E. I. Il'yashenko, M. Baziljevich and T. H. Johansen. "Faraday rotation spectra of bismuth-substituted ferrite garnet films with in-plane magnetization", *Phys. Rev. B*, Vol. 64, 174406, 2001

12. B. Keszei, Z. Vertesy, G. Vertesy. "Growth of Bi and Ga substituted YIG and LuIG layers by LPE method", *Cryst. Res. Technol.* 36 (8-10), 2001, p953

13. T. Aichele, A. Lorenz, R. Herg, P. Gomert. "Garnet layers prepared by liquid phase epitaxy for microwave and magneto-optical applications – a review", *Cryst. Res. Technol.* 38, No.7-8, 2003, p575

14. J. –P. Krumme, V. Doormann, R. Eckart. "Bismuth-substituted iron garnet films prepared by RF diode sputtering", *IEEE Trans. Magn.* Vol. MAG-20, No.5, 1984, p983

15. M. Gomi, T. Tanida and M. Abe. "RF sputtering of highly Bi-substituted garnet films on glass substrates for magneto-optic memory". *J. Appl. Phys.* 57(1), 1985. p3888

16. M. Gomi, K. Utsugi and M. Abe. "RF sputtered films of Bi-substituted garnet for magneto-optical memory". *IEEE Trans. Magn.*, Mag_22, No. 5, 1986. p1233

17. M. Gomi, T. Okazaki and M. Abe. "Bi-substituted garnet films crystallized during rf sputtering for M-O memory", *IEEE Trans. Magn.*, Mag-23, No.5, 1987. p2967

18. T. Okuda, N. Koshizuka, K. Hayahsi, T. Takahashi, H. Kobani and H. Yamamoto, "Faraday rotation in highly Bi-substituted yttrium iron garnet films prepared by ion beam sputtering", *IEEE Trans. Magn.* Vol MAG-23, Vol.5, 1987, p3491

19. M. Gomi, K. Satoh and M. Abe, "Improvement in optical and magnetic properties of Bi-substituted garnet sputtered films for magneto-optical recording", *J. Appl. Phys.* 63 (8), 1988, p3642

20. J. –P. Krumme, A.F. Otterloo, P.C. Zalm and J. Pertruzzello. "Surface segregation and preferential sputtering of bismuth in rf-magnetron-sputtered iron-granet films". *J. Appl. Phys.* 54(8), 1988. p3965

21. W. Eppler and M. H. Kryder. "The effects of the sputtering conditions on bismuth doped gadolinium iron garnet films". *IEEE Trans. Magn.*, 25(5), 1989. p3743

22. T. Takahashi, H. Toshima, N. Imaizumi, T. Okuda and Y. Yiyazawa. "Magnetic garnet films prepared by ion beam sputtering and their application to optical isolators". *IEEE Trans. Magn.* Vol. 27, No. 6, 1991, P5396.

23. Shinji Mino, Morito Matsuoka, Akiyuki Take, Atsushi Shibukawa and Ken'ichi Ono, "Complete Bi-substituted iron garnet (BIG) films prepared by electron cyclotron resonance (ECR) sputtering", *Jpn. J. Appl. Phys.* Vol, 31, Part 1, No. 6A, 1992, p1786

24. Y. Braik and H. Le Gall. "Influence of radio-frequency sputtering and crystallization parameters on the structure of the BiGa-DyIG garnet films for magneto-optical recording". *J. Appl. Phys.* 76(11), 1994. p7633

25. J. Ostorero, M. Escorne, A. Pecheron-Guegan, F. Soulette and H. Le Gall. "$Dy_3Fe_5O_{12}$ garnet thin film grown from sputtering of metallic targets". *J. Appl. Phys.* 75 (10), 1994, P6103.

26. Myung-Beom Park, Pyung Jin Kim and Nam-Hee Cho. "Chemical composition,

microstructure and magnetic characteristics of yttrium iron garnet (YIG, Ce-YIG) thin films grown by RF magnetron sputtering techniques". *IEEE Trans. Magn.*, Vol. 35, No.5, 1999. p3049

27. A. Furuya, C. Baubet, H. Yoshikawa, T. Tanabe, S. Hirono and M. Yamamoto. "Controlling garnet film composition by magnetic-field-controlled radio frequency magnetron sputtering". *J. Appl. Phys.*, 87(8), 2000. p6776

28. M.-B. Park, N.-H, Cho. "Structural and magnetic characteristics of yttrium iron garnet (YIG, Ce:YIG) films prepared by RF magnetron sputtering techniques", *J. Magn. Magn. Mater.* 231 (2001), p253.

29. M. Gomi, H. Furuyama and M. Abe, "Strong magneto-optical enhancement in high Ce-substituted iron garnet films prepared by sputtering", *J. Appl. Phys.* 70 (11), 1991, p7065

30. Shinji Mino, Akiyuki Take, Takehiko Uno, Toshihiro Shintaku and Atsushi Shibukawa, "Properties of Ce-substituted yttrium iron garnet film containing indium prepared by RF-sputtering", *Jpn. J. Appl. Phys.* 32, part 2, No. 7B, 1993, pL994

31. Y. Okamura, J. Kubota and S. Yamamoto, "Cerium substitute YIG single crystalline film prepared with ultra-high-vacuum magnetron sputtering", *IEEE Trans. Magn.* Vol.31, No. 6, 1995, p3289

32. Toshihiro Shintaku, Akiyuki Tate and Shinji Mino, "Ce-substituted yttrium iron garnet films prepared on $Gd_3Ga_5O_{12}$ garnet substrate by sputter epitaxy", *Appl. Phys. Lett.* 71 (12), 1997, p1640

33. Y. Okamura, T. kawakami and S. Yamamoto, "Sputter epitaxy of cerium yttrium iron garnet films on neodymium gallium substrates", *J. Appl. Phys.* 81 (8), 1997, p5653

34. Yasuyuki Okamura and Sadahiko Yamamoto, "Sputter deposition of cerium yttrium irion garnet films on substrates with ion-beam bombarded patterns", *Jpn, J. Appl. Phys, vol.*38, part.2, No. 6A/B, 1999, pL636

35. Bethanie J. H. Stadler and Anand Gopinath, "Mangeto-optical garnet films made by reactive sputtering", *IEEE Trans. Magn.* Vol. 36, No.6, 2000, p3957

36. P. C. Dorsey, S. E. Bushnell, R. G. Seed and C. Vittoria, "Epitaxial yttrium iron garnet films grown by pulsed laser deposition", *J. Appl. Phys.* 74 (2), 1993, p1242

37. Hideo Kidoh, Akiharu Morimoto and Tatsuo Shimizu, "Synthesis of ferromagnetic Bi-substituted yttrium iron garnet films by laser ablation", *Appl. Phys. Lett.* 59 (2), 1991, p237

38. B. M. Simon, G. Thomas, R. Ramesh, V. G. Keramidas and R. L. Pfeffer, "Growth

and characterization of ($Y_3Fe_5O_{12}$-$Bi_3Fe_5O_{12}$) heterostructures by pulsed laser deposition", *Appl. Phys. Lett.* 66 (7), 1995, p830

39. T. M. Le, F. Huang, D.D. Stancil and D. N. Lambeth, "Bismuth substituted iron garnet thin films deposited on silicon by laser ablation", *J. Appl. Phys.* 77(5), 1995, p2128

40. Ming-Yau Chern and Juin-sen Liaw, "Study of $Bi_xY_{3-x}Fe_5O_{12}$ thin films grown by pulsed laser deposition", *Jpn. J. Appl. Phys.* Vol.36, part 1, No.3A, 1997, p1049

41. Ming Yau Chern, Fan-Yun Lo, Da-Ren Liu, Kuang Yang and Juin-sen Liaw, "Red shift of Faraday rotation in thin films of completely bismuth-substituted iron garnet $Bi_3Fe_5O_{12}$", *Jpn. J. Appl. Phys.* Vol 38 part1, No.12A, 1999, p6687

42. Hyonju Kim, A. M. Grishin K. V. Rao, S.C. Yu, R. Sbiaa and H. Le Gall, "Ce-substituted YIG films grown by pulsed laser deposition for magneto-optic waveguide devices", *IEEE Trans. Magn.* 35 (5), 1999, p3163

43. N. Adachi, V. P. Denysenkov, S. I. Khartsev, A. M. Grishin and T. Okuda, "Epitaxial $Bi_3Fe_5O_{12}$ (001) films grown by pulsed laser deposition and reactive ion beam sputtering techniques", *J. Appl. Phys.* 88 (5), 2000, p2734

44. E. Popova, N. Keller, F. Gendron, M. Guyot, M. –C. Brianso, Y. Dumond and M. Tessier, "Structure and magnetic properties of yttrium-iron-garnet thin films prepared by laser deposition", *J. Appl. Phys.* Vol.90, No. 3, 2001, p1422

45. S. Kahl, S. I. Khartsev, A. M. Grishin, K. Kawano, G. Kong, R. A. Chakalov, J. S. Abell, "Structure, microstructure and magneto-optical properties of laser deposited $Bi_3Fe_5O_{12}$/$Gd_3Ga_5O_{12}$ (111) films", *J. Appl. Phys.* 91 (12), 2002, p9556

46. S.Kahl and A. M. Grishin, "Pulsed laser deposition of $Y_3Fe_5O_{12}$ and $Bi_3Fe_5O_{12}$ films on garnet substrates", *J. Appl. Phys.* 93(10), 2003, p6945

47. Masaru Okada, Shigehisa Katayama and Koji Tominaga, "Preparation and magneto-optic properties of Bi-substituted yttrium iron garnet thin films by metalorganic chemical vapor deposition", *J. Appl. Phys.* 69 (6), 1991, p3566

48. J. Cho, M. Gomi and M. Abe, "Bi-substituted iron garnet films with fine grains prepared by pyrolysis", *J. Appl. Phys.* 70 (10), 1991, p6301

49. M. Levy, R. M. Osgood, Jr. A. Kumar and H. Bakhru, "Crystal ion slicing of single-crystal magnetic garnet films", *J. Appl. Phys.* 83 (11), 1998, p6759

50. Koji Matsumoto, Satoshi Sasski, Yasunori Yamanobe, Kazuhiro Yamaguchi, Toshitaka Fujii and Yousuke Asahara, "Bismuth- and aluminum-substituted YIG single-crystal films on modified gadolinium gallium garnet single-crystal substrates", *J. Appl. Phys,* 70 (3), 1991, p1624

51. Hidetoshi Iwamura, Shintaro Hayashi, Hiroshi Iwasaki, "A compact optical isolator using a $Y_3Fe_5O_{12}$ crystal for near infra-red radiation", *Optical and Quantum Electronics,* 10, 1978, p393

52. R. Wolfe, J. F. Dillion, Jr., R. A. Lieberman and V. J. Fratello, "Broadband magneto-optic waveguide isolator", *Appl. Phys. Lett.* 57 (10), 1990, p960

53. H. Dammann, E. Pross, G. Tabe and W. Tolksdorf, "45° waveguide isolator with phase mismatch", *Appl. Phys. Lett.* 56 (14), 1990, p1302

54. R. Wolfe, R. A. Lieberman, V. J. Fratello, R. E. Scotti and N. Kopylov, "Etch-tuned ridged waveguide magneto-optic isolator", *Appl. Phys. Lett.* 56 (5), 1990, p426

55. Toshihiro Shintaku, Takehiko Uno and Morio Kobayashi, "Magneto-optic channel waveguides in Ce-substituted yttrium iron garnet", *J. Appl. Phys.* 74 (8), 1993, p4877

56. M. Levy, I. Ilic, R. Scarmozzino, R. M. Osgood, Jr., R. Wolfe, C. J. Gutierrez and G.A. Prinz, "Thin-film-magnet magnetooptic waveguide isolator", *IEEE Photonics Technology Letters,* 5 (2), 1993, p198

57. Toshihiro Shintaku and Takehiko Uno, "Optical waveguide isolator based on nonreciprocal radiation", *J. Appl. Phys.* 76 (12), 1994, p8155

58. M. Levy, R. M. Osgood Jr., H. Hegde, F. J. Cadieu, R. Wolfe and V. J. Fratello, "Integrated optical isolators with sputter-deposited thin-film magnets", *IEEE Photonics Technology Letters*, 8 (7), 1996, p903

59. N. Sugimoto, H. Terui, A. Tate, Y. Katoh, Y. Yamada, A. Sugita, A. Shibukawa and Y. Inoue, "A hybrid integrated waveguide isolator on a silica-based planar lightwave circuit", *Journal of Lightwave Technology,* Vol. 14, No. 11, 1996, p2537

60. Toshihiro, Shintaku, "Integrated optical isolator based on efficient nonreciprocal radiation mode conversion", *Appl. Phys. Lett.* 74 (14), 1998, p1946

61. J. Fujita, M. Levy, R. M. Osgood, Jr. L. Wikens and H. Dotsch, "Waveguide optical isolator based on Mach-Zehnder interferometer", *Appl. Phys. Lett.* 76 (16), 2000, p2158

62. S. E. Irvine and A. Y. Elezzabi, "A miniature broadband bismuth-substituted yttrium iron garnet magneto-optic modulator", *J. Phys. D: Appl. Phys,* 36, 2002, p2218

63. Mitsuteru Inoue, Takeshi Yamamoto, Keiji Isamoto and Toshitaka Fujii, "Effect of structural irregularity on propagation properties of optical waves in discontinuous magneto-optical meida with one-dimensional quasirandom array structures", *J. Appl. Phys.*, 79 (8), 1996, p5988

64. Mitsuteru Inoue, Keiji Isamoto, Takeshi Yamamoto and Toshitaka Fujii, "Magneto-optical Faraday effect of discontinuous magnetic media with a one-dimensional array structure", *J. Appl. Phys.* 79(3), 1996, p1611

65. Mitsuteru Inoue and Toshitaka Fujii, "A theoretical analysis of magneto-optical Faraday effect of YIG films with random multilayer structures", *J. Appl. Phys.* 81(8), 1997

66. Mitsuteru Inoue and Ken'ichi Arai, Toshitaka Fujii and Masanori Abe, "Magneto-optical properties of one-dimensional photonic crystals composed of magnetic and dielectric layers", *J. Appl. Phys.*, 83(11), 1998, p6768

67. Mitsuteru Inoue, Ken'ichi Arai, Toshitaka Fujii, Masanori Abe, "One dimensional magnetophotonic crystals", *J. Appl. Phys.,* 85 (8), 1999, p5768

68. Hideki Kato, Takeshi Matsushita, Akio Takayama, Motoji Egawa, Kazuhiro Nishimura and Mitsuteru Inoue, "Theoretical analysis of optical and magneto-optical properties of one-dimensional magnetophotonic crystals", *J. Appl. Phys.*, 93 (7), 2003

69. S. Sakaguci and N. Sugimoto, "Transmission properties of multilayer films composed of magneto-optical and dielectric materials", *Journal of lightwave technology*, Vol 17 (6), 1999, p1087

70. E. Takeda, No. Todoroki, Y. Kitamoto, M. Abe, M. Inoue, T. Fujii and Ken'ichi Arai, "Faraday effect enhancement in Co-ferrite layer incorporated into one-dimensional photonic crystal working as a Fabry-Perot resonator", *J. Appl. Phys.* 87 (9), 2000, p6782

71. S. Kahl and A. M. Grishin, "Enhanced Faraday rotation in all-garnet magneto-optical photonic crystal", *Appl. Phys. Lett.* 84 (9), 2004, p1438

72. H. Kato, T. Matsushita, A. Takayama, M. Egawa, K. Nishimura and M. Inoue, "Properties of one-dimensional magnetophotonic crystal for use in optical isolator devices", *IEEE Trans. Magn.* 38 (5), 2002, p3246

73. Hideki Kato and Mitsuteru Inoue, "Reflection-mode operation of one-dimensional magnetophotinic crystals for use in film-based magneto-optical isolator devices", *J. Appl. Phys.*, 91 (10), 2002, p7017

74. M. J. Steel, M. Levy and R. M. Osgood, "Photonic bandgaps with defects and the enhancement of Faraday rotation", *Journal of lightwave technology,* Vol 18 (9), 2000, p1297

75. M. Levy, H. C. Yang, M. J. Steel and J. Fujita, "Flat-top response in one-dimensional magnetic photonic bandgap structures with Faraday rotation enhancement", *Journal*

of Lightwave Technology, Vol. 19, No.2, 2001

76. Rong Li and Miguel Levy, "Bragg Grating Magnetic Photonic Crystal Waveguides", *Appl. Phys. Lett.* 86 (25), 251102, 2005

77. A. H. Eschenfelder. *Magnetic Bubble Technology,* Springer-Verlag, 1980

78. http://www.eotech.com/store/faraday.php

79. E. Yablonovitch, "Inhibited spontaneous emission in solid-state physics and electronics", *Phys. Rev. Lett.* 58, 1987, p2509

80. S. Sakaguchi and N. Sugimoto, "Transmission characteristic of periodic magneto-optical and dielectric multilayer films under a variable magnetic field", *J. Opt. Soc. Am. A,* Vol.16, No. 8, 1999, p2045

81. Chul-Sik Kee, Jae-Eun Kim and Hae Yong Park, "Two dimensional tunable magnetic photonic crystals", *Phys. Rev. B*, Vol.61, No. 23, 2000, 15523

82. I L Lyubchanskii, N N Dadoenkova, M I Lyubchanskii, E A Shapovalov and Th Rashing, "Magnetic photonic crystals", *J. Phys. D.* 36, 2003, pR277

83. J. E. Sipe, L. Poladian, C. Martijn de Sterke, "Propagating through nonuniform grating structures", *J. Opt. Soc. Am. A,* Vol.11, No. 4, 1994, p1307

84. Awdah Arraf, L. Poladian, C. Martijn de Sterke and T. G. Brown, "Effective-medium approach for counterpropagating waves in nonuniform Bragg gratings", *J. Opt. Soc. Am. A,* Vol. 14, No. 5, 1997, p1137

85. S. Visnovsky, K. Postava, T. Yamaguchi, "Magneto-optic polar Kerr and Faraday effects in magnetic superlattices", *Czechoslovak Journal of Physics,* Vol. 51, No.9, 2001, p917

86. L. D. Laudau, E. M. Lifshitz and L. Pitaevskii, *Electrodynamics of continuous media*, 2nd edition, 1984

87. Li Wei and John W. Y. Lit, "Phase-shifted Bragg grating filters with symmetrical structures", *Journal of Lightwave Technology*, Vol. 15, No8, 1997, p1405

88. R. C. Linares, "Epitaxial growth of narrow linewidth yttrium iron garnet films", *J. Cryst. Growth,* 3-4, 1968, p443

89. J. H. Park, J. K. Cho, K. Nishimura, H. Uchida and M. Inoue, "Growth of epitaxial garnet film by LPE for application to integrated mangetooptic light switch arrays", *Phys. Sta. Sol.* (a), 201, No.8, 2004, p1976

90. D. Dijkkamp, T. Venkatesan, X.D. Wu, S.A. Shaheen, N. Jisrawi, Y. H. Min-Lee, W.

L. McLean and M. Croft, "Preparation of Y-Ba-Cu oxide superconductor thin film using pulsed laser evaporation from high Tc bulk material", *Appl. Phys. Lett.* 51, No.8, 1987, p619

91. N. B. Ibrahim, C. Edwards and S. B. Palmer, "Pulsed laser ablation deposition of yttrium iron garnet and cerium-substituted YIG films", *Journal of Magnetism and Magnetic Materials*, 220, 2000, p184

92. Soren Kahl, Ph.D thesis, 2004

93. P. J. Besser, J. E. Mee, P. E. Elkins and D. M. Heinz, "A stress model for heteroepitaxial magnetic oxide films grown b chemical vapor deposition", *Mat. Res. Bull.*, Vol. 6, 1971, p1111

94. Shinji Mino, Akiyuki Tate, Takehiko Uno, Toshihiro Shintaku and Atsushi Shibukawa, "Structure and lattice deformation of Ce-substituted Yttrium iron garnet film prepared by RF sputtering", *Jpn. J. Appl. Phys.* Vol. 32, part 1, No.7, 1993, p3154

95. Akiyuki Tate, takehiko Uno, Shinji Mino, Atushi Shibukawa and Toshihiro Shintaku, "Crystallinity of Ce substituted YIG films prepared by RF sputtering", *Jpn. J. Appl. Phys.*, Vol.35, part 1, No. 6A, 1996, p3419

96. Eiju Komuro, Teruyoshi Hirano, Tatsuru Namikawa and Yohtaro Yamazaki, "Nonstoichiometric properties of Bi-substituted yttrium iron garnet sputtered films", *Jpn. J. Appl. Phys.* Vol. 33, Part 1, No.7A, 1994, p3902

97. Akinori Furuya and Shigeru Hirono, "Target magnetic-field effects on deposition rate in rf magnetron sputtering" *J. Appl. Phys.* 68 (1), 1990, p304

98. W. D. Westwood, "Calculation of deposition rates in diode sputtering systems", *J. Vac. Sci. Technol.* 15 (1), 1978, p1

99. Nam-Yang Lee, Tomoyuki Sekine, Yukio Ito and Kenji Uchino, "Deposition profile of RF-Magnetron-Sputtered $BaTiO_3$ thin films", *Jpn. J. Appl. Phys.* Vol.33, part.1, No. 3A, 1994, p1484

100. R. E. Somekh, "The thermallization of energetic atoms during the sputtering process", *J. Vac. Sci. Technol.* A 2, 1984, p1285

101. J. W. Matthews, S. Mader and T. B. Light, "Accommodation of misfit across the interface between crystals of semiconducting elements or compounds" *J. Appl. Phys.* vol. 41 (9), 1970, p3800

102. L. B. Freund and S. Suresh, *Thin film materials: stress, defect formation and surface evolution*, Cambridge University Press, 2003

103. R. People and J. C. Bean, "Calculation of critical layer thickness versus lattice mismatch for Ge_xSi_{1-x}/Sis strained-layer heterostructures", *Appl. Phys. Lett.* 47 (3), 1985, p322

104. R. H. Miles, T. C. Mcgill, P. P. Chow, D. C. Johnshon, R. J. Hauenstein, C. W. Nieh and M. D. Strathman, "Dependence of critical thickness on growth temperature in Ge_xSi_{1-x}/Si superlattices", *Appl. Phys. Lett.* 52(11), 1988, p916

105. S. N. G. Chu, A. T. Macrander, K. E. Strege and W. D. Johnston, Jr., "Misfit stress in InGaAs/InP heteroepitaxial structures grown by vapor-phase epitaxy", *J. Appl. Phys.* 57 (2), 1985, p249

106. J. Y. Tsao and B. W. Dodson, "Excess stress and the stability of strained heterostructures", *Appl. Phys. Lett.* 53 (10), 1988, p848

107. G. J. Whaley and P. I. Cohen, "Relaxation of strained InGaAs during molecular beam epitaxy", *Appl. Phys. Lett.* 57 (2), 1990, p144

108. G. L. Price, "Critical-thickness and growth-mode transitions in highly strained In_xGa_{1-x}As films", *Phys. Rev. Lett.* 66 (4), 1991, p469

109. Tong-Yi Zhang, Sanboh Lee, L. J. Guido and Chun-Hway Hseuh, "Criteria for formation of interface dislocations in a finite thickness epilayer deposited on a substrate", *J. Appl. Phys.,* 85 (11), 1999, p7579

110. Jaemo Im, O. Auciello, P. K. Baumann, S. K. Streiffer, D. Y. Kaufman and A. R. Krauss, "Composition-control of magnetron-sputter-deposited $(Ba_xSr_{1-x})Ti_{1+y}O_{3+z}$ thin films for voltage tunable devices", *Appl. Phys. Lett.* 76 (5), 2000, P625

111. YiFeng Yang, James E. Nordman and Ji Ung Lee, "Effects of deposition conditions on stoichiometry of off-axis RF sputtered BiSrCaCuO thin films", *IEEE Transactions on Applied   Superconductivity,* Vol 3, No. 1, 1993, p1543

112. Chan, Wen-Hao, Shen Hui-Ling, Chou, Lih-Hsin, Wang, Jinn-Lung and Tsai, Jyi-Ching, "Effect of in-situ DC-bias on the composition, microstructure and dielectric properties of RF-magnetron reactive sputtered $(Ba,Sr)TiO_3$ films", *Materials Research Society Symposium-Proceedings,* V596, 2000,p43

113. R. Wolfe, V. J. Fratello and M. McGlashan-Powell, "Thin film garnet materials with zero linear birefringence for magneto-optic waveguide devices", *J. Appl. Phys.*, 63 (8), 1988, p3099

114. K. Ando, N. Takeda, N. Koshizuka and T. Okuda, "Annealing effects on growth-induced optical birefringence in liquid-phase-epitaxial-grown Bi-substituted iron garnet films", *J. Appl. Phys.* Vol. 57 (4), 1985, p1277

115. P. Paroli, "Magneto-optical devices based on garnet films", *Thin solid films,* 114,

1984, p187

116. Tien P. K. Tien, R. J. Martin, R. Wolfe, R.C.Lecraw and S. L. Blank，"Switching and modulation of light in magneto-optic waveguide of garnet films", *Appl. Phys. Lett.* 21 (8), 1972, p394

117. R. Wolf, J. Hegarty, J. F. Dillon, JR., L.C. Luther, G. K．Cellar, L. E. Trimble and C. S. Dorsey, " Thin-film waveguide magneto-optic isolator", *Appl. Phys. Lett.*, 46 (9), 1985, p817

118. R. Wolfe, V. J. Fratello and M. McGlashan-Powell, "Elimination of birefringence in garnet films for magneto-optic waveguide devices", *Appl. Phys. Lett.*, 51 (16), 1987, p1221

119. J. F. Nye, *Physical Properties of Crystals.* Oxford, U. K. Oxford Univ. Press, 1985, p235-254

120. R. T. Lynch Jr., J. F. Dillon Jr. and L. G. Van Uitert, "Stress birefringence in ferromagnetic garnets" *J. Appl. Phys.*, Vol. 44 (1), 1973, p225

121. A. N. Ageev, O. G. Rutkin, A.S. Trifonov, V. B. Kravtchenko, L. M. Filmonova, H. Le Gall and J. M. Desvignes, "Stress and growth-induced anisotropic birefringence in garnet films", *Revue De Physique Appl.,* Vol 20, 1985, p753

122. T. Okuda, N. Koshizuka, A. Murata, Y. Yokoyama and K. Ando, "Control of birefringence in LPE-grown magnetic garnet films" *J. Appl. Phys.*, vol.55 (6), 1984, p2176

123. A. Murata, N. Koshizuka, T. Okuda and K. Ando, "Guided-wave properties and mode conversions in $(BiNdLu)_3(FeAlLu)_5O_{12}$ films", *IEEE Trans. Magn.* vol. MAG-21, No.5, 1985, p1657

124. V. J. Fratello, S. E. G. Slusky, C. D. Brandle and M. P. Norelli, "Growth-induced anisotropy in bismuth: rare-earth iron garnets", *J. Appl. Phys.*, vol. 60 (7), 1986, p2488

125. P. Hansen and K. Witter, "Growth-induced uniaxial anisotropy of bismuth-substituted iron-garnet films", *J. Appl. Phys.* Vol. 58 (1), 1985, p454

126. V. J. Fratello, H. M. O'Bryan and C. D. Brandle, "Search for high thermal expansion substrates for magneto-optic thick film garnets", *J. Cryst. Growth,* vol. 166, 1996, p774

127. P. Roschmann, "Redistribution kinetics of Ga and Al substitutions in yttrium iron garnet", *J. Magn. Magn. Mater.*, vol. 15-18, ser.3, 1980, p1305

128.R. Wolfe, J. Hegarty, L. C. Luther, and D. L. Wood, "Single mode magneto-optic waveguide films", *Appl. Phys. Lett.*, 48 (8), 1986, p508

129.E. Pross, H. Dammann, and W. Tolksdorf, "Light guidance and mode conversion in magneto-optic buried channel waveguides", *J. Appl. Phys.*, 68 (8), 1990, p3849

130.E. Pross, W. Tolksdorf, and H. Dammann, "Yttrium iron garnet single mode buried channel waveguides for waveguides isolators", *Appl. Phys. Lett.* 52 (9), 1988, p682

131.Atsushi Shibukawa and Morio Kobayashi, "Optical TE-TM mode conversion in double epitaxial garnet waveguide", *Applied Optics*, vol. 20 (14), 1981, p2444

132.W. Tolksdorf, H. Dammann, E. Pross, B. Strocka, H. J. Tolle, and P. Willich, "Growth of yttrium iron garnet multi-layers by liquid phase epitaxy for single mode magneto-optic waveguides", *J. Cryst. Growth*, vol. 83, 1987, p15

133.W. Tolksdorf, I. Bartels, H. Dammann, and E. Pross, "Growth of buried garnet channel waveguides by liquid phase epitaxy", *J. Cryst. Growth*, vol. 84, 1987, p323

134.Yujiro Katoh, Naoto Sugimoto, Akiyuki Tate and Atsushi Shibukawa, "Preparation of substituted $Y_3Fe_5O_{12}$ single mode buried waveguides on a [100] oriented $Gd_3Ga_5O_{12}$ substrate", *Jpn. J. Appl. Phys*. Vol. 32, part.2 No. 4A, 1993, pL508

135.Santi Kaewsuriyathumrong, Tetsuya Mizumoto, Honming Mak and Yoshiyuki Naito, "Double-layered magnetooptic channel waveguide for waveguide isolator application", *Journal of Lightwave Technology*, Vol. 8 (2), 1990, p177

136.Naoto Sugimoto, Yujiro Katoh, Akiyuki Tate, Toshihiro Shintaku, Hiroshi Terui, and Atushi Shibukawa, "Preparation of Magneto-optic single-mode buried channel waveguides of Lanthanum- and Gallium-substituted Yttrium iron garnet", *Jpn. J. Appl. Phys.* vol. 34, part. 1, No.6A, 1995, p3113

137. H. Dammann, E. Pross, G. Rabe, W. Tolksdorf, and M. Zinke, "Phase matching in symmetrical single-mode magneto-optic waveguides by application of stress", *Appl. Phys. Lett.*, vol. 49 (26), 1986, p1755

138.W. Tolksdorf, H. Dammann, E. Pross, B. Strocka, F. Welz, and P. Willich, "Growth of magneto-optic garnet layers on structured surfaces", *J. Cryst. Growth*, vol. 99, 1990, p616

139.H. Donnerberg and C R A Catlow, "Atomistic computer simulations of yttrium iron garnet (YIG) as an approach to materials defect chemistry: I. Intrinsic defects", *J. Phys.: Condens. Matter*. 5, 1993, p2947

140.P. Novak, J. Englich, H. Stepankova, J. Kohout, H. Lutgemeier, K. Wagner and W. Tolksdorf, "Evidence for magnetic interactions between distant cations in yttrium iron

garnet", *Phys. Rev. Lett.* vol.75 (3), 1995, p545

141. Maija M. Kuklja and Ravindra Pandey, "Atomic modeling of native point defects in yttrium aluminum garnet crystals", *J. Am. Ceram. Soc.*, 82 (10), 1999, p2881

142. Magneto-optical materials for photonics and recording, MRS symposium proceeding, Edited by Koji Ando, William Challener, Richard Gambino and Miguel Levy, vol. 834, 2004

143. In consultant with M. Levy

144. **_H.C. Yang,_** M. Levy, R. Li, P. D. Moran, C.Gutierrez and A. K. Bandyopadhyay, "Linear birefringence control and magnetization in sputter deposited magnetic garnet film waveguides," IEEE Trans. Mag. **40**, 3533-3537 (2004)

Publication List

1. X. Huang, R. Li, ***H.C. Yang,*** M. Levy, "Multimodal and birefringence effects in magnetic photonic crystals," J. Magn. Mag. Materials, 2005, in press
2. M. Levy, X. Huang, R. Li, ***H.C.Yang*** and H. Bakhru, Proceedings of SPIE - The International Society for Optical Engineering, v 5515, Nanoengineering: Fabrication, Properties, Optics, and Devices, 2004, p 30-41
3. ***H. C. Yang,*** M. Levy, R. Li, P. D. Moran, C.Gutierrez and A. K. Bandyopadhyay, "Linear birefringence control and magnetization in sputter deposited magnetic garnet film waveguides," IEEE Trans. Mag. **40**, 3533-3537 (2004).
4. R. Li, X. Huang, M. Levy and ***H.C. Yang***, "Photonic crystal ridge waveguides on magnetic garnet films", Mater. Res. Soc. Symp. Proc. Vol. 834, 65-71 (2004)
5. M. Levy, ***H. C. Yang,*** and M. J. Steel, "Flat top response in one-dimensional magnetic photonic band gap structures with Faraday rotation enhancement," IEEE J. Lightwave Technol. **19**, 1964-1969 (2001).
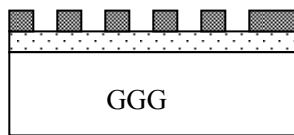
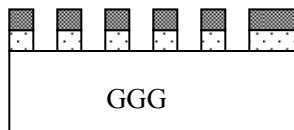**Appendix: Optical Waveguide Fabrication procedure**

← Garnet

GGG
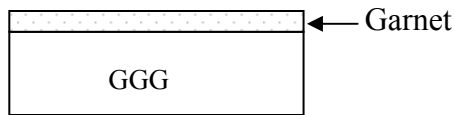
Garnet film is RF-sputter deposited on GGG substrate
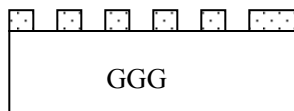
← Photo Resist

GGG
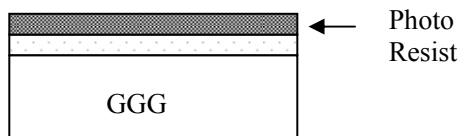
Spin Photoresist on the garnet film

GGG

Waveguides pattern is fabricated on the photoresist by photolithography

GGG

Waveguides pattern is transferred to the garnet film by dry etching

GGG

Remove photoresist